Sequential Linear Programming Coordination Strategy for Deterministic and Probabilistic Analytical Target Cascading

by

Jeongwoo Han

A dissertation submitted in partial fulfillment
of the requirements for the degree of
Doctor of Philosophy
(Mechanical Engineering)
in The University of Michigan
2008

Doctoral Committee:

Professor Panos Y. Papalambros, Chair
Professor Vijayan N. Nair
Associate Professor Kazuhiro Saitou
Associate Research Scientist Michael Kokkolaras
Staff Research Scientist Trudy R. Weber, General Motors Corp.

To my wife.

ACKNOWLEDGEMENTS

The completion of such a demanding project could not have been accomplished without the assistance of numerous individuals who served as critical sources of support and guidance. First and foremost, I would like to thank my lovely wife, Mijung, for her support and encouragement. She have helped me to go through all the difficulties since we met five year ago.

I would like to thank Professor Panos Papalambros for being my advisor, mentor and friend and encouraging me to speak professionally (or loud and clearly). Many thanks to Prof. Vijay Nair and Prof. Kazu Saitou for providing their time towards evaluating this disseration. I would also like to show my gratitude to Dr. Michael Kokkolaras for many advises on my researches and Trudy Weber for providing me valuable comments on hybrid vehicle and giving a chance to work in the General Motors Corp. as an intern.

I would like to thank every one from Optimal DEsign (ODE) laboratory: Miles for inspiring the dissertation idea and being a wonderful friend; James for great research discussions and the electric vehicle model; Erin for green inspiration; Subroto for sharing his knowledge and archive on design optimization under uncertainty; Zhijun and Arlene for treating me like a family; Andreas for discussions on hybrid vehicle control; Sulaiman for letting me know about him; Jarod and Bart for collaborations on IT business; Hyoung June, Harrison and Jeremy for great advises on both research and life in US; Katie, Tahira, Michael, Steven, Kwang Jae, Diane, Harshit and Kuk

Hyun for being great lab-mates. Also thanks to Hosun, Chulho, Jihyun, Sukmoon, Jonghwa, Youngjune, Youngmin, Hyogyeum and Gueon.

I also want to thank Eunha Kim for proofreading and being a fabulous sister-in-law. I also wish to appreciate my family.

My research has been partially supported by NSF Grant DMI-0503737, the General Motors Corporation and the Automotive Research Center, a US Army Center of Excellence in Modeling and Simulation of Ground Vehicle Systems at the University of Michigan. This support is gratefully acknowledged.

TABLE OF CONTENTS

LIST OF TABLES

Table

LIST OF FIGURES

Figure

LIST OF SYMBOLS

The following nomenclature is used consistently in the dissertation wherever possible, with the exception of Allison's structural optimization problem in Section 3.4.2 and 4.4.3 and a hybrid electric fuel cell vehicle design problem in Chapter 5, which use their own set of symbols to define the examples.

$\circ$	Component-wise multiplication of two vectors
Δl_e	Predicted reductions in f_e
Δf_e	Actual reductions in f_e
$\mathcal{C}_{ij}$	Set of the children of element j at level i
$\mathbf{c}_A$	Vector of active consistency constraints
$\mathbf{c}_{ij}$	Vector of local consistency constraints of element j at level i
$\bar{\mathbf{d}}_{ij}^{(l)}$	Vector of solution for the LP subproblem of element j at level i at SLP iteration l
$\mathbf{d}_{\mathbf{t}_{ij}}^{(l)}$	Vector of solution for $\mathbf{t}_{ij}$ at SLP iteration l
$\mathbf{d}_{\mathbf{x}_{ij}}^{(l)}$	Vector of solution for $\mathbf{x}_{ij}$ at SLP iteration l
$\mathrm{E}[X]$	Expected value of X
$\mathcal{F}$	Filter
F_X	Cumulative Distribution Function (CDF) of X
f_X	Probability Density Function (PDF) of X
f_{ij}	Local objective of element j at level i

$\mathbf{g}$	Vector of inequality constraints
$\mathbf{g}_A$	Vector of active inequality constraints
$\mathbf{g}_{ij}$	Vector of local inequality constraints of element j at level i
$\mathbf{h}$	Vector of equality constraints
$\mathbf{h}_{ij}$	Vector of local equality constraints of element j at level i
i	Level index in ATC hierarchy
j, k	Element index in ATC hierarchy
LP_{ij}	LATC/PLATC subproblem
l	SLP iteration index
O_{ij}	Element i at level j
p_f	Probability of failure
p_f^t	Target probability of failure
P_{ij}	ATC/PATC subproblem for element j at level i
p_X	Probability Mass Function (PMF) of X
$\Pr[\cdot]$	Probability of satisfying a condition
$\mathbf{T}_{ij}$	Vector of random design targets to element j at level i
$\mathbf{t}_{ij}$	Vector of deterministic design targets to element j at level i
$\mathbf{R}_{ij}$	Vector of random design responses from element j at level i
$\mathbf{r}_{ij}$	Vector of deterministic design responses from element j at level i
X	Random variable
X_n	Sequence of X
$\mathbf{x}$	Vector of local design variables
$\mathbf{X}_{ij}$	Vector of random local design variables of element j at level i
$\mathbf{x}_{ij}$	Vector of deterministic local design variables of element j at level i
$\bar{\mathbf{x}}_{ij}$	Vector of design variables of element j at level i

x^p	Percentile
$\mathrm{Var}[X]$	Variance of X
β	Reliability index
β^t	Target reliability index
β^L, γ^L	User-defined constants for filter
δ	Buffer constant for δ activity
δ^L, σ^L	User-defined constants for SLP algorithm
$\mathcal{E}_i$	Set of elements at level i
ϵ_{ij}	Maximum consistency error between $\mathbf{t}_{ij}$ and $\mathbf{r}_{ij}$
ζ_t, ζ_f	Suspension strategy constants
η	Constraint violation function
κ_p	pth principal curvature of g_m at MPP
μ_X	Expected value of X
π	Relaxation function
ρ	Trust region radius
σ_X	Standard deviation of X
Φ	CDF of a standard normal distribution

Allison's Structural Optimization Problem

E_i, $E_{r,j}$	Young's modulus of beam i and rod j, respectively
F_i	Transmitted force of beam i
$F_{t,i}$	Limit for transmitted force of beam i
f_i	Vertical deflection of beam i
$f_{r,j}$	Elongation of rod j
L	Length of beams and rods
m_i, $m_{r,j}$	Mass of beam i and rod j, respectively
ρ	Density of the material
$\sigma_{a,j}$	Axial stress in rod j
$\sigma_{b,i}$	Bending stress in beam i
$\bar{\sigma}$	Limit for stress

Hybrid Electric Fuel Cell Vehicle Design Problem

A^{fc}	Fuel cell active area
A^{bt}	Battery cell area
$a^{\mathrm{fc}}, b^{\mathrm{fc}}$	Coefficients of the approximation of $P_{\mathrm{net}}^{\mathrm{fc}}$
a^{bt}, b^{bt}, c^{bt}	Coefficients of the approximation of R_{dis} and R_{chr}
d^{bt}	Mean value of the differences of R_{dis} and R_{chr}
C_p	Specific heat capacity of air
C^{pt},C^{mt}	Cost of powertrain and vehicle motor, respectively
C^{fc}, C^{bt}	Cost of fuel cell system and battery, respectively
C^{ic}	Target IC engine cost
$\mathrm{C}_{\mathrm{dsl}}$, $C_{\mathrm{H_2}}$	Diesel and hydrogen fuel expense, respectively
$\mathrm{C}_{\mathrm{p}}^{\mathrm{ent}}$	Vehicle production cost

$\mathrm{Cp}^{\mathrm{bt}}$	Battery columbic capacity
D_{dsl}	Diesel fuel price
$\bar{D}_{\mathrm{dsl}}$	Normal level of D_{dsl}
E^{fc}, E^{bt}	Fuel cell and battery open circuit voltage, respectively
$\dot{E}_{\mathrm{H_2}}$	Fuel energy consumed in a fuel cell
$\dot{E}_{\mathrm{e^-}}$	Equivalent electric energy consumed in a battery
F	Faraday constant
$\mathrm{fe}_{\mathrm{dsl}}$	Fuel economy of a conventional light truck
$\mathrm{fe}^{\mathrm{pt}}$	Fuel economy of a design powertrain
H_{LHV}	Low heating value of hydrogen
h_{n}	Negative electrode thickness in a battery cell
h_{p}	Positive electrode thickness in a battery cell
h_{s}	Separator thickness in a battery cell
h^{bt}	Representative battery cell thicknesses
$I_{\mathrm{st}}^{\mathrm{fc}}$	Fuel cell stack current
$I_{\mathrm{min}}^{\mathrm{fc}}$, $I_{\mathrm{max}}^{\mathrm{fc}}$	Minimum and maximum fuel cell current, respectively
$I_{\mathrm{l}}^{\mathrm{bt}}$	Battery cell load current
$I_{\mathrm{p}}^{\mathrm{bt}}$	Current though the polarization resistance in a battery cell
J_t	Instantaneous energy consumption of a powertrain
$M_{\mathrm{H_2}}$, $M_{\mathrm{O_2}}$	Molar masses of hydrogen and oxygen, respectively.
$M_{\mathrm{N_2}}$	Molar masses of nitrogen
M_{vap}, M_{air}	Molar masses of vapor and dry air, respectively
M_t	Miles traveled
$\dot{m}_{\mathrm{H_2}}$	Rate of hydrogen consumption
n^{fc}, n^{bt}	Number of cells in a fuel cell stack and a battery pack, respectively

$P^{\mathrm{fc}}_{\mathrm{net}}$	Power output from a fuel cell system
$P^{\mathrm{fc}}_{\mathrm{st}}$	Power generated from a fuel cell stack
$P^{\mathrm{fc}}_{\mathrm{con}}$	Power consumed by a fuel cell compressor
$\bar{P}^{\mathrm{fc}}_{\mathrm{con}}$	Power consumed by the unscaled fuel cell compressor
$P^{\mathrm{pt}}_{\mathrm{req}}$	Power required by the mechanical part of a vehicle
$P^{\mathrm{pt}}_{\mathrm{avl}}$	Power available from the electric part of a vehicle
P^{fc}, P^{bt}	Powers generated in a fuel cell and a battery, respectively
$P^{\mathrm{bt}}_{\mathrm{min}}$, $P^{\mathrm{bt}}_{\mathrm{max}}$	Minimum and maximum power available from the battery
P^{ent}	Price
$\bar{P^{\mathrm{ent}}}_{01\|02}$	Average of 2001 and 2002 market prices of the current conventional light truck design
p_{amb}	Ambient pressure
$p_{\mathrm{O_2,ca}}$	Oxygen partial pressure in a fuel cell cathode
$p_{\mathrm{vap,amb}}$	Partial pressures of vapor at the ambient
$p_{\mathrm{air,amb}}$	Partial pressures of dry air at the ambient
p_{cp}	Required pressure raise of the compressor
pr	Pulley speed ratio
q^{ent}	Quantity
R_0, R_p	Internal ohmic and polarization resistances of a battery, respectively
$\mathbf{r}^{\mathrm{fc}}$, $\mathbf{r}^{\mathrm{bt}}$, $\mathbf{r}^{\mathrm{pt}}$	Fuel cell, battery and powertrain design responses, respectively
r_x	Response for linking variable x
r^{ent}	Static inflation rate
rm	Rotor radius of a vehicle motor
S^{ent}	Fuel cost saving
$\mathrm{SC}^{\mathrm{fc}}$	Fuel cell specific cost

$\mathbf{t}^{\mathrm{fc}}$, $\mathbf{t}^{\mathrm{bt}}$, $\mathbf{t}^{\mathrm{pt}}$	Fuel cell, battery and powertrain design targets, respectively
t_x	Design target for linking variable x
t_f	End of driving schedule
t_{0-60}	0-60 mph time
V^{ent}	Net utility threshold
$v_{\mathrm{cl}}^{\mathrm{fc}}$	Cell voltage of a fuel cell
v_{act}, v_{ohm}	Overvoltage due to the activation and ohmic loss, respectively
v_{conc}	Overvoltage due to the concentration loss
$v_{\mathrm{net}}^{\mathrm{fc}}$, $v_{\mathrm{net}}^{\mathrm{bt}}$	Fuel cell and battery net voltage, respectively
W_{in}	Total mass flow rate of the inlet air
$\bar{W}_{\mathrm{in}}$	Inlet mass flow rate to the unscaled compressor
$W_{\mathrm{H_2,rea}}$	Rates of reacted hydrogen in a fuel cell
$W_{\mathrm{O_2,rea}}$	Rates of reacted oxygen in a fuel cell
$W_{\mathrm{O_2,in}}$	Inlet mass flow rates of oxygen to a fuel cell
$W_{\mathrm{N_2}}$	Inlet mass flow rates of nitrogen to a fuel cell
$W_{\mathrm{vap,in}}$	Inlet mass flow rates of vapor to a fuel cell
W^{fc}, W^{bt}	Fuel cell and battery pack weight, respectively
$w_{\mathrm{O_2}}$	Oxygen mass fraction in dry air
w^{mt}	Vehicle motor speed
w_{max}	Maximum value of vehicle motor speed
α	Speed of reversion
α_{ch}	Geometric scaling factor of reactant channels in length
α_{cp}	Geometric scaling factor in length
γ	Ratio of specific heats of air

η_{cp}	Fuel cell compressor efficiency
η^{bt}	Battery efficiency
θ_n, θ_p	Negative and positive insertion materials, respectively
λ	Oxygen excess ratio
$\lambda_{P^{\mathrm{ent}}}$	Price elasticity of demand
$\lambda_{S^{\mathrm{ent}}}$	Fuel cost saving elasticity of demand
π^{ent}	Gross profit
σ^{dsl}	Volatility of diesel fuel price
τ_{p}	Polarization time constant
τ^{mt}	Vehicle motor torque
$\tau_{\max}$	Maximum value of vehicle motor torque
$\tau_{\min}$	Minimum value of vehicle motor torque

CHAPTER I

Introduction

Uncertainty is ubiquitous because our knowledge is always limited. The effect of uncertainty can often be small enough to be ignored, while sometimes it is too risky not to take it into account. Especially when engineering products are designed or pushed to their limits for maximum performance, uncertainty in engineering design causes a variety of failures and malfunctions if it is not dealt with properly. Therefore, engineers always make decisions under various forms of uncertainty. Since many products today are large, complex systems, their design requires multidisciplinary analyses involving significant interactions that may include uncertain quantities due to uncertainty propagation between disciplines. Thus, we need to estimate the propagated uncertainty to study how the design will perform. Estimation of the propagated uncertainty is a numerically challenging task if the analysis function is nonlinear. Thus, solving the design problem with All-In-One (AIO) methods, where the system is treated as a fully integrated single problem, may not be practical or reliable for many problems. Moreover, the inclusion of uncertain quantities in these interactions can strongly couple subsystems to each other [8]. Thus, use of decomposition strategies in Multi-disciplinary Design Optimization (MDO) of such systems, where the system is broken down into several manageable subsystems

that are solved with traditional approaches, may be the only available solution approach. Decomposition strategies are classified as non-hierarchical or hierarchical, as shown in Figure 1.1. Strategies for non-hierarchical partitions, such as Collaborative Optimization (CO), Concurrent SubSpace Optimization (CSSO), and Bi-Level Integrated System Synthesis (BLISS), often use two levels: sub-problems typically representing different aspects (or disciplinary analyses) are optimized concurrently, while a system-level problem coordinates the interactions between the sub-problems [5, 11, 20, 37, 85, 86, 125]. On the other hand, hierarchical partitions contain multiple levels of subsystems (typically representing physical components). Figure 1.1 (b) shows an example of a hierarchically decomposed system in which each block represents an element constituting its parent (or the element at the upper level). Thus, elements in hierarchical decomposition are coupled only between a parent and its children while the interactions among elements with the same parents, the so-called siblings, are not linked directly to each other but are coordinated by their parent. This dissertation focuses on an MDO method for hierarchically decomposed systems under uncertainty.

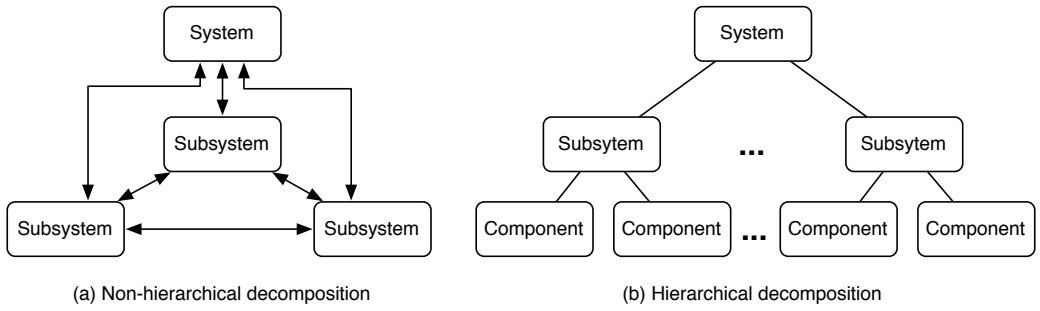

Figure 1.1: System decomposition approaches

1.1 Analytical Target Cascading and Probabilistic Analytical Target Cascading

Analytical Target Cascading (ATC) is an optimization method for multilevel hierarchical systems. A parent and its children are coupled by linking variables that contain design targets $\mathbf{t}_{ij}$ and analysis responses $\mathbf{r}_{ij}$. In a coordination strategy, a parent element cascades targets to its children (the elements at the lower level) while a child element tries to provide responses as close to these targets as possible. A typical ATC subproblem is shown in Figure 1.2. In the figure, subscript i and j are level and element indices, respectively. By updating the targets and response iteratively, ATC can obtain the solution with sufficient consistency.

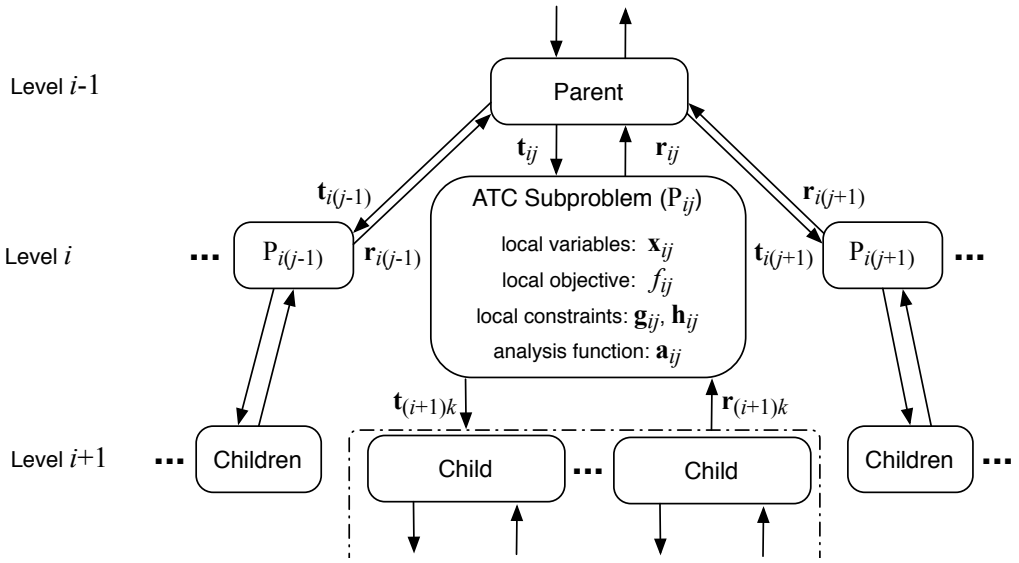

Figure 1.2: Example of ATC subproblem

Mathematically, the ATC process starts with an AIO problem formulation, prior

to any decomposition, expressed as:

$$\begin{aligned} \min_{\bar{\mathbf{x}}_{11},...,\bar{\mathbf{x}}_{NM}} \quad & \sum_{i=1}^{N}\sum_{j\in\mathcal{E}_i} f_{ij}(\bar{\mathbf{x}}_{ij}) \\ \text{subject to} \quad & \mathbf{g}_{ij}(\bar{\mathbf{x}}_{ij}) \leq \mathbf{0}, \quad \mathbf{h}_{ij}(\bar{\mathbf{x}}_{ij}) = \mathbf{0}, \\ \text{where} \quad & \bar{\mathbf{x}}_{ij} = [\mathbf{x}_{ij}, \mathbf{r}_{(i+1)k}], \quad \forall k \in \mathcal{C}_{ij}, \\ & \mathbf{r}_{ij} = \mathbf{a}_{ij}(\bar{\mathbf{x}}_{ij}), \quad \forall j \in \mathcal{E}_i, i = 1, ..., N, \end{aligned} \tag{1.1}$$

where N and M are the number of levels and elements, respectively. In Eq.(1.1), f_{ij}, $\mathbf{g}_{ij}$ and $\mathbf{h}_{ij}$ are the separated objective, inequality and equality constraints of element j at level i, respectively; $\mathcal{C}_{ij}$ is the set of children of element j at level i, and $\mathcal{E}_i$ is the set of elements at level i. The quantities $\mathbf{r}_{ij}$ are termed "response" of element j at level i resulting from the decision $\bar{\mathbf{x}}_{ij}$. Since the values from other elements in level $i+1$ are needed to evaluate f_{ij}, $\mathbf{g}_{ij}$, $\mathbf{h}_{ij}$ and $\mathbf{r}_{ij}$, the copies of $\mathbf{r}_{(i+1)k}$, represented as the "targets", $\mathbf{t}_{(i+1)k}$, are created to separate the elements. Consistency constraints are applied to make targets and responses consistent, namely,

$$\mathbf{c}_{ij} = \mathbf{t}_{ij} - \mathbf{r}_{ij} = \mathbf{0}. \tag{1.2}$$

The resulting modified AIO is expressed as:

$$\begin{aligned} \min_{\bar{\mathbf{x}}_{11},...,\bar{\mathbf{x}}_{NM}} \quad & \sum_{i=1}^{N}\sum_{j\in\mathcal{E}_i} f_{ij}(\bar{\mathbf{x}}_{ij}) \\ \text{subject to} \quad & \mathbf{g}_{ij}(\bar{\mathbf{x}}_{ij}) \leq \mathbf{0}, \quad \mathbf{h}_{ij}(\bar{\mathbf{x}}_{ij}) = \mathbf{0}, \\ & \mathbf{c}_{ij} = \mathbf{t}_{ij} - \mathbf{r}_{ij} = \mathbf{0}, \\ \text{where} \quad & \bar{\mathbf{x}}_{ij} = [\mathbf{x}_{ij}, \mathbf{t}_{(i+1)k}], \quad \forall k \in \mathcal{C}_{ij}, \\ & \mathbf{r}_{ij} = \mathbf{a}_{ij}(\bar{\mathbf{x}}_{ij}), \quad \forall j \in \mathcal{E}_i, i = 1, ..., N. \end{aligned} \tag{1.3}$$

Allowing inconsistencies among elements or relaxing the consistency constraints, $\mathbf{c}_{ij}$, enables a decomposition strategy. Specifically, the overall system can be consistent at convergence by minimizing the deviation between elements throughout the ATC

iterations. By monotonicity analysis [112], the consistency constraints are always active. Previous ATC formulations utilized three types of relaxations that were added to the objective: Quadratic Penalty (QP) [80, 105, 106], Ordinary Lagrangian (OL) [88] and Augmented Lagrangian (AL) relaxations [126]. Letting $\pi(\mathbf{t}_{ij} - \mathbf{r}_{ij})$ be a general constraint relaxation function and partitioning the problems, a typical ATC subproblem P_{ij} for element j at level i is formulated as:

$$\begin{aligned} \min_{\bar{\mathbf{x}}_{ij}} \quad & f_{ij}(\bar{\mathbf{x}}_{ij}) + \pi(\mathbf{c}_{ij}) + \sum_{k \in \mathcal{C}_{ij}} \pi(\mathbf{c}_{(i+1)k}) \\ \text{subject to} \quad & \mathbf{g}_{ij}(\bar{\mathbf{x}}_{ij}) \leq \mathbf{0}, \quad \mathbf{h}_{ij}(\bar{\mathbf{x}}_{ij}) = \mathbf{0}, \\ \text{where} \quad & \bar{\mathbf{x}}_{ij} = [\mathbf{x}_{ij}, \mathbf{t}_{(i+1)k}], \quad \forall k \in \mathcal{C}_{ij}, \\ & \mathbf{c}_{ij} = \mathbf{t}_{ij} - \mathbf{r}_{ij}, \quad \mathbf{c}_{(i+1)k} = \mathbf{t}_{(i+1)k} - \mathbf{r}_{(i+1)k} \\ & \mathbf{r}_{ij} = \mathbf{a}_{ij}(\bar{\mathbf{x}}_{ij}), \quad \forall j \in \mathcal{E}_i, i = 1, ..., N. \end{aligned} \tag{1.4}$$

While ATC has been successfully applied to several optimal design problems, only a few publications are available that solve hierarchical system design optimization problems under uncertainty due to the difficulty in incorporating uncertainty into linking variables. Using random variables to represent uncertainty, the so-called Probabilistic Analytical Target Cascading (PATC) has been formulated from the deterministic ATC by Kokkolaras et al.[84], and generalized with general probabilistic characteristics by Liu et al.[100]. The generalized PATC formulation for subproblem P_{ij} is expressed as:

$$\begin{aligned} \text{Given} \quad & \mathbf{T}_{ij}, \mathbf{R}_{(i+1)k}, \\ \min_{\bar{\mathbf{X}}_{ij}} \quad & \mathrm{E}[f_{ij}(\bar{\mathbf{X}}_{ij})] + \pi(\mathbf{T}_{ij} - \mathbf{R}_{ij}) + \pi(\mathbf{T}_{(i+1)k} - \mathbf{R}_{(i+1)k}) \\ \text{subject to} \quad & \Pr[\mathbf{g}_{ij}(\bar{\mathbf{X}}_{ij}) \leq \mathbf{0}] \geq \boldsymbol{\alpha}_{ij} \\ \text{where} \quad & \mathbf{R}_{ij} = \mathbf{a}_{ij}(\bar{\mathbf{X}}_{ij}), \quad \bar{\mathbf{X}}_{ij} = [\mathbf{X}_{ij}, \mathbf{T}_{(i+1)k}], \\ & \forall k \in \mathcal{C}_{ij}, \quad \forall j \in \mathcal{E}_i, i = 1, ..., N, \end{aligned} \tag{1.5}$$

where $\mathbf{X}_{ij}$, $\mathbf{T}_{ij}$ and $\mathbf{R}_{ij}$ are assumed to be the vectors of normal random variables and π is a general relaxation function. Since matching two random variables is not practically doable in most cases, system consistency of PATC is defined by the choice of random variable representation. In the previously published PATC formulations, the first few moments are used as targets and responses. Even with the first few moments, however, computing the solution is very expensive if response functions in child elements are nonlinear due to computational difficulty in estimating propagated uncertainty. Thus, this dissertation investigates a solution approach to improve the computational efficiency for PATC with sufficient accuracy.

1.2 Motivation

In probabilistic formulations, uncertainty is defined using random variables, assuming that their Probability Density Functions (PDFs) can be inferred. In other words, design variables, parameters or both can be random variables resulting in objective, constraint and analysis function values that are also random variables whose distributions need to be estimated to solve the problem. Estimating the propagated uncertainty, however, can be a very challenging and computationally expensive task for nonlinear functions. Even with a simple univariate function, the output of a nonlinear function is typically distributed differently from the distribution of the input, as illustrated in Figure 1.3 (a). For a linear function, obtaining the analytical expression of the output distribution can still be very demanding if the function contains multiple random variables. Suppose that X and Y are independent and have continuous distributions with densities f_X and f_Y respectively and $Z = X + Y$. Then the PDF of Z, f_Z can be obtained from the convolution of f_X and f_Y, expressed as

follows:

$$f_Z(z) = (f_X * f_Y)(z) = \int f_X(x) f_Y(z-x) dx \tag{1.6}$$

Thus, obtaining the exact value of Eq.(1.6) can still be challenging for arbitrary distributions. Since the convolution of independent normal distributions is normally distributed, however, the uncertainty propagation for a linear system with normally distributed inputs can be obtained efficiently, as presented in Figure 1.3 (b).

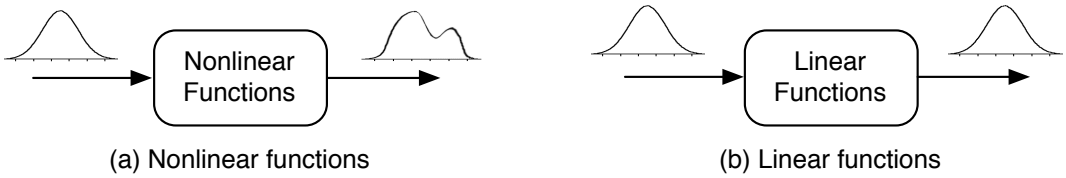

(a) Nonlinear functions (b) Linear functions

Figure 1.3: Uncertainty propagation through nonlinear and linear functions

In order to overcome the general difficulty in uncertainty propagation, Chan et al. [28] proposed the use of Sequential Linear Programming (SLP) to solve reliability based design optimization problems for a single system, with the goal of achieving an appropriate balance between accuracy, efficiency and convergence behavior. Thus, assuming that random design variables or parameters are normally distributed (or can be approximated to be normal distributions), the algorithm takes advantage of the simplicity and ease of uncertainty propagation for a linear system by linearizing and solving a problem successively.

The benefit of sequential linearization can be more significant for decomposed systems. As pointed out in Liu et al. [100], the choice of probabilistic characteristic is an important issue in MDO under uncertainty because it is not practical to match two distributions exactly. Thus, in the previous literature, the first few moments are used to maintain consistency in coupling variables, where coupling variables mean

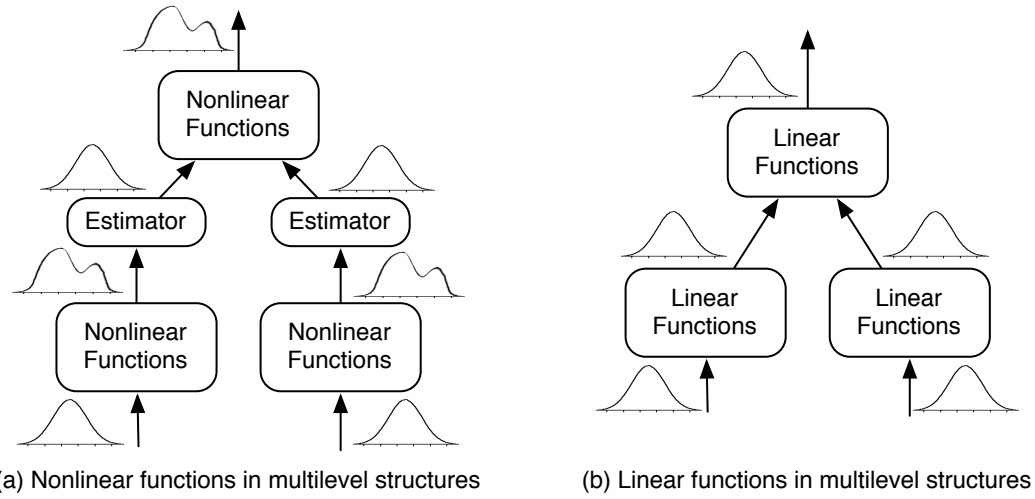

Figure 1.4: Benefit of sequential linearization in decomposition strategies

linking variables that are analysis outputs from one system and required to compute other systems. In order to obtain the first few moments, however, additional estimators between subsystems need to be used for coupling variables because the PDFs of linking variables are unknown, as illustrated in Figure 1.4 (a). The estimators typically require a considerable amount of computational cost, depending on the accuracy of estimation. On the other hand, once the system is approximated linearly and the random variables are normally distributed, the coupling variables also have normal distributions. In other words, no estimators are needed, as shown in Figure 1.4 (b).

1.3 Hybrid Electric Fuel Cell Vehicle Design

In order to understand the need for efficient coordination strategies for PATC, Figure 1.5 represents a Hybrid Electric Fuel Cell Vehicle (HEFCV) as an example of a hierarchically decomposed system. Similar to other types of vehicles, a HEFCV is a complex system consisting of a large number of subsystems represented by the

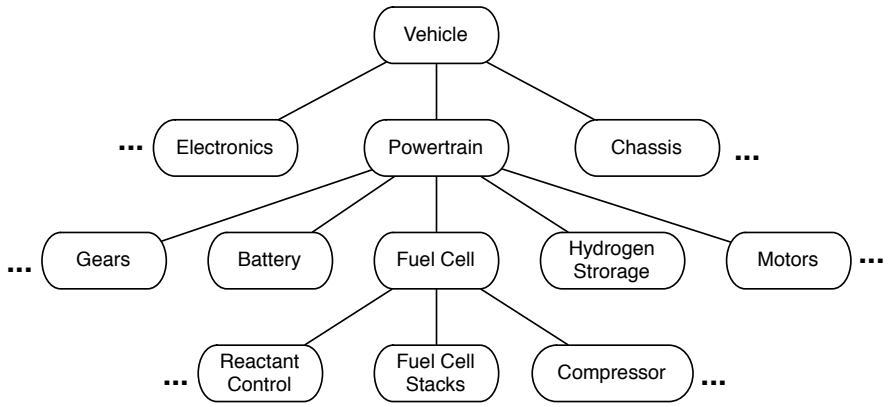

Figure 1.5: Representation of a hybrid electric fuel cell vehicle as a hierarchically decomposed system

blocks in the hierarchy. Because a large number of subsystems are involved, the HEFCV is likely to have considerable uncertainty sources in the engineering design problem. For example, manufacturing processes of subsystems can cause randomness in dimensions, such as cell thickness in fuel cells and battery cells. Because cells in fuel cell stacks and battery modules are stacked in series and pressed, the thickness of each cell can be varied depending on how uniformly the pressure is distributed over the stacks and modules. On the other hand, the cell thickness can be varied by in-use environmental parameters because the electrochemical reactions in the cells change in temperature, humidity and pressure. Moreover, since the rate of reactions is not uniform across the stacks and modules, the properties in the cells are not homogenous, which also causes randomness in cell thickness. In addition to random cell thicknesses, many other manufacturing processes and in-use environmental parameters are uncertain in engineering design problems, for which it is equally inappropriate and incorrect to use single deterministic values to represent the variable behavior.

Uncertainty does not only come from the inside of engineering problems (endogenous uncertainty) but also from the outside of engineering problems (exogenous uncertainty), such as the inconsistency of customer preferences and volatility of material and fuel costs. Exogenous uncertainty from customers is critical for new technologies because less information is available about how the market will react to the new technologies and more resources and costs are involved to introduce the new technologies. Therefore, in order to estimate the adaptability or feasibility of an alternative energy system such as fuel cells, we need to rely on market forces to shape our energy future rather than attempting to dictate what fuels are to be used, according to American Petroleum Institute President Red Cavaney, as quoted in the Senate Environment & Public Works Committee in November 2005 [71]. In other words, it is necessary to include an enterprise decision model connecting customer preferences and marketing decisions to engineering design problems [104].

1.4 Dissertation Objectives

In order to solve a hierarchical system design optimization problem under uncertainty, such as the HEFCV design problem, efficient approaches to coordinate PATC are required. Therefore, the objective of this dissertation is to contribute to the development of the approaches by exploiting sequential linearization. In this dissertation, we only consider uncertainty in design variables, leaving uncertainty in parameters outside our scope, because the proposed coordination strategies focus on uncertain linking variables that are added due to decomposition. The proposed coordination strategies and their proofs, however, are valid for both random design variables and parameters with minor notational modifications on subproblem for-

mulations. These uncertainties in terms of random variables are incorporated into the PATC framework and their effects on the interactions among subsystems are investigated. In order to achieve the goals, several areas will be focused on:

1. *Mathematical formulations of hierarchical decompositions for sequential linearization.* This dissertation introduces L_∞ norms for relaxation in order to make ATC and PATC linear and differentiable.

2. *Analytical methodologies for coordinating subsystems.* Using SLP algorithms and the Hierarchical Overlapping Coordination (HOC) strategy in [106], methodologies are developed to obtain an optimal solution for ATC and PATC formulations.

3. *Efficient methodologies for reducing computations.* Taking advantage of the properties of weakly-coupled elements, methodologies are devised to reduce the number of function evaluations.

4. *System-level formulation for application in Hybrid Electric Fuel Cell Vehicle (HEFCV).* Hierarchical design problems under uncertainty are formulated and utilized for HEFCV. This also addresses solving problems where multiple uncertainties exist in different subsystems.

1.5 Dissertation Overview

The remainder of this dissertation is organized as follows. Literature is reviewed in Chapter 2 in three categories: uncertainty propagation of random variables, design optimization under uncertainty and MDO under uncertainty. Chapter 3 discusses the SLP coordination strategy for ATC, including mathematical formulations and

convergence proofs. A suspension strategy is also introduced to reduce computations further. The SLP coordination strategy is extended to PATC in Chapter 4. The suspension strategy is applied again for the probabilistic formulation. Both Chapter 3 and Chapter 4 include analytical examples to show the efficiency and accuracy of the proposed methodologies. Chapter 5 demonstrates a comprehensive HEFCV design problem under uncertainty that includes fuel cell system, battery, vehicle and enterprise decision models. Chapter 6 concludes the dissertation and provides some ideas for future research.

CHAPTER II

Theoretical Background

2.1 Introduction

In this chapter, previous research on uncertainty in Multi-disciplinary Design Optimization (MDO) is reviewed, beginning with the representation and propagation of uncertainty and extending to the coordination of subproblems with uncertain variables. The first step to understanding how uncertainty affects design optimization is to represent uncertainty with mathematical models. Various uncertainty models exist in the literature for different application fields, which require different methods to estimate their propagation: e.g., interval models [107], convex models [15], fuzzy sets [144], and random variables [46, 113]. Here we focus on random variable models because they are a popular and effective way to define uncertainty in design optimization under uncertainty. The chapter starts with a review of random variables and how to estimate their propagation through objective and constraint functions in Section 2.2. Problem formulations for a single system are discussed in Section 2.3. After reviewing Analytical Target Cascading (ATC) formulations, Section 2.4 focuses on MDO methods under uncertainty, especially for Probabilistic Analytical Target Cascading (PATC).

2.2 Random Variables

Mathematically a random variable, X, is a measurable function from a probability space into a measurable space of possible values of the variable [46]. Therefore, the value of the random variable will vary as the experiment is repeated. A random variable requires an infinite number of measurements to infer its probability distribution. In practice, a sufficiently large number of measurements is assumed to be enough to infer the true probability distribution accurately.

If X can take an infinite number of possible values, X is called a continuous random variable, while a discrete random variable can take only a finite number of possible values. A Probability Density Function (PDF) is a common way to represent continuous random variables. A PDF, denoted as f_X, represents the frequency or probability of a random variable X being located within an interval $\mathbb{D}$, and satisfies the conditions

$$f_X(t) \geq 0 \quad \forall t \in \mathbb{D} \tag{2.1}$$

$$\int_{-\infty}^{\infty} f_X(t)dt = 1. \tag{2.2}$$

The probability of a continuous X being within the range $[a, b]$ can be calculated by integrating its PDF over the domain $[a, b]$, as shown in Eq.(2.3).

$$\int_{a}^{b} f_X(t)dt = \Pr[a \leq X \leq b] \tag{2.3}$$

On the other hand, for discrete random variables, a Probability Mass Function (PMF) of X, $p_X(x_i)$, is defined as the function that indicates the probability that X

is equal to x_i, and satisfies the following properties:

$$p_X(x_i) \geq 0 \ \forall x_i \in \mathbb{D}$$
$$\sum_i p_X(x_i) = 1. \tag{2.4}$$

In addition to the PDF, a Cumulative Distribution Function (CDF) describes the probability that a continuous random variable X takes on a value less than or equal to x and is expressed as

$$F_X(x) = \Pr[X \leq x] = \int_{-\infty}^{x} f_X(t)dt. \tag{2.5}$$

Similarly, a Cumulative Mass Function (CMF) for a discrete random variable is defined as follows.

$$F_X(x) = \Pr[X \leq x] = \sum_{i:x_i \leq x} p_X(x_i). \tag{2.6}$$

This dissertation considers continuous random variables only and leaves the rest of the models open for further investigation.

Due to the difficulty of realizing a distribution from PDF or CDF information, some parameters are used to characterize the distribution. The most common parameters are listed as follows.

- Expected value, $\mathrm{E}[X]$: the expected value (or mathematical expectation) of a random variable is the sum of the probability of each possible outcome multiplied by its value. For continuous X,

$$\mathrm{E}[X] = \mu_X = \int_{-\infty}^{\infty} t f_X(t)dt. \tag{2.7}$$

- Variance, $\mathrm{Var}[X]$: the variance of a random variable is a measure of its statistical dispersion, indicating how its possible values are spread around the expected

value.

$$\mathrm{Var}[X] = \mathrm{E}[(X - \mu_X)^2] \tag{2.8}$$

- Percentile, x^p : the 'p'th percentile is a value on a scale of one hundred that indicates the p percent of a distribution, which satisfies Eq.(2.9). For example, 5th percentile x^5 indicates that 5 % of the possible value of X are smaller than x^5. The 50th percentile is called the median.

$$F_X(x^p) = p\% \tag{2.9}$$

- Central moment, $\mathrm{E}[X - \mathrm{E}[X]^k]$: the 'k'th central moment in mathematics, evolved from the concept of a moment in physics, is defined as the quantity satisfying Eq.(2.10).

$$\mathrm{E}[X - \mathrm{E}[X]^k] = \int_{-\infty}^{\infty} (t - \mu_X)^k f_X(t) dt \tag{2.10}$$

Functions of Random Variables

If design variables or parameters are random variables with known distributions, the resulting values of objective, constraint and analysis functions are random variables whose distributions are unknown in general. For example, let Eq.(2.11) be a function of random variables $\mathbf{X} = \{X_1, ..., X_n\}$.

$$Y = g(\mathbf{X}) \tag{2.11}$$

If $g(\mathbf{X})$ is simply linear, the mean of Y, μ_Y, is simply the sum of μ_{X_i}. If $g(\mathbf{X})$ is simply linear and X_is are independent, the variance of Y is the sum of $\mathrm{Var}[X_i]$s. The PDF of the output Y, however, is defined as in Eq.(2.12).

$$\Pr[y \le Y \le y + dy] = \int_{y \le Y \le y+dy} \cdots \int f_Y(\mathbf{x}) d\mathbf{x} \tag{2.12}$$

Even if $g(\mathbf{X})$ is a univariate function, an analytical solution of Eq.(2.12) is difficult to obtain in general because the number of segments satisfying $y \leq Y \leq y + dy$ can be more than one, unless $g(\mathbf{X})$ is monotonic (as illustrated in Figure 2.1), and it is difficult to obtain $\mathbf{x} = g^{-1}(y)$ from $y = g(\mathbf{x})$, even if $g(\mathbf{x})$ is an analytical function. Since most engineering problems contain a number of nonlinear or multidimensional functions or even simulation-based functions, the direct calculation for an analytical solution is not plausible. Therefore, a number of numerical methods for calculating uncertainty propagation have been developed in various fields for different purposes. These methods can be classified into five categories: sampling techniques, local expansion, most probable point, functional expansion, and numerical integration methods [91]. We review these methods in more detail below.

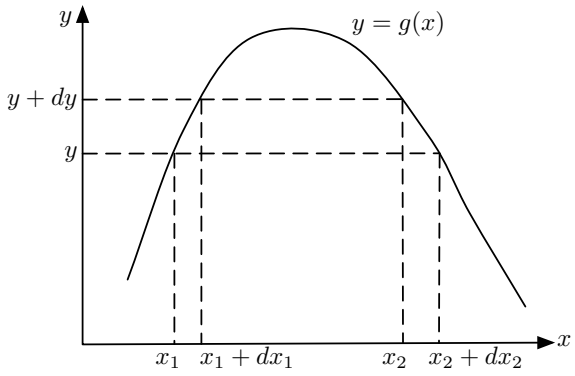

Figure 2.1: Direct Calculation (modified from [26])

2.2.1 Sampling Techniques

Due to its simplicity, several sampling approaches based on Monte Carlo Simulation (MCS) have been developed and widely used in engineering problems to estimate the output PDF of a model due to its simplicity [66]. MCS is able to obtain accurate $f_{\mathbf{X}}$ with a sufficiently large number of samples.

With more samples, MCS can capture the characteristics of a system function more accurately. Mathematically, the accuracy of Monte Carlo simulation has been calculated by Shooman [121], as in Eq.(2.13),

$$\epsilon\% = \sqrt{\frac{1 - p_f^T}{N \cdot p_f^T}} \cdot 200\%, \tag{2.13}$$

where p_f^T is the true probability of failure and N is the number of samples. From Eq.(2.13) the error ϵ is a function of both the number of simulations and the actual probability. However, the actual probability is usually unknown and MCS is utilized to approximate it. Thus, when MCS is applied to achieve an accurate estimation of the probability of failure, computational time becomes a significant challenge. For example, in a design problem with n random variables, n million random numbers are necessary if MCS is to successfully estimate the probability of failure [66].

Based on the above, MCS may not be a practical approach for design optimization problems that require a significant number of iterations. Several modification of MCS have been proposed to reduce the number of samples without sacrificing the simplicity and accuracy of MCS, including Quasi-Monte Carlo methods [130], Hammersly sampling techniques [42, 43], β-sphere importance sampling [68], stratified sampling [66] and adaptive sampling [75, 133, 134]. By sampling around regions of importance, these methods improve numerical efficiency, but the computational challenge remains high, particularly when the individual simulation cost is high.

2.2.2 Local Expansion Methods

The local expansion methods approximate $g(\mathbf{X})$ through first or second order Taylor series expansions or perturbation methods. The First Order Second Moment (FOSM) (sometimes called mean value method [137]) is the most popular method

in this category, approximating the nonlinear function at the design point $\mu_{\mathbf{X}}$ as expressed in Eq.(2.14).

$$\hat{g}_{\text{FOSM}} \approx g(\mu_{\mathbf{X}}) + \sum_{i=1}^{n} \left.\frac{\partial g}{\partial x_i}\right|_{\mu_{X_i}} \cdot (x - \mu_{X_i}) \tag{2.14}$$

Let X_i be independent normally random variables ($X_i \sim N(\mu_{X_i}, \sigma^2_{X_i})$, $\forall i = 1, ..., n$). If $g(\mathbf{X})$ is approximated linearly by Eq.(2.14), the output distribution of the approximated function is still a normal distribution with parameters as shown in Eq.(2.15).

$$\hat{g}_{\text{FOSM}}(\mathbf{X}) \sim N(\mu_g, \sigma_g^2) \text{ where } \begin{cases} \mu_g = g(\mu_{\mathbf{X}}) \\ \sigma_g^2 = \sum_{i=1}^{n} \left(\frac{\partial g}{\partial x_i}\right)^2 \sigma^2_{X_i} \end{cases} \tag{2.15}$$

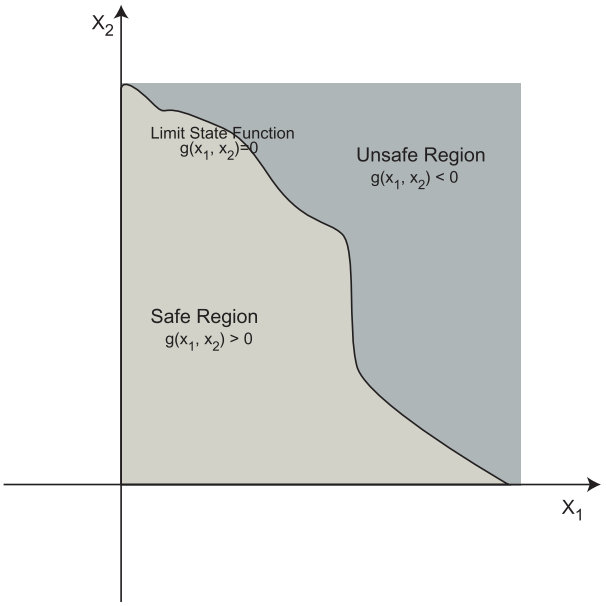

Figure 2.2: Example of limit state function

Let the constraint boundary $g(\mathbf{X}) = 0$ be the 'limit state' as shown in Fig. 2.2. In general, nonlinear limit state functions are approximated as linear or quadratic functions, and the probability of violating the limit states is approximated as the

probability of violating the approximated functions. The probability of violating the approximated functions can be calculated easily using the error function (erf) as shown in Eq.(2.16).

$$\begin{aligned} \Pr[g_j(\mathbf{X}) > 0] &= 1 - \int_{-\infty}^{0} \frac{1}{\sqrt{2\pi}\sigma_{g_j}} e^{-\frac{\left(t-\mu_{g_j}\right)^2}{2\sigma_{g_j}^2}} dt \\ &= 1 - \frac{1}{2}\left[1 + \operatorname{erf}\left(\frac{-\mu_{g_j}}{\sigma_{g_j}\sqrt{2}}\right)\right] \qquad (2.16) \\ &= 1 - \Phi\left(\frac{-\mu_{g_j}}{\sigma_{g_j}}\right), \qquad (2.17) \end{aligned}$$

where Φ is the CDF of a standard normal distribution ($N(0,1)$). Letting $\mathbf{U}$ be a standard normal vector ($U_i \sim N(0,1)$, $\forall i = 1, ..., n$), we have $\mathbf{U} = \frac{(\mathbf{X}-\boldsymbol{\mu}_{\mathbf{X}})}{\boldsymbol{\sigma}_{\mathbf{X}}}$. The term inside Φ in Eq.(2.17) is defined as the reliability index β that can be interpreted as the shortest distance from the design point to the approximated limit state in the $\mathbf{U}$ space [70] as illustrated in Fig. 2.3.

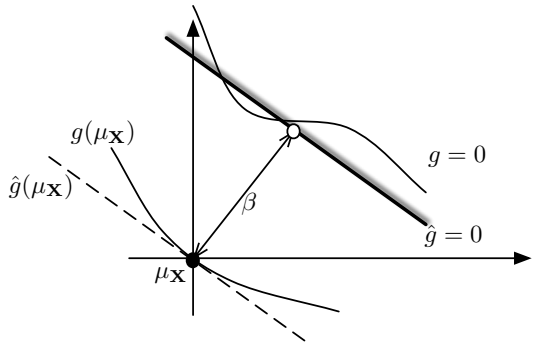

Figure 2.3: Approximated reliability index β by first order second moment

For non-normally distributed random variables, Rosenblatt [118] proposed a method to transfer their distributions into equivalent normal distributions with equivalent means and standard deviations ($N(\mu^e, \sigma^e)$). Then, the probability of violating a linear constraint can be written as $\Phi(-\beta^e)$. The Rosenblatt transformation is not applicable unless joint CDFs or conditional CDFs are given. Because complete in-

formation is not available in many industrial applications, Choi et al. [33] recently developed a new transformation technique using Nataf transformation to approximate joint CDFs or conditional CDFs. Note that these transformation methods can be used for other categories of uncertainty propagation.

Due to its simplicity, this approach is also referred to as fast reliability integration in the literature [69]. Since the approximation is made at the design point, success with this approach can be highly unpredictable depending on how the linear function is approximated. Wu [135] proposed an Advanced Mean Value method (AMV) to consider high order terms of Taylor series expansion and improve the accuracy of FOSM in the tail regions.

2.2.3 Most Probable Point Methods

Similar to the local expansion methods, methods in this category also approximate $g(\mathbf{X})$ through a first or second order Taylor series expansion. The difference is, however, that the approximation is made at the Most Probable Point (MPP) not at the mean. MPP is defined as a point that lies on the limit state having the shortest distance to the design point, which is interpreted to mean that the failure probability along the limit state is higher than at any other point. Thus, compared to the local expansion methods, the methods in this category require the solution of an additional optimization subproblem to find the MPP. Eq.(2.18) shows a formulation for this optimization subproblem, which is called the reliability index approach (RIA):

$$\begin{aligned} \min_{\mathbf{u}} \quad & \mathbf{u}^T\mathbf{u} \\ \text{s.t.} \quad & G(\mathbf{u}) = 0 \\ \text{where} \quad & \mathbf{u} = \frac{\mathbf{x} - \mu_{\mathbf{X}}}{\sigma_{\mathbf{X}}} \quad \text{and} \quad G(\mathbf{u}) = g(\mathbf{x}). \end{aligned} \tag{2.18}$$

The feasibility of a probabilistic constraint is determined by comparing the reliability index $\beta = \sqrt{\mathbf{u}^T\mathbf{u}}$ with a target reliability index $\beta^t = -\Phi^{-1}(p_{f_j})$. A probabilistic constraint is feasible if $\beta > \beta^t$.

The probability of violating the limit state function can also be reformulated as in Eq.(2.19), representing the approach proposed in [32], namely the Performance Measure Approach (PMA):

$$\begin{aligned} & \Pr[g(\mathbf{x}) \geq 0] = \Phi(-\beta) \leq p_f = \Phi(-\beta_t) \\ \Rightarrow \quad & F_g(0) = \Pr[g(\mathbf{x}) \geq 0] \leq \Phi(-\beta_t) \\ \Rightarrow \quad & G_{P_f} = F_g^{-1}(\Phi(-\beta_t)) \geq 0 \end{aligned} \tag{2.19}$$

where G_p is called the performance measure for PMA. This measure is further used as an index for the original reliability constraint in order to maintain the feasibility of the probabilistic constraint. Calculating this performance measure requires solving the optimization problem Eq.(2.20),

$$\begin{aligned} \min_{\mathbf{u}} \quad & G(\mathbf{u}) \\ \text{s.t.} \quad & \|\mathbf{u}\| = \beta^t. \end{aligned} \tag{2.20}$$

RIA is a commonly used and well-developed approach. However, since the convergence of reliability analysis using PMA is inherently more robust and efficient than RIA, PMA is usually preferred [4, 19, 34, 140, 141].

In order to apply the MPP methods to optimization problems with probabilistic constraints, two coupled optimization loops need to be solved. A nested MPP loop needs to be solved for every iteration of the outer optimization loop. In order to reduce computational costs related to the nested optimization, a lot of effort has

been made to develop efficient methods for the MPP loop, such as the advanced mean value method [136], hybrid mean value method [142], sequential optimization and reliability analysis [50], and the design potential method [127]. Also optimality conditions of the MPP subproblem are integrated in the outer problem as equality constraints, which turns double loop problems into "single loop" ones [31, 95].

Once the MPP is obtained, the approximation is made at the MPP after converting the design variables into a **U** space representation: the First Order Reliability Method (FORM) creates a linear approximation, as expressed in Eq. (2.21), while the Second Order Reliability Method (SORM) includes the curvature of the nonlinear limit state function, as expressed in Eq.(2.22).

$$\hat{g}_{\text{FORM}} \approx g(\mathbf{x}_{\text{MPP}}) + \nabla g^T(\mathbf{x}_{\text{MPP}}) \cdot (\mathbf{X} - \mathbf{x}_{\text{MPP}}), \tag{2.21}$$

$$\hat{g}_{\text{SORM}} \approx g(\mathbf{x}_{\text{MPP}}) + \nabla g^T(\mathbf{x}_{\text{MPP}}) \cdot (\mathbf{X} - \mathbf{x}_{\text{MPP}}) + \frac{1}{2}(\mathbf{X} - \mathbf{x}_{\text{MPP}})^T \cdot \nabla^2 g(\mathbf{x}_{\text{MPP}}) \cdot (\mathbf{X} - \mathbf{x}_{\text{MPP}}). \tag{2.22}$$

FORM can estimate the probability of failure efficiently but the results may not be accurate enough to be used for design problems [36] with highly nonlinear limit state functions. In order to overcome this limitation, several methods have been proposed to modify the FORM formulation, including a combination of safety factors and failure probability [25], and an alternative reliability index with curvature information [41, 129].

On the other hand, SORM can improve the accuracy of probability estimation by considering the Hessian of the constraint $g(\mathbf{X})$ at the MPP. Since the Hessian is required, SORM increases the cost of computation significantly relative to FORM. Historical development of SORM can be found in [21, 22, 55]. Discussions about

applicable ranges of FORM and SORM are presented in [146]. An alternative SORM is proposed by Zhao et al. [147, 148]. FORM/SORM is applicable for general non-normal random variables using transformations discussed in Section 2.2.2.

2.2.4 Numerical Integration Methods

In addition to sampling and expansion techniques, uncertainty propagation in system optimization output can be obtained by numerical integration methods. In these methods, statistical moments are calculated by moment-matching equations and used to approximate the PDF from empirical distribution systems, such as the Pearson family. The numerical integration methods rely on the principle that the first few moments of a random variable will adequately describe the complete PDF of the variable. While the PDF contains all the information on a random variable, occasionally, an engineering application does not require all this information but only excerpts that sufficiently characterize the distribution. In practice, this means that computing some moments of the distribution will be sufficient.

Let $f_{\mathbf{X}}$ be the joint PDF of the n dimensional vector of random variables $\mathbf{X}$. If $n = 1$, the kth center moment of $g(\mathbf{X})$ can be approximated by the m-node Gaussian type integration rule for statistical moments, expressed as

$$\mathrm{E}\big[g^k\big] = \int_{-\infty}^{\infty} \big\{g(x)\big\}^k f_X(x)dx \approx \sum_{i=1}^{m} w_i \big[g(\mu_X + \alpha_i \sigma_X)\big]^k, \tag{2.23}$$

where α_i, w_i are the location parameters and weights at the ith quadrature point. By letting $g(X) = X - \mu_X$, the solutions of α_i, w_i can be obtained using the moment-matching equation, expressed as

$$k^{th} \text{ moment}: \; M_k = \int_{-\infty}^{\infty} (x - \mu_X)^k f_X(x)dx = \sum_{i=1}^{m} w_i (\alpha_i \sigma_X)^k \quad \text{for} \quad k = 0, ..., 2m-1, \tag{2.24}$$

where M_k should be given from the input distribution. Even though solving $2m$ equations of Eq.(2.24) is not a simple task, they can be directly derived from the Gauss-Hermite, Gauss-Legendre, and Gauss-Laguerre quadrature formulas, if X is the normal, uniform and exponential distribution, respectively.

If $g(\mathbf{X})$ is a n dimensional function, Eq.(2.23) can be expanded as

$$\begin{aligned} \mathrm{E}\big[g^k\big] &= \int_{-\infty}^{\infty} \cdots \int_{-\infty}^{\infty} \big\{g(x_1, \cdots, x_n)\big\}^k f_X(x_1, \cdots, x_n) dx \\ &\approx \sum_{i_1=1}^{m} w_{i_1} \big[g(\mu_{X_1} + \alpha_{i_1}\sigma_{X_1}, \cdots \mu_{X_n})\big]^k \cdots \sum_{i_n=1}^{m} w_{i_n} \big[g(\mu_{X_1}, \cdots, \mu_{X_n} + \alpha_{i_n}\sigma_{X_n})\big]^k, \end{aligned} \tag{2.25}$$

where α_{i_j} and w_{i_j} can be provided by solving Eq.(2.24) for X_j. Because the number of function evaluations is m^n, similar to a full factorial design in the DOE point of view, this method is named as the Full Factorial Moment Method (FFMM) [92, 93] or the Full Factorial Numerical Integration (FFNI) [91]

The computational cost of FFMM or FFNI is exponential in the number of variables. In order to calculate the kth moment of $g(\mathbf{X})$ with fewer samples, a Univariate Dimension Reduction (UDR) method was developed recently [117, 138], where the multi-dimensional moment integral of Eq.(2.25) is computed by multiple reduced-dimensional integrals based on additive decomposition of the performance function as follows:

$$\begin{aligned} \mathrm{E}\big[g^k\big] \approx \mathrm{E}\big[\hat{g}^k\big] &= \mathrm{E}\left[\left\{\sum_{i=1}^{n} g_i(x_i) - (n-1)g(\mu_{\mathbf{X}})\right\}^k\right] \\ &= \int_{-\infty}^{\infty} \left\{\sum_{i=1}^{n} g_i(x_i) - (n-1)g(\mu_{\mathbf{X}})\right\}^k f_{X_i}(x_i) dx_i, \\ &\quad \text{where} \quad g_i(x_i) = g(\mu_{X_1}, ..., x_i, ...\mu_{X_n}). \end{aligned} \tag{2.26}$$

Using a bionomial formula, evaluation of Eq.(2.26) can be performed algebraically by recursively executing one-dimensional integration. The number of function evalu-

ations required is less than $mn+1$, increasing linearly with the number of variables. Youn et al. [143] recently developed the Eigenvector Dimension Reduction (EDR) method using $2n+1$ or $4n+1$ axial-DOE so that m is maintained at values 2 or 4 for large-scale problems. Also, the accuracy of probability estimation at the tail distribution can be improved by applying UDR methods at MPP [89].

Once the four statistical moments are obtained, the complete PDF of $Y = g(\mathbf{X})$, f_Y, can be evaluated from the empirical distribution systems. The Pearson family of distributions, one of the most common moment-matching methods, is described by [114] as

$$\frac{d\hat{f}_Y}{dx} = -\frac{a+x}{c_0 + c_1 x + c_2 x^2}\hat{f}_Y. \tag{2.27}$$

The moment-matching method for the Pearson family states that $\hat{f}_Y$ can represent the real PDF of the output, f_Y, if all the coefficients a, c_0 , c_1 , c_2 are found so that the first four moments of the system output match the first four moments of the Pearson distribution.

Numerical integration methods are robust against the non-normality of inputs based on the comparative study in [91]. Also, UDR and EDR methods can be efficient, especially when interactions between variables are weak.

2.3 Design Optimization under Uncertainty

Deterministic design optimization problems can be considered as the task to find the optimal design variable values $\mathbf{x}_*$ that minimize the objective function f while at the same time satisfying inequality constraints $\mathbf{g}$ and equality constraints $\mathbf{h}$, where variables $\mathbf{x}$ vary within lower bounds $\mathbf{x}_l$ and upper bounds $\mathbf{x}_u$ [112], as expressed in

Eq.(2.28).

$$\begin{aligned} \text{minimize} \quad & f(\mathbf{x};\mathbf{p}) \\ \text{with respect to} \quad & \mathbf{x} \\ \text{subject to} \quad & \mathbf{g}(\mathbf{x};\mathbf{p}) \leq 0, \quad \mathbf{h}(\mathbf{x};\mathbf{p}) = 0 \\ & \mathbf{x}_l \leq \mathbf{x} \leq \mathbf{x}_u. \end{aligned} \tag{2.28}$$

Here $\mathbf{p}$ is a vector of parameters that are not controllable by the designer. Solving Eq.(2.28) often leads to a solution on the boundary of the design space [112], thus leaving little room for uncertainty. Therefore, the deterministic optimal solution will tend to violate constraints and result in unexpected deviation from the intended performance in the presence of variations in the environment, such as temperature or humidity, applied external forces and manufacturing process outputs.

Robust design methods have been developed in order to improve the robustness and reliability of design solutions in the presence of uncertainty. When a formulation as in Eq. (2.28) is used, an optimizer finds the solution where the objective function f is minimal. Let the design variables and parameters be independent normal random variables, denoted by $\mathbf{X} \sim N(\boldsymbol{\mu}_{\mathbf{X}}, \boldsymbol{\sigma}_{\mathbf{X}})$ and $\mathbf{P} \sim N(\boldsymbol{\mu}_{\mathbf{P}}, \boldsymbol{\sigma}_{\mathbf{P}})$, respectively. If $\boldsymbol{\mu}$ is set to the optimal solution from Eq. (2.28), then the objective and constraint functions are random variables whose mean values equal to the values obtained from Eq. (2.28). The variances of the objective and constraints depend on the characteristics of the design problem. Conceptually, the designer finds out the tradeoff between minimizing the mean and the variance of the objective function without violating constraints under uncertainty. Mathematically this can be expressed as a

bi-objective optimization problem expressed as follows.

$$\begin{aligned} \min_{\mathbf{X}} \quad & [\mu_f, \sigma_f] \\ \text{subject to} \quad & \boldsymbol{\mu}_{\mathbf{g}} + k\boldsymbol{\sigma}_{\mathbf{g}}^2 \leq 0 \\ & \mathbf{x}_l \leq \boldsymbol{\mu}_{\mathbf{X}} \pm k\boldsymbol{\sigma}_{\mathbf{X}}^2 \leq \mathbf{x}_u. \end{aligned} \tag{2.29}$$

Here k indicates a user-defined constant that depends on the design purpose. The variances of objective and constraints can be calculated based on first order Taylor series expansion, expressed as

$$\begin{aligned} \sigma_f^2 &= \sum_{i=1}^{n} \left(\frac{\partial f}{\partial x_i}\right)^2 \sigma_{X_i}^2 + \sum_{i=1}^{m} \left(\frac{\partial f}{\partial p_i}\right)^2 \sigma_{P_i}^2 \\ \boldsymbol{\sigma}_{\mathbf{g}}^2 &= \sum_{i=1}^{n} \left(\frac{\partial \mathbf{g}}{\partial x_i}\right)^2 \sigma_{X_i}^2 + \sum_{i=1}^{m} \left(\frac{\partial \mathbf{g}}{\partial p_i}\right)^2 \sigma_{P_i}^2 \end{aligned} \tag{2.30}$$

where n and m are the numbers of design variables and parameters, respectively. Since this approach is based on first order Taylor series, the variations in Δx_i and Δp_i are assumed to be small.

Emch and Parkinson [52] provide a worst-case tolerance within which the design never fails. The worst-case concept assumes that uncertainty sources are independent and the largest variation for each source of uncertainty occurs at the worst-case design point. This approach is a conservative way to provide a solution for robust design. Using statistical analysis, several formulations have been suggested [14, 29, 48, 90, 145], and also applied to multidisciplinary systems [30, 63, 74]. Generalization of the robust design formulation with expectations, variances or their combination in objective function and constraints, has also been made by [39]. Most formulations for robust design require the low-order moments (means and variances) of objective and constraint functions that can be obtained efficiently by local expansion methods and numerical integration methods.

On the other hand, Reliability Based Design Optimization (RBDO) focuses on the probability of constraint violation or the probability of failure, usually denoted as p_f. In RBDO, any constraint that contains random variables is transformed from a deterministic to a probabilistic form. Eq. (2.31) shows a probabilistic formulation,

$$\begin{aligned} \min \quad & \mathrm{E}[f(\mathbf{x}, \mathbf{p}, \mathbf{X}, \mathbf{P})] \\ \text{with respect to} \quad & \mathbf{x}, \mathbf{X} \\ \text{subject to} \quad & \Pr[g_i(\mathbf{x}, \mathbf{p}, \mathbf{X}, \mathbf{P}) \geq 0] \leq p_{f_i}, \\ & g_j(\mathbf{x}, \mathbf{p}) \leq 0, \end{aligned} \tag{2.31}$$

where $\mathbf{x}$ and $\mathbf{p}$ are deterministic design variables and parameters, respectively, while $\mathbf{X}$ and $\mathbf{P}$ are probabilistic design variables and parameters, respectively. Inequality constraints are also separated into deterministic and probabilistic constraints. Constraints that contain no random variables remain in their deterministic form, while constraints involving random variables are reformulated into probabilistic equations. A probabilistic constraint states that the probability of violating the constraint is below a given threshold p_{f_i}. Since $\mathbf{p}_f$ in Eq.(2.31) is typically significantly small, the accuracy at the tail distribution is more important than the low-order moment. Thus, the MPP methods can be efficient in general but the FFNI approach or functional expansion methods can be more useful for highly nonlinear problems.

2.4 Analytical Target Cascading and Analytical Target Cascading under Uncertainty

Analytical Target Cascading (ATC) is an optimization method for multilevel hierarchical systems typically partitioned into physical subsystems or objects (see Figure 2.4) [80]. Each block in the hierarchical structure is referred to as an element and is an optimization sub-problem. An element can be coupled with only one parent

element but with multiple children elements. The interactions among elements with the same parents, the so-called siblings, are not linked directly to each other but are coordinated by their parent. The linking variables between a parent and children are design targets $\mathbf{t}_{ij}$ and analysis responses $\mathbf{r}_{ij}$. Targets are set by parents and propagated to their children; the children solve a minimum deviation optimization problem to obtain responses that are as close to the targets as possible. Thus, targets and responses are updated and coordinated iteratively to achieve consistent values within all elements where they appear. ATC has been successfully applied to a variety of optimal design problems [35, 78, 79, 80, 81, 83, 101, 104].

Mathematically, the ATC process starts with an AIO problem formulation, prior to any decomposition, expressed as:

$$\begin{aligned} \min_{\bar{\mathbf{x}}_{11},\ldots,\bar{\mathbf{x}}_{NM}} \quad & \sum_{i=1}^{N}\sum_{j\in\mathcal{E}_i} f_{ij}(\bar{\mathbf{x}}_{ij}) \\ \text{subject to} \quad & \mathbf{g}_{ij}(\bar{\mathbf{x}}_{ij}) \leq \mathbf{0}, \quad \mathbf{h}_{ij}(\bar{\mathbf{x}}_{ij}) = \mathbf{0}, \\ \text{where} \quad & \bar{\mathbf{x}}_{ij} = [\mathbf{x}_{ij}, \mathbf{r}_{(i+1)k}], \quad \forall k \in \mathcal{C}_{ij}, \\ & \mathbf{r}_{ij} = \mathbf{a}_{ij}(\bar{\mathbf{x}}_{ij}), \quad \forall j \in \mathcal{E}_i, i = 1, ..., N. \end{aligned} \tag{2.32}$$

In Eq.(2.32), f_{ij}, $\mathbf{g}_{ij}$ and $\mathbf{h}_{ij}$ are the separated objective, inequality and equality constraints of element j at level i, respectively; $\mathcal{C}_{ij}$ is the set of children of element

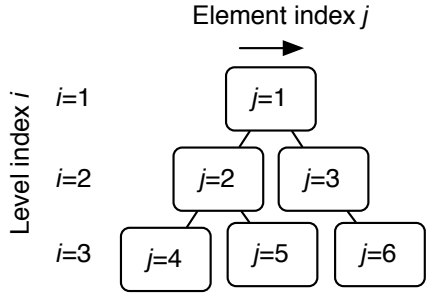

Figure 2.4: Example of index notation for a hierarchically partitioned design problem

j at level i, and $\mathcal{E}_i$ is the set of elements at level i. The quantities $\mathbf{r}_{ij}$ are termed "response" of element j at level i resulting from the decision $\bar{\mathbf{x}}_{ij}$. Due to the functional dependency of f_{ij}, $\mathbf{g}_{ij}$, $\mathbf{h}_{ij}$ and $\mathbf{r}_{ij}$ on $\mathbf{r}_{(i+1)k}$, each element is not separable. In other words, an element j at level i cannot be evaluated separately because the values from other elements in level $i+1$ are needed to evaluate the functions in the element. In order to separate the elements, the copies of $\mathbf{r}_{(i+1)k}$, represented as the "targets", $\mathbf{t}_{(i+1)k}$, are created. Consistency constraints are applied to make targets and responses consistent, namely,

$$\mathbf{c}_{ij} = \mathbf{t}_{ij} - \mathbf{r}_{ij} = \mathbf{0}. \tag{2.33}$$

The resulting modified AIO is expressed as:

$$\begin{aligned} \min_{\bar{\mathbf{x}}_{11},\ldots,\bar{\mathbf{x}}_{NM}} \quad & \sum_{i=1}^{N}\sum_{j\in\mathcal{E}_i} f_{ij}(\bar{\mathbf{x}}_{ij}) \\ \text{subject to} \quad & \mathbf{g}_{ij}(\bar{\mathbf{x}}_{ij}) \leq \mathbf{0}, \quad \mathbf{h}_{ij}(\bar{\mathbf{x}}_{ij}) = \mathbf{0}, \\ & \mathbf{c}_{ij} = \mathbf{t}_{ij} - \mathbf{r}_{ij} = \mathbf{0}, \\ \text{where} \quad & \bar{\mathbf{x}}_{ij} = [\mathbf{x}_{ij}, \mathbf{t}_{(i+1)k}], \quad \forall k \in \mathcal{C}_{ij}, \\ & \mathbf{r}_{ij} = \mathbf{a}_{ij}(\bar{\mathbf{x}}_{ij}), \quad \forall j \in \mathcal{E}_i, i = 1, ..., N. \end{aligned} \tag{2.34}$$

Allowing inconsistencies among elements or relaxing the consistency constraints, $\mathbf{c}_{ij}$, enables a decomposition strategy. Specifically, the overall system can be consistent at convergence by minimizing the deviation between elements throughout the ATC iterations. By monotonicity analysis [112], the consistency constraints are always active. Previous ATC formulations utilized three types of relaxations that were added to the objective: Quadratic Penalty (QP) [80, 105, 106], Ordinary Lagrangian (OL) [88] and Augmented Lagrangian (AL) relaxations [126]. Letting $\pi(\mathbf{t}_{ij} - \mathbf{r}_{ij})$ be a general constraint relaxation function and partitioning the problems, a typical

ATC subproblem P_{ij} for element j at level i is formulated as:

$$\begin{aligned}
\min_{\bar{\mathbf{x}}_{ij}} \quad & f_{ij}(\bar{\mathbf{x}}_{ij}) + \pi(\mathbf{c}_{ij}) + \sum_{k \in \mathcal{C}_{ij}} \pi(\mathbf{c}_{(i+1)k}) \\
\text{subject to} \quad & \mathbf{g}_{ij}(\bar{\mathbf{x}}_{ij}) \leq \mathbf{0}, \quad \mathbf{h}_{ij}(\bar{\mathbf{x}}_{ij}) = \mathbf{0}, \\
\text{where} \quad & \bar{\mathbf{x}}_{ij} = [\mathbf{x}_{ij}, \mathbf{t}_{(i+1)k}], \quad \forall k \in \mathcal{C}_{ij}, \\
& \mathbf{c}_{ij} = \mathbf{t}_{ij} - \mathbf{r}_{ij}, \quad \mathbf{c}_{(i+1)k} = \mathbf{t}_{(i+1)k} - \mathbf{r}_{(i+1)k} \\
& \mathbf{r}_{ij} = \mathbf{a}_{ij}(\bar{\mathbf{x}}_{ij}), \quad \forall j \in \mathcal{E}_i, i = 1, ..., N.
\end{aligned} \tag{2.35}$$

Since ATC enforces the consistency of values shared between elements by using relaxation functions, the proper choice of relaxation functions and associated weights is critical for solution convergence. For quadratic penalty functions, large weights are required to obtain accurate and consistent solutions [18]. Similar to other decomposition strategies, ATC typically is more expensive than AIO (if the latter could be used to obtain a solution) due to the coordination overhead. Michalek et al. [105] developed an iterative method for updating weights, which finds minimal weights to achieve a given level of inconsistency, especially important for problems with unattainable system targets. Still, the inner loop coordination, where the decomposed ATC problems are solved iteratively, is computationally expensive. To address this, Tosserams et al. [126] introduced an Augmented Lagrangian relaxation function and an alternating direction solution method, resulting in significant reduction of computational cost. Recently, a Diagonal Quadratic Approximation (DQA) method and a Truncated DQA (TDQA) method were applied to the augmented Lagragian relaxation function [94]. In DQA and TDQA, subproblems are fully separated and require the value of linking variables at the previous inner/outer loop iteration. Thus, the DQA methods can solve subproblems in parallel.

In addition to relaxation functions, coordination strategies are also critical for

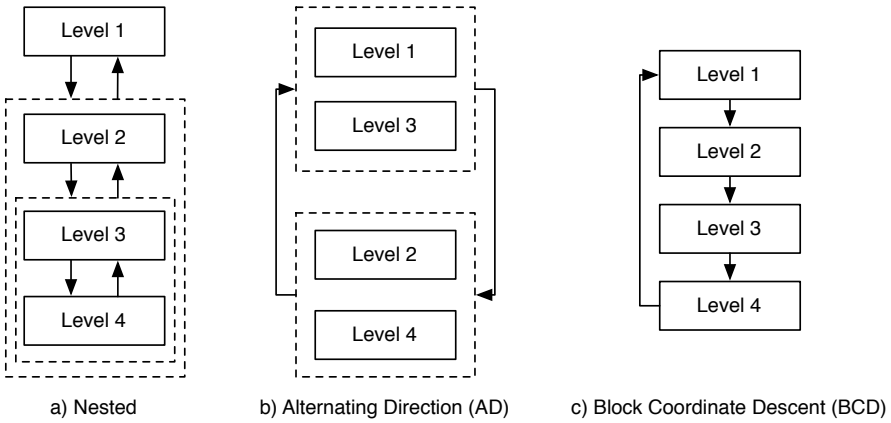

Figure 2.5: ATC coordination strategy

global and local convergence. To date, three coordination strategies have been used for global convergence proofs, namely, the Hierarchical Overlapping Coordination (HOC) strategy, the Alternating Direction (AD) strategy and the Block Coordinate Descent (BCD) strategy. The original convergence proof for ATC is based on HOC where subproblems are solved in a bi-level fashion [106]. Figure 2.5 (a) shows the bottom-up solution in HOC. On the other hand, AD solves odd levels and even levels separately so that subproblems in these levels can be calculated in parallel, as illustrated in Figure 2.5 (b) [126]. Also, Figure 2.5 (c) demonstrates BCD where each subproblem is solved sequentially and iteratively [94]. Note that the OL relaxation, DQA and TDQA methods do not require a coordination strategy because values for the linking variables in these methods are obtained from the previous iteration. According to [94], AL-AD and TDQA perform better than the other methods in general.

Compared to deterministic MDO, little research has been conducted to discuss and resolve the issue of uncertainty involved within the MDO context. Sues et al. [124] utilized stochastic optimization along with a response surface approach to re-

solve this uncertainty embedded within a multidisciplinary system. Batill et al. [13] indicated the challenges to be faced for uncertainty analysis within a multidisciplinary optimization problem. Gu et al. [63] proposed worst-case propagated uncertainty analysis and robust optimization. In [49], two approaches, namely, System Uncertainty Analysis (SUA) and Concurrent SubSystem Uncertainty Analysis (CSSUA), are proposed to improve the efficiency of uncertainty propagation within one coupled multidisciplinary problem.

- SUA: Based on information about the linking variables between disciplines, system level analysis is required to compute the impact of linking variables on each discipline. By using Taylor series expansion to the first order with respect to the mean value of linking and all input variables, the variation of subsystem outputs can be calculated from Eq. (2.36):

$$\Delta z_i = \sum_{\substack{j=1 \\ j \neq i}}^{n} \frac{\partial \mathbf{F}_{zi}}{\partial \mathbf{y}_j} \Delta \mathbf{y}_j + \frac{\partial \mathbf{F}_{zi}}{\partial \mathbf{x}_s} \Delta \mathbf{x}_s + \frac{\partial \mathbf{F}_{zi}}{\partial \mathbf{x}_i} \Delta \mathbf{x}_i + \Delta \epsilon_{zi}. \tag{2.36}$$

  Here $\mathbf{x}_i$ and $\mathbf{x}_s$ are vectors of input and linking variables, respectively. This calculation decouples linking variables between disciplines that help to parallelize the computation.

- CSSUA: In order to avoid computationally expensive system-level analysis in SUA, the mean value of each linking variable is computed in parallel by creating a sub-optimization problem, as presented in Figure 2.6.

This sub-optimization problem removes the necessity of system analysis. The variation of linking variables and subsystem outputs are found by the same approach as SUA. The links are decoupled to improve the efficiency of the computation.

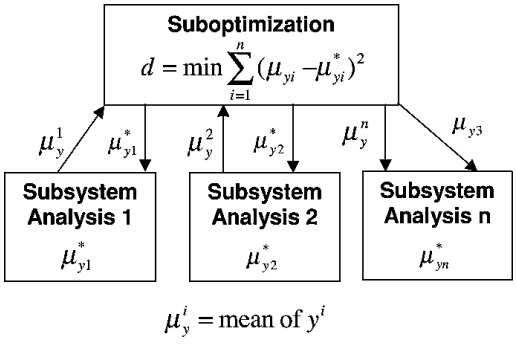

Figure 2.6: Sub-optimization for uncertainty analysis in the CSSUA (adapted from[49])

Collaborative reliability analysis is proposed by Du and Chen to improve the efficiency of reliability analysis for MDO under uncertainty [51]. In this analysis, a single loop procedure, combining the traditional MPP procedure with collaborative disciplinary analyses, is used to automatically satisfy the interdisciplinary consistency in reliability analysis.

Most of the research associated with MDO under uncertainty is focused on how to qualitatively define the problem of uncertainty within MDO instead of providing a generic solution. Yet little attention had been given to hierarchical system design. In order to provide an approach for hierarchical system optimization under uncertainty, deterministic ATC has been extended to probabilistic formulations, the so-called Probabilistic Analytical Target Cascading (PATC), by Kokkolaras et al. [84] using mean values to represent random linking variables. Liu et al. [100] generalized the formulation with general probabilistic characteristics. The generalized PATC

formulation for subproblem P_{ij} with a quadratic penalty function is expressed as:

$$\begin{aligned}
\text{Given} \quad & \mathbf{T}_{ij}, \mathbf{R}_{(i+1)k}, \\
\min_{\bar{\mathbf{X}}_{ij}} \quad & \mathrm{E}[f_{ij}(\bar{\mathbf{X}}_{ij})] + ||\mathbf{w}_{ij} \circ (\mathbf{T}_{ij} - \mathbf{R}_{ij})||_2^2 \\
& + \sum_{k \in \mathcal{C}_{ij}} ||\mathbf{w}_{(i+1)k} \circ (\mathbf{T}_{(i+1)k} - \mathbf{R}_{(i+1)k})||_2^2 \\
\text{subject to} \quad & \Pr[\mathbf{g}_{ij}(\bar{\mathbf{X}}_{ij}) \leq \mathbf{0}] \geq \boldsymbol{\alpha}_{ij} \\
\text{where} \quad & \mathbf{R}_{ij} = \mathbf{a}_{ij}(\bar{\mathbf{X}}_{ij}), \quad \bar{\mathbf{X}}_{ij} = [\mathbf{X}_{ij}, \mathbf{T}_{(i+1)k}], \\
& \forall k \in \mathcal{C}_{ij}, \quad \forall j \in \mathcal{E}_i, i = 1, ..., N,
\end{aligned} \tag{2.37}$$

where $\mathcal{C}_{ij}$ is the set of the children of element j at level i and $\mathcal{E}_i$ is the set of elements at level i. In Eq.(2.37), the $\circ$ operation indicates the component-wise multiplication of two vectors such that $\{a_1, ..., a_k\}^T \circ \{b_1, ..., b_k\}^T = \{a_1 b_1, ..., a_k b_k\}^T$.

Note that $\mathbf{X}_{ij}$, $\mathbf{T}_{ij}$ and $\mathbf{R}_{ij}$ in Eq.(2.37) are random variables. As pointed out in [100], the choice of random variable representation is an important issue in MDO under uncertainty since it determines consistency through random linking variables. If response functions in children elements are nonlinear, the output distributions of responses can be non-normal, which might be considerably difficult to infer and match. Thus, in the previously published PATC formulations, the first few moments are used as targets and responses. Even with the first few moments, however, computing the solution is very expensive. Also, the consistency of PATC based on the first few moments matched has yet to be proven.

CHAPTER III

Sequential Linear Programming Coordination Strategy for Analytical Target Cascading

3.1 Introduction

In this chapter, we employ Sequential Linear Programming (SLP) as an alternative coordination strategy to solve ATC problems: the elements in the hierarchy are linearized and the linearized ATC is solved successively. The inspiration for the particular algorithm comes from recent SLP-filter implementations on Reliability Based Design Optimization (RBDO) problems [27, 28]. The SLP algorithm utilizes a filtering and trust region strategy to prove global convergence of RBDO problems for a single system. In addition to the SLP algorithm, a suspension strategy, similar to that in [8], is applied to avoid analyses of elements that do not need substantial redesign, for example, when a child element has a weaker coupling to its parent than those of the other children.

The chapter is organized as follows. In Section 3.2, SLP coordination strategy for ATC, or SLP-based ATC for short, is developed by formulating a Linear ATC (LATC) subproblem and modifying the notations used in the SLP-filter algorithm. Section 3.3 proposes the suspension strategy for SLP-based ATC and explains the algorithm flow. Illustrative test examples are presented in Section 3.4, followed by

conclusions in Section 3.5.

3.2 SLP-based Analytical Target Cascading

In SLP-based ATC, a nonlinear ATC problem is linearly approximated and solved using the "standard" ATC strategy to obtain the optimal solution of the LATC subproblem. By solving LATC subproblems successively, the algorithm converges to a solution of the original nonlinear problem with the aid of a filter algorithm and trust region method [57]. To maintain linearity, the LATC formulation requires different relaxation functions than those used in other ATC formulations [106, 126]. Decomposition and relaxation errors lead to a modification of the SLP-filter algorithms developed by Fletcher et al. [57]. The details of LATC formulation are explained in Section 3.2.1, and the convergence proof of ATC with L_∞ norms is presented in Section 3.2.2, while Section 3.2.3 discusses the notational modification of the SLP algorithm and flowcharts. Finally, Section 3.2.4 provides the convergence argument of SLP-based ATC.

3.2.1 LATC Subproblem Formulation

We consider the modified AIO system design problem, expressed in Eq.(3.1) from Section 2.4.

$$\begin{aligned} \min_{\bar{\mathbf{x}}_{11},\ldots,\bar{\mathbf{x}}_{NM}} \quad & \sum_{i=1}^{N}\sum_{j\in\mathcal{E}_i} f_{ij}(\bar{\mathbf{x}}_{ij}) \\ \text{subject to} \quad & \mathbf{g}_{ij}(\bar{\mathbf{x}}_{ij}) \le \mathbf{0}, \mathbf{h}_{ij}(\bar{\mathbf{x}}_{ij}) = \mathbf{0}, \\ & \mathbf{c}_{ij} = \mathbf{t}_{ij} - \mathbf{r}_{ij} = \mathbf{0}, \\ \text{where} \quad & \bar{\mathbf{x}}_{ij} = [\mathbf{x}_{ij}, \mathbf{t}_{(i+1)k}], \\ & \mathbf{r}_{ij} = \mathbf{a}_{ij}(\bar{\mathbf{x}}_{ij}) \quad \forall k \in \mathcal{C}_{ij}, \forall j \in \mathcal{E}_i, i = 1, ..., N. \end{aligned} \tag{3.1}$$

The derivation of Eq.(3.1) from the original nonlinear problem in Eq.(2.32) is discussed in Section 2.4. In Eq.(3.1), f_{ij}, $\mathbf{g}_{ij}$ and $\mathbf{h}_{ij}$ are the separated objective, inequality and equality constraints of element j at level i, respectively. Even though the convergence proof of the SLP algorithm in [57] is presented with only inequality constraints, the filter algorithm can be extended for problems with equality constraints using a constraint violation function similar to that defined in [60]. Note that the solution from Eq.(3.1) solves the original nonlinear problem Eq.(2.32).

For the SLP convergence argument presented in Section 3.2.4, a linear approximation is applied before decomposition. Note that applying the decomposition first will result in the same final LATC formulation. The LP problem of the modified AIO depends on the value of $\bar{\mathbf{x}}_{ij}^l$ $(\forall j \in \mathcal{E}_i, i = 1, ..., N)$ at an SLP iteration l and trust region radius ρ^l $(\rho^l > 0)$, and is given by:

$$
\begin{aligned}
\min_{\bar{\mathbf{d}}_{11}^l, ..., \bar{\mathbf{d}}_{NM}^l} \quad & \sum_{i=1}^{N} \sum_{j \in \mathcal{E}_i} \nabla f_{ij}^T(\bar{\mathbf{x}}_{ij}^l) \bar{\mathbf{d}}_{ij}^l \\
\text{subject to} \quad & \nabla \mathbf{g}_{ij}^T(\bar{\mathbf{x}}_{ij}^l) \bar{\mathbf{d}}_{ij}^l + \mathbf{g}_{ij}(\bar{\mathbf{x}}_{ij}^l) \leq \mathbf{0}, \\
& \nabla \mathbf{h}_{ij}^T(\bar{\mathbf{x}}_{ij}^l) \bar{\mathbf{d}}_{ij}^l + \mathbf{h}_{ij}(\bar{\mathbf{x}}_{ij}^l) = \mathbf{0}, \\
& \mathbf{t}_{ij}^l + \mathbf{d}_{\mathbf{t}_{ij}}^l - \mathbf{r}_{ij}(\bar{\mathbf{x}}_{ij}^l) - \nabla \mathbf{r}_{ij}^T(\bar{\mathbf{x}}_{ij}^l) \mathbf{d}_{ij}^l = \mathbf{0}, \\
& ||\bar{\mathbf{d}}_{ij}^l||_\infty \leq \rho^l, \\
\text{where} \quad & \bar{\mathbf{d}}_{ij}^l = [\mathbf{d}_{\mathbf{x}_{ij}}^l, \mathbf{d}_{\mathbf{t}_{(i+1)k}}^l], \quad \forall k \in \mathcal{C}_{ij} \\
& \mathbf{r}_{ij} = \mathbf{a}_{ij}(\mathbf{x}_{ij}), \quad \forall j \in \mathcal{E}_i, i = 1, ..., N.
\end{aligned}
\tag{3.2}
$$

In Eq.(3.2), the L_∞ norm is used to define the trust region because its implementation requires only simple bounds to the LAIO problem.

For decomposition, inconsistency among elements is allowed and the consistency constraints $\mathbf{c}_{ij}$ are relaxed. Because the relaxation functions in previous ATC literature, such as QP, OL, and AL, are nonlinear, a weighted L_∞ norm is applied in this

formulation to maintain the linearity of the elements:

$$||\mathbf{w}_{ij} \circ (\mathbf{t}_{ij} - \mathbf{r}_{ij})||_\infty \leq \epsilon_{ij} \Rightarrow \max|\mathbf{w}_{ij} \circ (\mathbf{t}_{ij} - \mathbf{r}_{ij})| \leq \epsilon_{ij} \tag{3.3}$$

where the $\circ$ operation indicates the component-wise multiplication of two vectors such that $\{a_1, ..., a_k\}^T \circ \{b_1, ..., b_k\}^T = \{a_1 b_1, ..., a_k b_k\}^T$. The outcome of $\mathbf{w}_{ij} \circ (\mathbf{t}_{ij} - \mathbf{r}_{ij})$ is a $1 \times m_{ij}$ vector, where m_{ij} is the number of components in $\mathbf{t}_{ij}$ or $\mathbf{r}_{ij}$. The right-hand-side equation is reformulated into a minimization problem with $2m_{ij}$ constraints:

$$\begin{aligned} &\min && \epsilon_{ij} \\ &\text{subject to} && -\boldsymbol{\epsilon}_{ij} \leq \mathbf{w}_{ij} \circ (\mathbf{t}_{ij} - \mathbf{r}_{ij}) \leq \boldsymbol{\epsilon}_{ij}, \end{aligned} \tag{3.4}$$

where $\boldsymbol{\epsilon}_{ij}$ is a $1 \times m_{ij}$ vector of ϵ_{ij}. By combining Eq.(4.5) with Eq.(3.2) as a relaxation term, the relaxed LAIO problem is given by:

$$\begin{aligned} \min \quad & \sum_{i=1}^{N} \sum_{j \in \mathcal{E}_i} \nabla f_{ij}(\bar{\mathbf{x}}_{ij}^l) \bar{\mathbf{d}}_{ij}^l + \sum_{i=1}^{N} \sum_{j \in \mathcal{E}_i} \epsilon_{ij}^l \\ \text{find} \quad & \bar{\mathbf{d}}_{11}^l, ..., \bar{\mathbf{d}}_{NM}^l, \epsilon_{22}^l, ..., \epsilon_{NM}^l \\ \text{subject to} \quad & \nabla \mathbf{g}_{ij}^T(\bar{\mathbf{x}}_{ij}^l) \bar{\mathbf{d}}_{ij}^l + \mathbf{g}_{ij}(\bar{\mathbf{x}}_{ij}^l) \leq \mathbf{0}, \\ & \nabla \mathbf{h}_{ij}^T(\bar{\mathbf{x}}_{ij}^l) \bar{\mathbf{d}}_{ij}^l + \mathbf{h}_{ij}(\bar{\mathbf{x}}_{ij}^l) = \mathbf{0}, \\ & -\boldsymbol{\epsilon}_{ij}^l \leq (\mathbf{w}_{ij} \circ (\mathbf{t}_{ij} + \mathbf{d}_{\mathbf{t}_{ij}} - \mathbf{r}_{ij} - \nabla \mathbf{r}_{ij}^T \bar{\mathbf{d}}_{ij}))^l \leq \boldsymbol{\epsilon}_{ij}^l, \\ & ||\bar{\mathbf{d}}_{ij}^l||_\infty \leq \rho^l, \\ \text{where} \quad & \bar{\mathbf{d}}_{ij}^l = [\mathbf{d}_{\mathbf{x}_{ij}}^l, \mathbf{d}_{\mathbf{t}_{(i+1)k}}^l], \quad \forall k \in \mathcal{C}_{ij} \\ & \forall j \in \mathcal{E}_i, i = 1, ..., N, \end{aligned} \tag{3.5}$$

Note that, unlike the other relaxation functions, most of the consistency constraints will remain inactive unless ϵ_{ij} becomes zero. Therefore, we cannot use monotonicity analysis [112] to incorporate the consistency constraints into the objective function.

As mentioned already, the convergence property of ATC has been proven based on the quadratic penalty function [106], the Ordinary Lagrangian relaxation [77] and the Augmented Lagrangian relaxation [94]. In the proofs, constraint sets are separable while the objective function is not, and the separable constraint sets is a crucial part of the proofs. On the other hand, the constraints in the formulation with L_∞ norms are separable instead of the objective function. Therefore, a new convergence proof for the use of L_∞ norms is provided in Section 3.2.2.

By decomposing the problem into separable elements, the LATC subproblem LP_{ij} of element j at level i is formulated as

$$\begin{aligned}
\min \quad & \nabla f_{ij}^T(\bar{\mathbf{x}}_{ij})\bar{\mathbf{d}}_{ij} + \epsilon_{ij} + \sum_{k\in\mathcal{C}_{ij}} \epsilon_{(i+1)k} \\
\text{find} \quad & \bar{\mathbf{d}}_{ij}, \epsilon_{ij}, \epsilon_{(i+1)1}, ..., \epsilon_{(i+1)n_{ij}} \\
\text{subject to} \quad & \nabla \mathbf{g}_{ij}^T(\bar{\mathbf{x}}_{ij})\bar{\mathbf{d}}_{ij} + \mathbf{g}_{ij}(\bar{\mathbf{x}}_{ij}) \le \mathbf{0}, \\
& \nabla \mathbf{h}_{ij}^T(\bar{\mathbf{x}}_{ij})\bar{\mathbf{d}}_{ij} + \mathbf{h}_{ij}(\bar{\mathbf{x}}_{ij}) = \mathbf{0}, \\
& -\boldsymbol{\epsilon}_{ij} \le (\mathbf{t}_{ij} + \mathbf{d}_{\mathbf{t}_{ij}} - \mathbf{r}_{ij} - \nabla \mathbf{r}_{ij}^T\bar{\mathbf{d}}_{ij}) \le \boldsymbol{\epsilon}_{ij}, \\
& -\boldsymbol{\epsilon}_{(i+1)k} \le \{\mathbf{w} \circ (\mathbf{t} + \mathbf{d}_{\mathbf{t}} - \mathbf{r} - \nabla \mathbf{r}^T\bar{\mathbf{d}})\}_{(i+1)k} \le \boldsymbol{\epsilon}_{(i+1)k}, \\
& ||\bar{\mathbf{d}}_{ij}||_\infty \le \rho, \\
\text{where} \quad & \bar{\mathbf{d}}_{ij} = [\mathbf{d}_{\mathbf{x}_{ij}}, \mathbf{d}_{\mathbf{t}_{(i+1)k}}], \quad \forall k \in \mathcal{C}_{ij},
\end{aligned} \tag{3.6}$$

where iteration index l is dropped for convenience. Information flows to and from a subproblem LP_{ij} are presented in Figure 3.1.

With a proper selection of weights in ATC, deviation errors become zero at convergence [106]. An important observation in Eq.(3.6) is that the global and local convergence properties depend on the size of trust regions and the scaling of design variables. In other words, the size of the $\bar{\mathbf{d}}_{ij}$ may be limited by the linking variables if the scaling of the design variables is not appropriate, which may cause the SLP

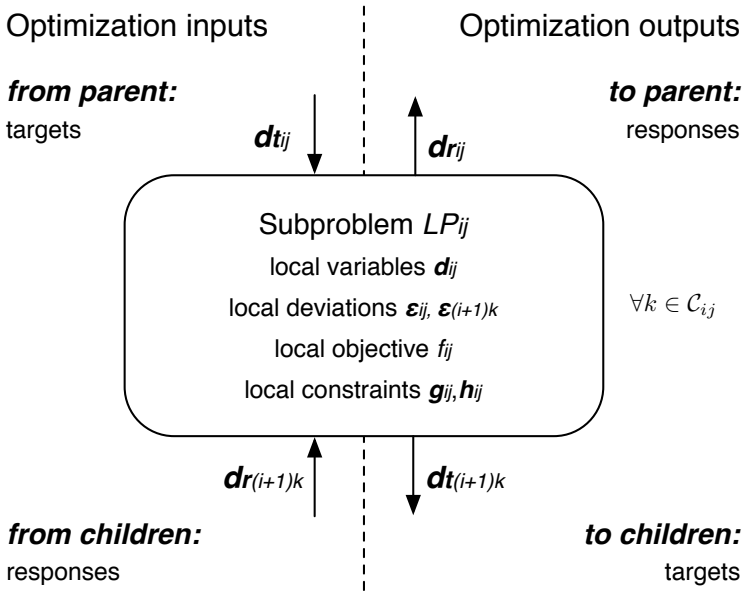

Figure 3.1: Information flow for ATC subproblem LP_{ij} of Eq.(3.6) (modified from [126])

algorithm to converge more slowly than an AIO formulation.

3.2.2 Convergence of ATC with L_∞ Norms

In order to prove the convergence of ATC with L_∞ norms, we follow the convergence arguments in [106] with respect to the Hierarchical Overlapping Coordination (HOC) strategy. To make the proof general, it will be proven for nonlinear problems instead of just linear ones.

Similarly to [106], consider a forest $\boldsymbol{F}$ that covers all nodes and edges from level $i = p$ to $r \geq p + 1$ as illustrated in Figure 3.2. Then, let q be a number between p and r and decompose the forest $\boldsymbol{F}$ in to two subforests $\boldsymbol{U}$ and $\boldsymbol{L}$, so that $\boldsymbol{U}$ and $\boldsymbol{L}$ contain all nodes and edges from level p to q and $q + 1$ to r, respectively. With this decomposition, we consider a multilevel problem in a bi-level structure. Assuming that the elements at level p are independent of each other, the elements in the forests

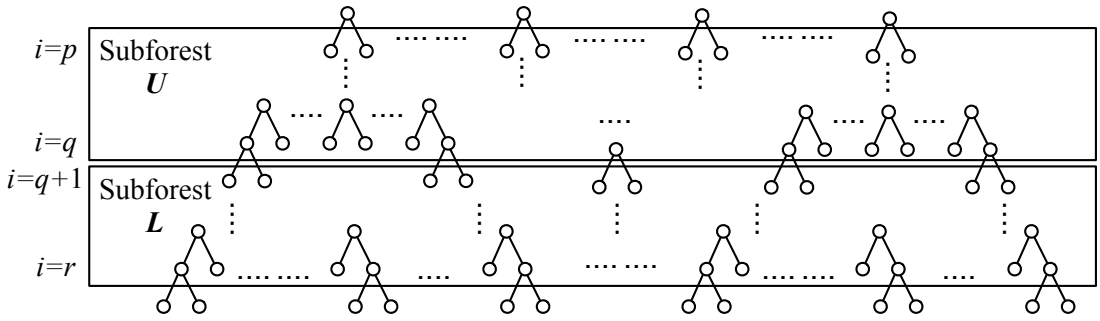

Figure 3.2: General forest in the problem hierarchy covering all nodes and edges from level $i = p$ to r (adapted from [106])

can be combined into a single problem and expressed as follows:

$$
\begin{aligned}
\text{Subforest } \boldsymbol{U}: \qquad & \min \quad \sum_{i=p-1}^{q} \sum_{j \in \mathcal{E}_i} f_{ij}(\bar{\mathbf{x}}_{ij}) + \sum_{i=p-1}^{q} \sum_{j \in \mathcal{E}_i} \sum_{k \in \mathcal{C}_{ij}} \boldsymbol{\epsilon}_{(i+1)k} \\
& \text{find} \quad \bar{\mathbf{x}}_{ij}, \boldsymbol{\epsilon}_{pk}, \boldsymbol{\epsilon}_{(i+1)k} \\
& \text{subject to} \quad \mathbf{g}_{ij}(\bar{\mathbf{x}}_{ij}) \leq \mathbf{0}, \quad \mathbf{h}_{ij}(\bar{\mathbf{x}}_{ij}) = \mathbf{0}, \\
& \qquad -\boldsymbol{\epsilon}_{pk} \leq \{\mathbf{w} \circ (\mathbf{t} - \mathbf{r})\}_{pk} \leq \boldsymbol{\epsilon}_{pk}, \\
& \qquad -\boldsymbol{\epsilon}_{(i+1)k} \leq \{\mathbf{w} \circ (\mathbf{t} - \mathbf{r})\}_{(i+1)k} \leq \boldsymbol{\epsilon}_{(i+1)k}, \\
& \text{where} \quad \bar{\mathbf{x}}_{ij} = [\mathbf{x}_{ij}, \mathbf{t}_{(i+1)k}], \quad \forall k \in \mathcal{C}_{ij}, \\
& \qquad \forall j \in \mathcal{E}_i, i = p, ...q;
\end{aligned}
\tag{3.7}
$$

$$
\begin{aligned}
\text{Subforest } \boldsymbol{L}: \qquad & \min \quad \sum_{i=q}^{r} \sum_{j \in \mathcal{E}_i} f_{ij}(\bar{\mathbf{x}}_{ij}) + \sum_{i=q}^{r} \sum_{j \in \mathcal{E}_i} \sum_{k \in \mathcal{C}_{ij}} \boldsymbol{\epsilon}_{(i+1)k} \\
& \text{find} \quad \bar{\mathbf{x}}_{ij}, \boldsymbol{\epsilon}_{(q+1)k}, \boldsymbol{\epsilon}_{(i+1)k} \\
& \text{subject to} \quad \mathbf{g}_{ij}(\bar{\mathbf{x}}_{ij}) \leq \mathbf{0}, \quad \mathbf{h}_{ij}(\bar{\mathbf{x}}_{ij}) = \mathbf{0}, \\
& \qquad -\boldsymbol{\epsilon}_{(q+1)k} \leq \{\mathbf{w} \circ (\mathbf{t} - \mathbf{r})\}_{(q+1)k} \leq \boldsymbol{\epsilon}_{(q+1)k}, \\
& \qquad -\boldsymbol{\epsilon}_{(i+1)k} \leq \{\mathbf{w} \circ (\mathbf{t} - \mathbf{r})\}_{(i+1)k} \leq \boldsymbol{\epsilon}_{(i+1)k}, \\
& \text{where} \quad \bar{\mathbf{x}}_{ij} = [\mathbf{x}_{ij}, \mathbf{t}_{(i+1)k}], \quad \forall k \in \mathcal{C}_{ij}, \\
& \qquad \forall j \in \mathcal{E}_i, i = q+1, ...r.
\end{aligned}
\tag{3.8}
$$

$$
\begin{aligned}
\text{Forest } \boldsymbol{F}: \qquad & \min \quad \sum_{i=p-1}^{r} \sum_{j \in \mathcal{E}_i} f_{ij}(\bar{\mathbf{x}}_{ij}) + \sum_{i=p-1}^{r} \sum_{j \in \mathcal{E}_i} \sum_{k \in \mathcal{C}_{ij}} \boldsymbol{\epsilon}_{(i+1)k} \\
& \text{find} \quad \bar{\mathbf{x}}_{ij}, \boldsymbol{\epsilon}_{pk}, \boldsymbol{\epsilon}_{(i+1)k} \\
& \text{subject to} \quad \mathbf{g}_{ij}(\bar{\mathbf{x}}_{ij}) \leq \mathbf{0}, \quad \mathbf{h}_{ij}(\bar{\mathbf{x}}_{ij}) = \mathbf{0}, \\
& \qquad -\boldsymbol{\epsilon}_{pk} \leq \{\mathbf{w} \circ (\mathbf{t} - \mathbf{r})\}_{pk} \leq \boldsymbol{\epsilon}_{pk}, \\
& \qquad -\boldsymbol{\epsilon}_{(i+1)k} \leq \{\mathbf{w} \circ (\mathbf{t} - \mathbf{r})\}_{(i+1)k} \leq \boldsymbol{\epsilon}_{(i+1)k}, \\
& \text{where} \quad \bar{\mathbf{x}}_{ij} = [\mathbf{x}_{ij}, \mathbf{t}_{(i+1)k}], \quad \forall k \in \mathcal{C}_{ij}, \\
& \qquad \forall j \in \mathcal{E}_i, i = p, ...r;
\end{aligned}
\tag{3.9}
$$

In Eq.(3.7), (3.8) and (3.9), the consistency constraints can be rewritten in the negative null form:

$$
\begin{pmatrix}
\mathbf{w}_U \circ (\mathbf{t}_U - \mathbf{r}_U) - \boldsymbol{\epsilon}_U, & \mathbf{w}_U \circ (\mathbf{r}_U - \mathbf{t}_U) - \boldsymbol{\epsilon}_U \\
\mathbf{w}_L \circ (\mathbf{t}_L - \mathbf{r}_L) - \boldsymbol{\epsilon}_L, & \mathbf{w}_L \circ (\mathbf{r}_L - \mathbf{t}_L) - \boldsymbol{\epsilon}_L
\end{pmatrix} \leq \mathbf{0} \ . \tag{3.10}
$$

where $\mathbf{t}_U$, $\mathbf{r}_U$ and $\boldsymbol{\epsilon}_U$ are the vectors of targets, responses and consistency errors in the upper forest, respectively, while $\mathbf{t}_L$, $\mathbf{r}_L$ and $\boldsymbol{\epsilon}_L$ are the vectors of targets, responses and consistency errors in the lower forest, respectively. Comparing Eq.(3.10) with consistency constraints in Eq.(3.9), one can easily find the consistency constraints between level q and $q+1$ are included twice in Eq.(3.10). The values for $\boldsymbol{\epsilon}_{(q+1)k}$, however, can be different depending on which subforests the values are obtained from. Therefore, let $\boldsymbol{\epsilon}^U_{(q+1)k}$ and $\boldsymbol{\epsilon}^L_{(q+1)k}$ be the consistency errors at level $q+1$ obtained from the upper and lower subforests, respectively. By adding copies of consistency constraints at level $q+1$ with $\boldsymbol{\epsilon}^U_{(q+1)k}$ and $\boldsymbol{\epsilon}^L_{(q+1)k}$, we can reformulate

Eq.(3.7), (3.8) and (3.9), and express them as follows:

$$
\begin{aligned}
\text{Subforest } \boldsymbol{U}: \min \quad & \sum_{i=p}^{q}\sum_{j\in\mathcal{E}_i} f_{ij}(\bar{\mathbf{x}}_{ij}) + \sum_{i=p}^{q}\sum_{j\in\mathcal{E}_i} \boldsymbol{\epsilon}_{ij} + \sum_{j\in\mathcal{E}_{q+1}} \boldsymbol{\epsilon}^{U}_{(q+1)k} \\
\text{find} \quad & \bar{\mathbf{x}}_{ij}, \boldsymbol{\epsilon}_{ij}, \{\boldsymbol{\epsilon}^{U}_{(q+1)j} | j \in \mathcal{E}_{q+1}\} \\
\text{subject to} \quad & \mathbf{g}_{ij}(\bar{\mathbf{x}}_{ij}) \le \mathbf{0}, \quad \mathbf{h}_{ij}(\bar{\mathbf{x}}_{ij}) = \mathbf{0}, \\
& \left\{ \left(\begin{array}{l} (\mathbf{w}\circ(\mathbf{t}-\mathbf{r}) - \boldsymbol{\epsilon})_{ij} \le \mathbf{0} \\ (\mathbf{w}\circ(\mathbf{r}-\mathbf{t}) - \boldsymbol{\epsilon})_{ij} \le \mathbf{0} \end{array} \right) \middle| \begin{array}{l} j \in \mathcal{E}_i, \\ i = p, ..., q \end{array} \right\} \\
& \left\{ \left(\begin{array}{l} (\mathbf{w}\circ(\mathbf{t}-\mathbf{r}) - \boldsymbol{\epsilon}^{U})_{(q+1)j} \le \mathbf{0} \\ (\mathbf{w}\circ(\mathbf{r}-\mathbf{t}) - \boldsymbol{\epsilon}^{U})_{(q+1)j} \le \mathbf{0} \end{array} \right) \middle| j \in \mathcal{E}_{q+1} \right\} \\
\text{where} \quad & \bar{\mathbf{x}}_{ij} = [\mathbf{x}_{ij}, \mathbf{t}_{(i+1)k}], \quad \forall k \in \mathcal{C}_{ij}, \\
& \forall j \in \mathcal{E}_i, i = p, ..., q;
\end{aligned}
\tag{3.11}
$$

$$
\begin{aligned}
\text{Subforest } \boldsymbol{L}: \min \quad & \sum_{i=q+1}^{r}\sum_{j\in\mathcal{E}_i} f_{ij}(\bar{\mathbf{x}}_{ij}) + \sum_{i=q+2}^{r+1}\sum_{j\in\mathcal{E}_i} \boldsymbol{\epsilon}_{ij} + \sum_{j\in\mathcal{E}_{q+1}} \boldsymbol{\epsilon}^{L}_{(q+1)j} \\
\text{find} \quad & \bar{\mathbf{x}}_{ij}, \boldsymbol{\epsilon}_{ij}, \{\boldsymbol{\epsilon}^{L}_{(q+1)j} | j \in \mathcal{E}_{q+1}\} \\
\text{subject to} \quad & \mathbf{g}_{ij}(\bar{\mathbf{x}}_{ij}) \le \mathbf{0}, \quad \mathbf{h}_{ij}(\bar{\mathbf{x}}_{ij}) = \mathbf{0}, \\
& \left\{ \left(\begin{array}{l} (\mathbf{w}\circ(\mathbf{t}-\mathbf{r}) - \boldsymbol{\epsilon})_{(i+1)k} \le \mathbf{0} \\ (\mathbf{w}\circ(\mathbf{r}-\mathbf{t}) - \boldsymbol{\epsilon})_{(i+1)k} \le \mathbf{0} \end{array} \right) \middle| \begin{array}{l} k \in \mathcal{C}_{ij}, j \in \mathcal{E}_i, \\ i = q+1, ..., r \end{array} \right\} \\
& \left\{ \left(\begin{array}{l} (\mathbf{w}\circ(\mathbf{t}-\mathbf{r}) - \boldsymbol{\epsilon}^{U})_{(q+1)j} \le \mathbf{0} \\ (\mathbf{w}\circ(\mathbf{r}-\mathbf{t}) - \boldsymbol{\epsilon}^{U})_{(q+1)j} \le \mathbf{0} \end{array} \right) \middle| j \in \mathcal{E}_{q+1} \right\} \\
\text{where} \quad & \bar{\mathbf{x}}_{ij} = [\mathbf{x}_{ij}, \mathbf{t}_{(i+1)k}], \quad \forall k \in \mathcal{C}_{ij}, \\
& \forall j \in \mathcal{E}_i, i = q+1, ..., r.
\end{aligned}
\tag{3.12}
$$

$$
\begin{aligned}
\text{Forest } \boldsymbol{F}: \min \quad & \sum_{i=p}^{r}\left(\sum_{j\in\mathcal{E}_i} f_{ij}(\bar{\mathbf{x}}_{ij})\right) + \sum_{i=p,i\neq q+1}^{r+1}\left(\sum_{j\in\mathcal{E}_i}\boldsymbol{\epsilon}_{ij}\right) \\
& + \sum_{j\in\mathcal{E}_{q+1}} (\boldsymbol{\epsilon}^U_{(q+1)j} + \boldsymbol{\epsilon}^L_{(q+1)j}) \\
\text{find} \quad & \bar{\mathbf{x}}_{ij}, \{\boldsymbol{\epsilon}_{ij} | j\in\mathcal{E}_i, i=p,...,r, i\neq q+1\}, \\
& \{\boldsymbol{\epsilon}^U_{(q+1)j} | j\in\mathcal{E}_{q+1}\}, \{\boldsymbol{\epsilon}^L_{(q+1)j} | j\in\mathcal{E}_{q+1}\} \\
\text{subject to} \quad & \mathbf{g}_{ij}(\bar{\mathbf{x}}_{ij}) \leq \mathbf{0}, \quad \mathbf{h}_{ij}(\bar{\mathbf{x}}_{ij}) = \mathbf{0}, \\
& \left\{ \left(\begin{array}{l} (\mathbf{w}\circ(\mathbf{t}-\mathbf{r}) - \boldsymbol{\epsilon})_{ij} \leq \mathbf{0} \\ (\mathbf{w}\circ(\mathbf{r}-\mathbf{t}) - \boldsymbol{\epsilon})_{ij} \leq \mathbf{0} \end{array} \right) \middle| \begin{array}{l} j\in\mathcal{E}_i, i=p,...,r+1, \\ i\neq q+1 \end{array} \right\} \\
& \left\{ \left(\begin{array}{l} (\mathbf{w}\circ(\mathbf{t}-\mathbf{r}) - \boldsymbol{\epsilon}^U)_{(q+1)j} \leq \mathbf{0} \\ (\mathbf{w}\circ(\mathbf{r}-\mathbf{t}) - \boldsymbol{\epsilon}^U)_{(q+1)j} \leq \mathbf{0} \\ (\mathbf{w}\circ(\mathbf{t}-\mathbf{r}) - \boldsymbol{\epsilon}^L)_{(q+1)j} \leq \mathbf{0} \\ (\mathbf{w}\circ(\mathbf{r}-\mathbf{t}) - \boldsymbol{\epsilon}^L)_{(q+1)j} \leq \mathbf{0} \end{array} \right) \middle| j\in\mathcal{E}_{q+1} \right\} \\
\text{where} \quad & \bar{\mathbf{x}}_{ij} = [\mathbf{x}_{ij}, \mathbf{t}_{(i+1)k}], \quad \forall k\in\mathcal{C}_{ij}, \\
& \forall j\in\mathcal{E}_i, i=p,...,r;
\end{aligned}
\tag{3.13}
$$

In Eq.(3.11), (3.12) and (3.13), $\mathbf{g}_{ij}$, $\mathbf{h}_{ij}$ and the first sets of the consistency constraints are separable functions according to the lemma in Section IV in [106]. Therefore, we define the augmented inequality constraints of the upper and lower subforest, $\mathbf{g}_U$ and $\mathbf{g}_L$, and the remaining consistency constraints of the upper and lower subforest, $\bar{\mathbf{c}}_U$ and $\bar{\mathbf{c}}_L$, as follows:

$$
\mathbf{g}_U := \left\{ \left(\begin{array}{c} \mathbf{g}_{ij} \\ (\mathbf{w}\circ(\mathbf{t}-\mathbf{r}) - \boldsymbol{\epsilon})_{ij} \leq \mathbf{0} \\ (\mathbf{w}\circ(\mathbf{r}-\mathbf{t}) - \boldsymbol{\epsilon})_{ij} \leq \mathbf{0} \end{array} \right) \middle| \begin{array}{l} j\in\mathcal{E}_i, \\ i=p,...,q \end{array} \right\} \tag{3.14}
$$

$$\mathbf{g}_L := \left\{ \left(\begin{array}{c} \mathbf{g}_{ij} \\ (\mathbf{w} \circ (\mathbf{t} - \mathbf{r}) - \boldsymbol{\epsilon})_{(i+1)k} \leq \mathbf{0} \\ (\mathbf{w} \circ (\mathbf{r} - \mathbf{t}) - \boldsymbol{\epsilon})_{(i+1)k} \leq \mathbf{0} \end{array} \right) \middle| \begin{array}{l} k \in \mathcal{C}_{ij}, j \in \mathcal{E}_i, \\ i = q+1, ..., r \end{array} \right\} \tag{3.15}$$

$$\bar{\mathbf{c}}_U := \left\{ \left(\begin{array}{l} (\mathbf{w} \circ (\mathbf{t} - \mathbf{r}) - \boldsymbol{\epsilon}^U)_{(q+1)j} \leq \mathbf{0} \\ (\mathbf{w} \circ (\mathbf{r} - \mathbf{t}) - \boldsymbol{\epsilon}^U)_{(q+1)j} \leq \mathbf{0} \end{array} \right) \middle| j \in \mathcal{E}_{q+1} \right\} \tag{3.16}$$

$$\bar{\mathbf{c}}_L := \left\{ \left(\begin{array}{l} (\mathbf{w} \circ (\mathbf{t} - \mathbf{r}) - \boldsymbol{\epsilon}^L)_{(q+1)j} \leq \mathbf{0} \\ (\mathbf{w} \circ (\mathbf{r} - \mathbf{t}) - \boldsymbol{\epsilon}^L)_{(q+1)j} \leq \mathbf{0} \end{array} \right) \middle| j \in \mathcal{E}_{q+1} \right\} \tag{3.17}$$

Further, $\mathbf{h}_U$ and $\mathbf{h}_L$ can be defined as follows:

$$\begin{aligned} \mathbf{h}_U &= \{\mathbf{h}_{ij} | j \in \mathcal{E}_i, i = p, ..., q\} \\ \mathbf{h}_L &= \{\mathbf{h}_{ij} | j \in \mathcal{E}_i, i = q+1, ..., r\}. \end{aligned} \tag{3.18}$$

Then the equation for the forest $\boldsymbol{F}$ in Eq.(3.9) can be rewritten in the following simplified form:

$$\begin{aligned} \min_{\mathbf{x}} \quad & \tilde{f}(\mathbf{x}) \\ \text{subject to} \quad & \mathbf{g}(\bar{\mathbf{x}}) = \left(\begin{array}{c} \mathbf{g}_U \\ \mathbf{g}_L \end{array} \right) \leq 0, \quad \mathbf{h}(\bar{\mathbf{x}}) = \left(\begin{array}{c} \mathbf{h}_U \\ \mathbf{h}_L \end{array} \right) = 0, \\ & \bar{\mathbf{c}}(\mathbf{x}) = \left(\begin{array}{c} \bar{\mathbf{c}}_U \\ \bar{\mathbf{c}}_L \end{array} \right) \leq 0 \end{aligned} \tag{3.19}$$

where $\bar{\mathbf{x}} \in \mathbb{R}^n$ includes all variables in Eq.(3.9) except for $\boldsymbol{\epsilon}^U_{(q+1)j}$ and $\boldsymbol{\epsilon}^L_{(q+1)j}$ while $\mathbf{x} \in \mathbb{R}^{n+n^{\boldsymbol{\epsilon}}}$ is the vector of all variables in Eq.(3.9) including $\boldsymbol{\epsilon}^U_{(q+1)j}$ and $\boldsymbol{\epsilon}^L_{(q+1)j}$. Let $\mathbf{x_U} \in \mathbb{R}^{n_U + n^{\boldsymbol{\epsilon}}_U}$ be the vector of all variables in the upper subforest problem and $\mathbf{x_L} \in \mathbb{R}^{n_L + n^{\boldsymbol{\epsilon}}_L}$ be the vector of all variables in the upper subforest problem, where $n = n_U + n_L$ and $n^{\boldsymbol{\epsilon}} = n^{\boldsymbol{\epsilon}}_U + n^{\boldsymbol{\epsilon}}_L$. Then we can rearrange the variables in Eq.(3.13) in

the following way:

$$\mathbf{x}_U = \begin{pmatrix} \bar{\mathbf{x}}_U \\ \\ \boldsymbol{\epsilon}_U \end{pmatrix}, \quad \mathbf{x}_L = \begin{pmatrix} \bar{\mathbf{x}}_L \\ \\ \boldsymbol{\epsilon}_L \end{pmatrix}, \quad \mathbf{x} = \begin{pmatrix} \mathbf{x}_U \\ \\ \mathbf{x}_L \end{pmatrix} \tag{3.20}$$

where $\mathbf{x}_U$ and $\mathbf{x}_L$ consist of variables at level p to q and $q+1$ to r, respectively. In Eq.(3.20), $\boldsymbol{\epsilon}_U$ and $\boldsymbol{\epsilon}_U$ are the vectors of $\boldsymbol{\epsilon}^U_{(q+1)j}$ and $\boldsymbol{\epsilon}^L_{(q+1)j}$, respectively, where $j \in \mathcal{E}_{q+1}$, while the rest of $\boldsymbol{\epsilon}$ are included in $\bar{\mathbf{x}}_U$ and $\bar{\mathbf{x}}_L$, respectively. Additionally, we define a vector $\bar{\mathbf{x}}$ and $\bar{\boldsymbol{\epsilon}}$, expressed as

$$\bar{\mathbf{x}} = \begin{pmatrix} \bar{\mathbf{x}}_U \\ \\ \bar{\mathbf{x}}_L \end{pmatrix}, \bar{\boldsymbol{\epsilon}} = \begin{pmatrix} \bar{\boldsymbol{\epsilon}}_U \\ \\ \bar{\boldsymbol{\epsilon}}_L \end{pmatrix}. \tag{3.21}$$

Define H_U to be the submatrix of the identity matrix I_n consisting of its first n_U rows, and H_L to be the submatrix of I_n consisting of its last n_L rows. Then we can define the following relation:

$$I_n = \begin{pmatrix} H_U \\ \\ H_L \end{pmatrix}, \quad H_U\bar{\mathbf{x}} = \bar{\mathbf{x}}_U, \quad H_L\bar{\mathbf{x}} = \bar{\mathbf{x}}_L. \tag{3.22}$$

In the HOC strategy, elements in two adjoint sets of levels are solved iteratively. Therefore, the corresponding elements can be defined as two subforests $\boldsymbol{U}$ and $\boldsymbol{L}$ that form a forest $\boldsymbol{F}$. By letting the solutions obtained from the upper and lower subforests be $\mathbf{d}_U$ and $\mathbf{d}_L$, the iterative process of HOC can be described in terms of H_U and H_L, expressed as:

$$\begin{aligned} &\text{Subforest } \boldsymbol{U}: \qquad \min_{\mathbf{x}} \quad \tilde{f}(\mathbf{x}) \\ &\qquad\qquad \text{subject to} \qquad \mathbf{g}(\bar{\mathbf{x}}) \le 0, \quad \mathbf{h}(\bar{\mathbf{x}}) = 0, \quad \bar{\mathbf{c}}(\mathbf{x}) \le 0, \quad H_L\bar{\mathbf{x}} = \mathbf{d}_L, \end{aligned} \tag{3.23}$$

where $\mathbf{d}_L$ is fixed and feasible values of the variables in the lower subforests except for $\boldsymbol{\epsilon}^U_{(q+1)j}$ where $j \in \mathcal{E}_{q+1}$, and

$$\begin{aligned} &\text{Subforest } \boldsymbol{L}: \qquad \min_{\mathbf{x}} \quad \tilde{f}(\mathbf{x}) \\ &\qquad\qquad \text{subject to} \qquad \mathbf{g}(\bar{\mathbf{x}}) \le 0, \quad \mathbf{h}(\bar{\mathbf{x}}) = 0, \quad \bar{\mathbf{c}}(\mathbf{x}) \le 0, \quad H_U\bar{\mathbf{x}} = \mathbf{d}_U, \end{aligned} \tag{3.24}$$

where $\mathbf{d}_U$ is fixed and feasible values of the variables in the upper subforests except for $\boldsymbol{\epsilon}^U_{(q+1)j}$ where $j \in \mathcal{E}_{q+1}$. As stated earlier, $\mathbf{d}_U$ ($\mathbf{d}_L$, respectively) is updated during the iterative ATC process by solving Eq.(3.23) (Eq. (3.24), repectively).

We are now ready to complete the convergence proof for ATC with L_∞ norms. According to the Karush-Kuhn-Tucker (KKT) condition, a regular point $\mathbf{x}^*$ is a solution to Eq.(3.19) if and only if there exist a nonnegative vector $\boldsymbol{\mu}_\mathbf{g}$ and $\boldsymbol{\mu}_\mathbf{c}$ and a vector $\boldsymbol{\lambda}$ such that

$$-\nabla \tilde{f}(\mathbf{x}^*) = \boldsymbol{\mu}_\mathbf{g}^T \nabla \mathbf{g}_A(\bar{\mathbf{x}}^*) + \boldsymbol{\lambda}^T \nabla \mathbf{h}(\bar{\mathbf{x}}^*) + \boldsymbol{\mu}_{\bar{\mathbf{c}}}^T \nabla \bar{\mathbf{c}}_A(\mathbf{x}^*) \tag{3.25}$$

where $\nabla \mathbf{g}_A$ and $\nabla \bar{\mathbf{c}}_A$ are the submatrix of $\nabla \mathbf{g}$ and $\nabla \bar{\mathbf{c}}$ consisting of the active inequality constraints at $\mathbf{x}^*$. If a feasible solution to Eq.(3.19), $\mathbf{x}^*$, exists, by solving Eq.(3.23) and (3.24) iteratively, $\mathbf{x}_U$ and $\mathbf{x}_L$ converge to $\mathbf{x}^*$ [106]. That is, $\mathbf{x}^*$ is a solution of both Eq.(3.23) and (3.24). Therefore, there exist vectors $\boldsymbol{z}_\mathbf{g} \geq 0$, $\boldsymbol{z}_{\bar{\mathbf{c}}} \geq 0$, $\boldsymbol{z}_\mathbf{h}$ and $\boldsymbol{u}$, and vectors $\boldsymbol{w}_\mathbf{g} \geq 0$, $\boldsymbol{w}_{\bar{\mathbf{c}}} \geq 0$, $\boldsymbol{w}_\mathbf{h}$ and $\boldsymbol{v}$, such that the following two equations simultaneously hold:

$$\begin{aligned} -\nabla \tilde{f}(\mathbf{x}^*) &= \boldsymbol{z}_\mathbf{g}^T \nabla \mathbf{g}_A(\bar{\mathbf{x}}^*) + \boldsymbol{z}_\mathbf{h}^T \nabla \mathbf{h}(\bar{\mathbf{x}}^*) + \boldsymbol{z}_{\bar{\mathbf{c}}}^T \nabla \bar{\mathbf{c}}_A(\mathbf{x}^*) + \boldsymbol{u}^T \nabla (H_U \bar{\mathbf{x}}^*) \\ -\nabla \tilde{f}(\mathbf{x}^*) &= \boldsymbol{w}_\mathbf{g}^T \nabla \mathbf{g}_A(\bar{\mathbf{x}}^*) + \boldsymbol{w}_\mathbf{g}^T \nabla \mathbf{h}(\bar{\mathbf{x}}^*) + \boldsymbol{w}_{\bar{\mathbf{c}}}^T \nabla \bar{\mathbf{c}}_A(\mathbf{x}^*) + \boldsymbol{v}^T \nabla (H_L \bar{\mathbf{x}}^*) \end{aligned} \tag{3.26}$$

Therefore, the convergence proof of ATC with L_∞ norms only requires to prove that a solution to both Eq.(3.23) and (3.24) also solves Eq.(3.19).

Lemma 3.2.1. *If $\mathbf{x}^*$ is a solution to both Eq.(3.25) and (3.26), then $\boldsymbol{\mu}_{\bar{c}} = \boldsymbol{z}_{\bar{c}} = \boldsymbol{w}_{\bar{c}}$.*

Proof: Since $\bar{\mathbf{c}}_U$ and $\bar{\mathbf{c}}_L$ are the sets of consistency constraints for linking variables between the elements at level q and $q+1$, they are identical except for the superscripts of $\boldsymbol{\epsilon}$ if we arrange them in the same order. Therefore, the sets of active constraints

at $\mathbf{x}^*$ are also identical except for the superscripts of $\boldsymbol{\epsilon}$. Then if we consider the rows in Eq.(3.25) and (3.26) that correspond to $\bar{\boldsymbol{\epsilon}}$, they can be rewritten as

$$\begin{aligned} -\nabla_{\bar{\boldsymbol{\epsilon}}}\tilde{f}(\mathbf{x}^*) &= \boldsymbol{\mu}_{\mathbf{c}}^T \nabla_{\bar{\boldsymbol{\epsilon}}}\mathbf{c}_A(\mathbf{x}^*) \\ &= \boldsymbol{z}_{\bar{\mathbf{c}}}^T \nabla_{\bar{\boldsymbol{\epsilon}}}\bar{\mathbf{c}}_A(\mathbf{x}^*) \\ &= \boldsymbol{w}_{\bar{\mathbf{c}}}^T \nabla_{\bar{\boldsymbol{\epsilon}}}\bar{\mathbf{c}}_A(\mathbf{x}^*) \end{aligned} \tag{3.27}$$

because $\nabla_{\bar{\boldsymbol{\epsilon}}}\mathbf{g}(\bar{\mathbf{x}}) = \mathbf{0}$, $\nabla_{\bar{\boldsymbol{\epsilon}}}\mathbf{h}(\bar{\mathbf{x}}) = \mathbf{0}$, $\nabla_{\bar{\boldsymbol{\epsilon}}}(H_U\bar{\mathbf{x}}) = \mathbf{0}$ and $\nabla_{\bar{\boldsymbol{\epsilon}}}(H_L\bar{\mathbf{x}}) = \mathbf{0}$. Thus, $\boldsymbol{\mu}_{\bar{c}} = \boldsymbol{z}_{\bar{c}} = \boldsymbol{w}_{\bar{c}}$. $\triangleleft$

Theorem 3.2.2. *If $\mathbf{x}^*$ is a solution of both Eq.(3.23) and (3.24), then it also solves Eq.(3.19).*

Proof: Let $\mathbf{x}^*$ be a solution to both Eq.(3.23) and (3.24). Then, there exist vectors

$$\boldsymbol{z}_{\mathbf{g}} = \begin{pmatrix} z_{\mathbf{g}}^1 \\ \vdots \\ z_{\mathbf{g}}^{p_g^A} \end{pmatrix} \geq \mathbf{0} \quad \boldsymbol{z}_{\mathbf{h}} = \begin{pmatrix} z_{\mathbf{h}}^1 \\ \vdots \\ z_{\mathbf{h}}^{p_h} \end{pmatrix} \quad \boldsymbol{u} = \begin{pmatrix} u^1 \\ \vdots \\ u^{n_U} \end{pmatrix} \tag{3.28}$$

where p_g^A and p_h are the number of active inequality and equality constraints at $\mathbf{x}^*$, respectively. Similarly,

$$\boldsymbol{w}_{\mathbf{g}} = \begin{pmatrix} w_{\mathbf{g}}^1 \\ \vdots \\ w_{\mathbf{g}}^{p_g^A} \end{pmatrix} \geq \mathbf{0} \quad \boldsymbol{w}_{\mathbf{h}} = \begin{pmatrix} w_{\mathbf{h}}^1 \\ \vdots \\ w_{\mathbf{h}}^{p_h} \end{pmatrix} \quad \boldsymbol{v} = \begin{pmatrix} v^1 \\ \vdots \\ v^{n_L}. \end{pmatrix} \tag{3.29}$$

Also, by Lemma 3.2.1, we can define $\boldsymbol{z}_{\bar{\mathbf{c}}} = \boldsymbol{w}_{\bar{\mathbf{c}}} \geq \mathbf{0}$. Let integer $p_g^{A,U}$ ($p_g^{A,L}$, respectively) be the number of active inequality constraints involving variables $\bar{\mathbf{x}}_U$ ($\bar{\mathbf{x}}_L$, respectively) only. Similarly, let integer p_h^U (p_h^L, respectively) be the number of equality constraints involving variables $\bar{\mathbf{x}}_U$ ($\bar{\mathbf{x}}_L$, respectively) only. By the separability of $\mathbf{g}$ and $\mathbf{h}$ defined in [106], $p_g^A = p_g^{A,U} + p_g^{A,L}$ and $p_h = p_h^U + p_h^L$. Define

nonnegative vectors $\boldsymbol{\mu}_{\mathbf{g}}$ and $\boldsymbol{\mu}_{\bar{\mathbf{c}}}$, and a vector $\boldsymbol{\lambda}$ as follows:

$$\boldsymbol{\mu}_{\mathbf{g}} = \begin{pmatrix} w_{\mathbf{g}}^{1} \\ \vdots \\ w_{\mathbf{g}}^{p_g^{A,U}} \\ z_{\mathbf{g}}^{p_g^{A,U+1}} \\ \vdots \\ z_{\mathbf{g}}^{p_g^{A}} \end{pmatrix}, \quad \boldsymbol{\mu}_c = \boldsymbol{z}_c = \boldsymbol{w}_c, \quad \boldsymbol{\lambda} = \begin{pmatrix} w_{\mathbf{h}}^{1} \\ \vdots \\ w_{\mathbf{h}}^{p_h^{U}} \\ z_{\mathbf{h}}^{p_h^{U+1}} \\ \vdots \\ w_{\mathbf{h}}^{p_h} \end{pmatrix} \tag{3.30}$$

We claim that these $\boldsymbol{\mu}_{\mathbf{g}}$, $\boldsymbol{\mu}_{\bar{\mathbf{c}}}$ and $\boldsymbol{\lambda}$ satisfy Eq.(3.25), which implies that $\mathbf{x}^*$ is a solution to Eq.(3.9). To verify the claim, define the matrices $A_{\mathbf{g}}^U$, $A_{\mathbf{g}}^L$, $A_{\mathbf{h}}^U$ and $A_{\mathbf{h}}^L$, as follows:

$$\nabla_{\bar{\mathbf{x}}}\mathbf{g}_A(\bar{\mathbf{x}}^*) = (A_{\mathbf{g}}^U, A_{\mathbf{g}}^L), \quad \nabla_{\bar{\mathbf{x}}}\mathbf{h}(\bar{\mathbf{x}}^*) = (A_{\mathbf{h}}^U, A_{\mathbf{h}}^L) \tag{3.31}$$

where $A_{\mathbf{g}}^U$ and $A_{\mathbf{h}}^U$ are the first n_U columns of the matrices $\nabla_{\bar{\mathbf{x}}}\mathbf{g}_A(\bar{\mathbf{x}}^*)$ and $\nabla_{\bar{\mathbf{x}}}\mathbf{h}(\bar{\mathbf{x}}^*)$, respectively.

Eq.(3.25) can be divided into two equations involving $\bar{\mathbf{x}}$ and $\bar{\mathbf{u}}$, expressed as:

$$-\nabla_{\bar{\mathbf{x}}}\tilde{f}(\mathbf{x}^*) = \boldsymbol{\mu}_{\mathbf{g}}^T\nabla_{\bar{\mathbf{x}}}\mathbf{g}_A(\bar{\mathbf{x}}^*) + \boldsymbol{\lambda}^T\nabla_{\bar{\mathbf{x}}}\mathbf{h}(\bar{\mathbf{x}}^*) + \boldsymbol{\mu}_{\bar{\mathbf{c}}}^T\nabla_{\bar{\mathbf{x}}}\bar{\mathbf{c}}_A(\mathbf{x}^*) \tag{3.32}$$

$$-\nabla_{\bar{\boldsymbol{\epsilon}}}\tilde{f}(\mathbf{x}^*) = \boldsymbol{\mu}_{\mathbf{g}}^T\nabla_{\bar{\boldsymbol{\epsilon}}}\mathbf{g}_A(\bar{\mathbf{x}}^*) + \boldsymbol{\lambda}^T\nabla_{\bar{\boldsymbol{\epsilon}}}\mathbf{h}(\bar{\mathbf{x}}^*) + \boldsymbol{\mu}_{\bar{\mathbf{c}}}^T\nabla_{\bar{\boldsymbol{\epsilon}}}\bar{\mathbf{c}}_A(\mathbf{x}^*). \tag{3.33}$$

Since Eq.(3.33) is satisfied by Lemma 3.2.1, we only need to prove that Eq.(3.32) is satisfied. Thus, considering Eq.(3.26) that involves $\bar{\mathbf{x}}$, it can be rewritten as

$$-\nabla_{\bar{\mathbf{x}}}\tilde{f}^T(\mathbf{x}^*) = \begin{pmatrix} A_{\mathbf{g}}^{U^T} \\ A_{\mathbf{g}}^{L^T} \end{pmatrix} \boldsymbol{z}_{\mathbf{g}} + \begin{pmatrix} A_{\mathbf{h}}^{U^T} \\ A_{\mathbf{h}}^{L^T} \end{pmatrix} \boldsymbol{z}_{\mathbf{h}} + (\nabla_{\bar{\mathbf{x}}}\bar{\mathbf{c}}_A)^T\boldsymbol{z}_{\bar{\mathbf{c}}} + H_U^T\boldsymbol{u} \tag{3.34}$$

$$= \begin{pmatrix} A_{\mathbf{g}}^{U^T} \\ A_{\mathbf{g}}^{L^T} \end{pmatrix} \boldsymbol{w}_{\mathbf{g}} + \begin{pmatrix} A_{\mathbf{h}}^{U^T} \\ A_{\mathbf{h}}^{L^T} \end{pmatrix} \boldsymbol{w}_{\mathbf{h}} + (\nabla_{\bar{\mathbf{x}}}\bar{\mathbf{c}}_A)^T\boldsymbol{w}_{\bar{\mathbf{c}}} + H_L^T\boldsymbol{v} \tag{3.35}$$

Because $(H_U^T, H_L^T) = I_n$ and $\boldsymbol{z}_{\bar{\mathbf{c}}} = \boldsymbol{w}_{\bar{\mathbf{c}}}$, one gets

$$\begin{aligned} &\begin{pmatrix} A_{\mathbf{g}}^{U^T} \\ A_{\mathbf{g}}^{L^T} \end{pmatrix} (\boldsymbol{z}_{\mathbf{g}} - \boldsymbol{w}_{\mathbf{g}}) + \begin{pmatrix} A_{\mathbf{h}}^{U^T} \\ A_{\mathbf{h}}^{L^T} \end{pmatrix} (\boldsymbol{z}_{\mathbf{h}} - \boldsymbol{w}_{\mathbf{h}}) \\ &= H_L^T \boldsymbol{v} - H_U^T \boldsymbol{u} = \begin{pmatrix} -\boldsymbol{u} \\ \boldsymbol{v} \end{pmatrix} \end{aligned} \tag{3.36}$$

Therefore,

$$\boldsymbol{u} = -A_{\mathbf{g}}^{U^T}(\boldsymbol{z}_{\mathbf{g}} - \boldsymbol{w}_{\mathbf{g}}) - A_{\mathbf{h}}^{U^T}(\boldsymbol{z}_{\mathbf{h}} - \boldsymbol{w}_{\mathbf{h}}) \tag{3.37}$$

$$\boldsymbol{v} = A_{\mathbf{g}}^{L^T}(\boldsymbol{z}_{\mathbf{g}} - \boldsymbol{w}_{\mathbf{g}}) + A_{\mathbf{h}}^{L^T}(\boldsymbol{z}_{\mathbf{h}} - \boldsymbol{w}_{\mathbf{h}}) \tag{3.38}$$

Hence, by applying Eq.(3.39) to Eq.(3.34), the following equation can be obtained.

$$\begin{aligned} -\nabla_{\bar{\mathbf{x}}} \tilde{f}^T(\mathbf{x}^*) &= \begin{pmatrix} A_{\mathbf{g}}^{U^T} \\ A_{\mathbf{g}}^{L^T} \end{pmatrix} \boldsymbol{z}_{\mathbf{g}} + \begin{pmatrix} A_{\mathbf{h}}^{U^T} \\ A_{\mathbf{h}}^{L^T} \end{pmatrix} \boldsymbol{z}_{\mathbf{h}} + (\nabla_{\bar{\mathbf{x}}} \bar{\mathbf{c}}_A)^T \boldsymbol{z}_{\bar{\mathbf{c}}} + H_U^T \boldsymbol{u} \\ &= (H_U^T, H_L^T) \begin{pmatrix} A_{\mathbf{g}}^{U^T} \\ A_{\mathbf{g}}^{L^T} \end{pmatrix} \boldsymbol{z}_{\mathbf{g}} + (H_U^T, H_L^T) \begin{pmatrix} A_{\mathbf{h}}^{U^T} \\ A_{\mathbf{h}}^{L^T} \end{pmatrix} \boldsymbol{z}_{\mathbf{h}} \\ &\quad + (\nabla_{\bar{\mathbf{x}}} \bar{\mathbf{c}}_A)^T \boldsymbol{\mu}_{\bar{\mathbf{c}}} - H_U^T [A_{\mathbf{g}}^{U^T}(\boldsymbol{z}_{\mathbf{g}} - \boldsymbol{w}_{\mathbf{g}}) + A_{\mathbf{h}}^{U^T}(\boldsymbol{z}_{\mathbf{h}} - \boldsymbol{w}_{\mathbf{h}})] \\ &= H_L^T A_{\mathbf{g}}^{L^T} \boldsymbol{z}_{\mathbf{g}} + H_L^T A_{\mathbf{h}}^{L^T} \boldsymbol{z}_{\mathbf{h}} + H_U^T A_{\mathbf{g}}^{U^T} \boldsymbol{w}_{\mathbf{g}} + H_U^T A_{\mathbf{h}}^{U^T} \boldsymbol{w}_{\mathbf{h}} \\ &\quad + (\nabla_{\bar{\mathbf{x}}} \bar{\mathbf{c}}_A)^T \boldsymbol{\mu}_{\bar{\mathbf{c}}} \end{aligned}$$

$$\begin{aligned} &= (H_U^T, H_L^T) \begin{pmatrix} A_{\mathbf{g}}^{U^T} \boldsymbol{w}_{\mathbf{g}} \\ A_{\mathbf{g}}^{L^T} \boldsymbol{z}_{\mathbf{g}} \end{pmatrix} + (H_U^T, H_L^T) \begin{pmatrix} A_{\mathbf{h}}^{U^T} \boldsymbol{w}_{\mathbf{h}} \\ A_{\mathbf{h}}^{L^T} \boldsymbol{z}_{\mathbf{h}} \end{pmatrix} \\ &\quad + (\nabla_{\bar{\mathbf{x}}} \bar{\mathbf{c}}_A)^T \boldsymbol{\mu}_{\bar{\mathbf{c}}} \\ &= \begin{pmatrix} A_{\mathbf{g}}^{U^T} \boldsymbol{w}_{\mathbf{g}} \\ A_{\mathbf{g}}^{L^T} \boldsymbol{z}_{\mathbf{g}} \end{pmatrix} + \begin{pmatrix} A_{\mathbf{h}}^{U^T} \boldsymbol{w}_{\mathbf{h}} \\ A_{\mathbf{h}}^{L^T} \boldsymbol{z}_{\mathbf{h}} \end{pmatrix} + (\nabla_{\bar{\mathbf{x}}} \bar{\mathbf{c}}_A)^T \boldsymbol{\mu}_{\bar{\mathbf{c}}} \end{aligned} \tag{3.39}$$

Due to the separable structure of $\mathbf{g}_A$ and $\mathbf{h}$, the Jacobians have the following block

structure:

$$\begin{aligned}\nabla_{\bar{\mathbf{x}}}\mathbf{g}_A(\mathbf{x}^*) &= (A^U_{\mathbf{g}}, A^L_{\mathbf{g}}) = \begin{pmatrix} \hat{A}^U_{\mathbf{g}} & 0 \\ 0 & \hat{A}^L_{\mathbf{g}} \end{pmatrix} \\ \nabla_{\bar{\mathbf{x}}}\mathbf{h}(\mathbf{x}^*) &= (A^U_{\mathbf{h}}, A^L_{\mathbf{h}}) = \begin{pmatrix} \hat{A}^U_{\mathbf{h}} & 0 \\ 0 & \hat{A}^L_{\mathbf{h}} \end{pmatrix}\end{aligned}$$

This implies further the block structure

$$A^U_{\mathbf{g}} = \begin{pmatrix} \hat{A}^U_{\mathbf{g}} \\ 0 \end{pmatrix}, \quad A^L_{\mathbf{g}} = \begin{pmatrix} 0 \\ \hat{A}^L_{\mathbf{g}} \end{pmatrix}$$

$$A^U_{\mathbf{h}} = \begin{pmatrix} \hat{A}^U_{\mathbf{h}} \\ 0 \end{pmatrix}, \quad A^L_{\mathbf{h}} = \begin{pmatrix} 0 \\ \hat{A}^L_{\mathbf{h}} \end{pmatrix}$$

Using this block structure and the definition of $\boldsymbol{\mu}_{\mathbf{g}}$ and $\boldsymbol{\lambda}$ in Eq.(3.30), one checks easily that

$$\begin{pmatrix} A^{U\,T}_{\mathbf{g}} \boldsymbol{w}_{\mathbf{g}} \\ A^{L\,T}_{\mathbf{g}} \boldsymbol{z}_{\mathbf{g}} \end{pmatrix} = \begin{pmatrix} A^{U\,T}_{\mathbf{g}} \\ A^{L\,T}_{\mathbf{g}} \end{pmatrix} \boldsymbol{\mu}_{\mathbf{g}}, \quad \begin{pmatrix} A^{U\,T}_{\mathbf{h}} \boldsymbol{w}_{\mathbf{h}} \\ A^{L\,T}_{\mathbf{h}} \boldsymbol{z}_{\mathbf{h}} \end{pmatrix} = \begin{pmatrix} A^{U\,T}_{\mathbf{h}} \\ A^{L\,T}_{\mathbf{h}} \end{pmatrix} \boldsymbol{\lambda} \tag{3.40}$$

Combining Eq.(3.40) with Eq.(3.39), one gets

$$\begin{aligned}-\nabla_{\bar{\mathbf{x}}}\tilde{f}^T(\mathbf{x}^*) &= \begin{pmatrix} A^{U\,T}_{\mathbf{g}} \\ A^{L\,T}_{\mathbf{g}} \end{pmatrix} \boldsymbol{\mu}_{\mathbf{g}} + \begin{pmatrix} A^{U\,T}_{\mathbf{h}} \\ A^{L\,T}_{\mathbf{h}} \end{pmatrix} \boldsymbol{\lambda} + (\nabla_{\bar{\mathbf{x}}}\mathbf{c}_A)^T \boldsymbol{\lambda}_{\mathbf{c}} \\ &= (\nabla_{\bar{\mathbf{x}}}\mathbf{g}_A(\bar{\mathbf{x}}^*))^T \boldsymbol{\mu}_{\mathbf{g}} + (\nabla_{\bar{\mathbf{x}}}\mathbf{h}(\bar{\mathbf{x}}^*))^T \boldsymbol{\lambda} + (\nabla_{\bar{\mathbf{x}}}\bar{\mathbf{c}}_A(\mathbf{x}^*))^T \boldsymbol{\mu}_{\bar{\mathbf{c}}}\end{aligned}$$

which shows that $\mathbf{x}^*$ is indeed a solution of Eq.(3.32). By Eq.(3.32) and (3.33), if $\mathbf{x}^*$ is a solution of both Eq.(3.23) and (3.24), then it also solves Eq.(3.19). $\triangleleft$

Since p and r are arbitrary numbers, letting $p = 0$ and $r = N$ makes forest $\boldsymbol{F}$ become the hierarchy of the relaxed design target problems and the argument by Michelena et al. [106] still holds for ATC with L_∞ norms, claiming that it is possible to find weights $\mathbf{w}_{(i+1)k}$ such that $\boldsymbol{\epsilon}_{(i+1)k}$ converges to zero. Therefore, the solution to ATC formulation with L_∞ norm solves the original problem.

3.2.3 Notational Modifications of SLP-filter Algorithm

In the SLP-filter algorithm presented by Fletcher et al.[57], every LP solution is evaluated for the system objective and constraints in order to check that the solution is acceptable to the current filter and the linear approximation is proper. Since the system objective and constraints are separated into elements, an equivalent system objective f_e is required, and defined by:

$$f_e(\bar{\mathbf{x}}_{11}, ..., \bar{\mathbf{x}}_{NM}) = \sum_{i=1}^{N} \sum_{j \in \mathcal{E}_i} f_{ij}(\bar{\mathbf{x}}_{ij}). \tag{3.41}$$

The equivalent predicted and actual reductions in $f_e(\bar{\mathbf{x}}_{11}, ..., \bar{\mathbf{x}}_{NM})$ are denoted as Δl_e and Δf_e, respectively, and they are calculated as

$$\begin{aligned} \Delta l_e &= \nabla f_e^T(\bar{\mathbf{x}}_{11}, ..., \bar{\mathbf{x}}_{NM}) \{\bar{\mathbf{d}}_{\bar{\mathbf{x}}_{11}}, ..., \bar{\mathbf{d}}_{\bar{\mathbf{x}}_{NM}}\} \\ &= \sum_{i=1}^{N} \sum_{j \in \mathcal{E}_i} \nabla f_{ij}^T \bar{\mathbf{d}}_{ij} \end{aligned} \tag{3.42}$$

$$\begin{aligned} \Delta f_e &= f_e(\bar{\mathbf{x}}_{11}, ..., \bar{\mathbf{x}}_{NM}) - f_e(\bar{\mathbf{x}}_{11} + \bar{\mathbf{d}}_{11}, ..., \bar{\mathbf{x}}_{NM} + \bar{\mathbf{d}}_{NM}) \\ &= \sum_{i=1}^{N} \sum_{j \in \mathcal{E}_i} f_{ij}(\bar{\mathbf{x}}_{ij}) - \sum_{i=1}^{N} \sum_{j \in \mathcal{E}_i} f_{ij}(\bar{\mathbf{x}}_{ij} + \bar{\mathbf{d}}_{ij}) \end{aligned} \tag{3.43}$$

The terms in Eq.(3.42) and Eq.(3.43), including ∇f_{ij}^T, $f_{ij}(\bar{\mathbf{x}}_{ij})$ and $f_{ij}(\bar{\mathbf{x}}_{ij} + \bar{\mathbf{d}}_{ij})$, are easily and independently obtained from the decomposed elements. Note that the deviation errors in Eq.(3.6) are not included in either the predicted or the actual reduction calculation. Instead, they are treated as additional equality constraints, and constraint violation functions η are expressed similarly to those in [59, 60],

$$\eta(\bar{\mathbf{x}}_{11}, ..., \bar{\mathbf{x}}_{NM}) = \left|\left|\mathbf{g}_{ij}^{+}(\bar{\mathbf{x}}_{ij})\right|\right|_1 + \left|\left|\left\{\mathbf{h}_{ij}(\bar{\mathbf{x}}_{ij}), \mathbf{c}_{ij} = \mathbf{t}_{ij} - \mathbf{r}_{ij}(\bar{\mathbf{x}}_{ij}))\right\}\right|\right|_1. \tag{3.44}$$

The term η replaces h in the publications cited above to avoid notational confusion; $\mathbf{g}_{ij}^{+}$ is a vector of constraint violation functions, $g^+ = \max(0, g)$. The decomposed constraints, $\mathbf{g}_{ij}^{+}(\bar{\mathbf{x}}_{ij})$, $\mathbf{h}_{ij}(\bar{\mathbf{x}}_{ij})$ and $\mathbf{r}_{ij}(\bar{\mathbf{x}}_{ij})$, can be obtained independently. Based on

the values in Eq.(3.41) to (3.44), acceptability to the current filter $\mathcal{F}$ is determined similarly to [57].

$$\eta \leq \beta^L \eta_{i_\mathcal{F}} \quad \text{or} \quad f_e \leq (f_e)_{i_\mathcal{F}} - \gamma^L \eta_{i_\mathcal{F}}, \quad \forall i_\mathcal{F} \in \mathcal{F}. \tag{3.45}$$

A trial point $\{\eta, f_e\}$, acceptable to $\mathcal{F}$, is regarded as an f-type iteration (improving f_e with a possible increase in η), an η-type iteration (reducing h with a possible increase in f_e), or an unacceptable point.

$$\text{f-type iteration} \quad : \Delta f_e^l \geq \sigma^L \Delta l_e^l \text{ and } \Delta l_e^l \geq \delta^L (\eta^l)^2 \tag{3.46}$$

$$\eta\text{-type iteration} \quad : \Delta l_e^l < \delta^L (\eta^l)^2 \tag{3.47}$$

$$\text{not acceptable} \quad : \text{otherwise.} \tag{3.48}$$

In Eq.(3.45), (3.46) and (3.47), $1 \sim \beta^L > \sigma^L > \gamma^L \sim 0$ and $\delta^L \sim 0$ are constants defined by users.

Note that the top level target in Eq.(3.6) may not be attainable in the early iterations due to small trust regions. For problems with unattainable targets, relaxation in the LATC formulation will result in arbitrarily small inconsistency deviations, if weights are chosen appropriately [105]. Additionally, filters ensure that η converges to zero as SLP iterations continue. Thus, the system inconsistency is enforced to converge to zero twice through LATC and SLP-filter algorithms, and the solution from Eq.(3.6) converges to the solution obtained from the LAIO problem, Eq.(3.2).

With the notational modification, the SLP-filter algorithm can be applied to solve Eq.(3.1), illustrated in Figure 3.3. In Step 1, a LATC problem, expressed in Eq.(3.6), is created and solved. If no compatible solution is found, it means that the current design point is located far from the feasible region compared to the current trust region. Therefore, a feasibility restoration phase is required to

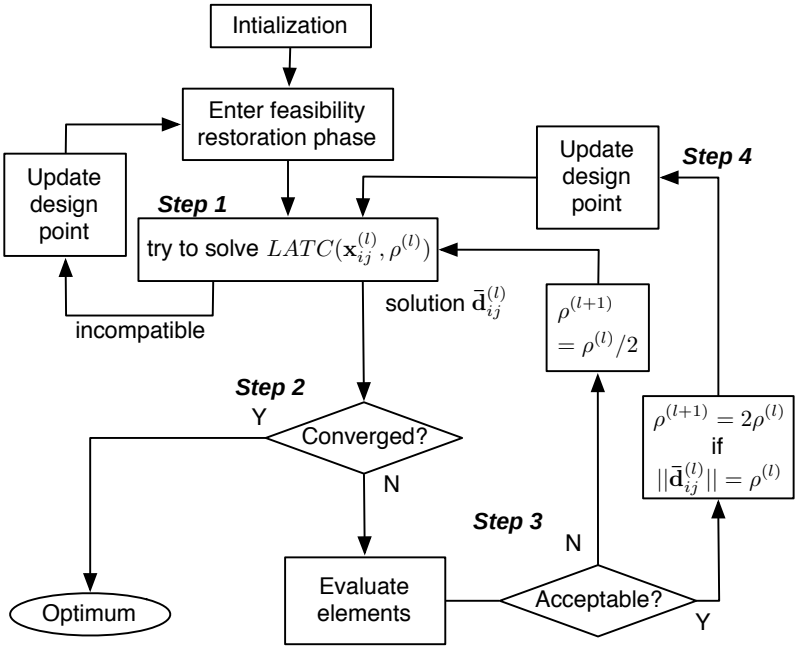

Figure 3.3: Flowcharts of SLP-based ATC

move the current design point close to the feasible region. During the feasibility restoration phase, the constraint violation is minimized by sacrificing the objective function value significantly. If a compatible solution is found, the algorithm checks if the solution satisfies convergence criteria in Step 2. If the convergence criteria are satisfied, the point is declared as an optimal point and the algorithm terminates. On the other hand, if the point is not optimal, the functions in the elements are evaluated separately. Then the point is checked if it is acceptable as the next design point based on Eq.(3.46), (3.47) and (3.48). If the point is acceptable, the point becomes this next design point and a new linear approximation is made around the next design point. Otherwise, the trust region is reduced by half.

3.2.4 Convergence Argument of SLP-based ATC

Since the solution to Eq.(3.6) is also a solution to Eq.(3.2) by the convergence proof of ATC with a L_∞ norm provided in the previous section, and the solution to

Eq.(3.1) equals the solution to Eq.(2.32), the equivalence of solutions from Eq.(3.1) and Eq.(3.2) needs to be proven in order to prove the convergence of linearized ATC with L_∞ norms, as illustrated in Figure 3.4. The argument is based on the convergence proof of SLP-filter and SQP-filter algorithms in [57] and [60], respectively.

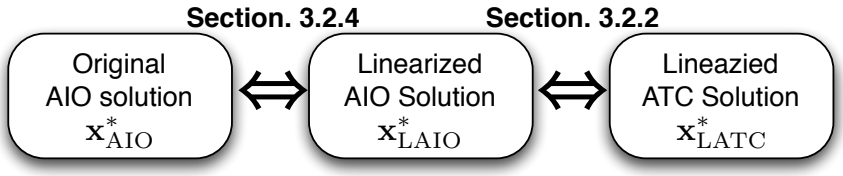

Figure 3.4: Convergence argument of SLP-based ATC

The proofs for the SLP-filter and SQP filter algorithms assumes the following standard assumptions.

1. *All points* $\mathbf{x}$ *that are sampled by the algorithm lie in a nonempty closed and bounded set* X*.*

2. *The problem functions* $f(\mathbf{x})$*,* $\mathbf{h}(\mathbf{x})$ *and* $\mathbf{g}(\mathbf{x})$ *are twice continuously differentiable on an open set containing* X*.*

3. *There exists a constant* $M^L > 0$ *such that* $|\frac{1}{2}\mathbf{s}^T(\nabla^2 f)\mathbf{s}| \leq M^L$*,* $||\frac{1}{2}\mathbf{s}^T(\nabla^2 g_i)\mathbf{s}||_\infty \leq M^L$ *and* $||\frac{1}{2}\mathbf{s}^T(\nabla^2 h_j)\mathbf{s}||_\infty \leq M^L$ *for all* $\mathbf{x} \in X$ *and all vectors* $\mathbf{s}$ *(*$||\mathbf{s}||_\infty = 1$*).*

One of the major differences between the two convergence proofs is the existence of equality constraints. Under the standard assumptions, the SLP-filter algorithm was proven to converge to a Karush-Kuhn-Tucker (KKT) point or an accumulation point that satisfies a Fritz-John condition for problems without equality constraints [57]. On the other hand, the SQP-filter algorithm converges to an accumulation point that satisfies KKT necessary conditions under a Mangasarian-Fromowitz Constraint Qualification (MFCQ), an extended form of the Fritz-John condition in the

presence of equality and inequality constraints [60]. Since the consistency constraints in Eq.(3.1) are equality constraints, we claim that the algorithm can be readily extended to problems with equality constraints under MFCQ. To verify the claim, we need to prove first that the modified AIO problem in Eq.(3.1) with consistency constraints holds under MFCQ if the original AIO problem in Eq.(2.32) holds under MFCQ.

Lemma 3.2.3. *Eq.(3.1) also satisfies MFCQ if and only if Eq.(2.32) satisfies MFCQ.*

Proof. A feasible point $\mathbf{x}^\circ$ of problem P satisfies MFCQ if and only if both (i) the vectors $\nabla \mathbf{h}_i^\circ$, are linearly independent and (ii) there exists a vector $\mathbf{s}$ that satisfies $\mathbf{s}^T \nabla \mathbf{h}^\circ = \mathbf{0}$, and $\mathbf{s}^T \nabla \mathbf{g}_A{}^\circ < 0$ where $\mathbf{g}_A$ denotes active inequality constraints at $\mathbf{x}^\circ$.

The structured AIO problem in Eq.(2.32) is rewritten here for convenience as:

$$\begin{aligned} \min_{\bar{\mathbf{x}}_{11},...,\bar{\mathbf{x}}_{NM}} \quad & \sum_{i=1}^{N} \sum_{j \in \mathcal{E}_i} f_{ij}(\bar{\mathbf{x}}_{ij}) \\ \text{subject to} \quad & \mathbf{g}_{ij}(\bar{\mathbf{x}}_{ij}) \leq \mathbf{0}, \quad \mathbf{h}_{ij}(\bar{\mathbf{x}}_{ij}) = \mathbf{0}, \\ \text{where} \quad & \bar{\mathbf{x}}_{ij} = [\mathbf{x}_{ij}, \mathbf{r}_{(i+1)k}], \quad \forall k \in \mathcal{C}_{ij}, \\ & \mathbf{r}_{ij} = \mathbf{a}_{ij}(\bar{\mathbf{x}}_{ij}), \quad \forall j \in \mathcal{E}_i, i = 1, ..., N. \end{aligned}$$

If Eq.(2.32) satisfies MFCQ at a feasible point $\mathbf{x}^\circ$, then $\nabla \mathbf{h}_{ij}$ and $\nabla(\mathbf{a}_{ij} - \mathbf{r}_{ij})$ are linearly independent and there exists a vector $\mathbf{s} = \{\mathbf{s}_{\mathbf{x_{11}}}, ..., \mathbf{s}_{\mathbf{x_{NM}}}, \mathbf{s}_{\mathbf{r_{22}}}, ..., \mathbf{s}_{\mathbf{r_{NM}}}\}$ that satisfies

$$\begin{aligned} \mathbf{s}^T \nabla \mathbf{h}_{ij} &= \mathbf{s}_{\mathbf{x}_{ij}}^T \nabla_{\mathbf{x}_{ij}} \mathbf{h}_{ij} + \mathbf{s}_{\mathbf{r}_{(i+1)k}}^T \nabla_{\mathbf{r}_{(i+1)k}} \mathbf{h}_{ij} = \mathbf{0} \\ \mathbf{s}^T \nabla (\mathbf{a}_{ij} - \mathbf{r}_{ij}) &= \mathbf{s}_{\mathbf{x}_{ij}}^T \nabla_{\mathbf{x}_{ij}} \mathbf{a}_{ij} + \mathbf{s}_{\mathbf{r}_{(i+1)k}}^T \nabla_{\mathbf{r}_{(i+1)k}} \mathbf{a}_{ij} - \mathbf{s}_{\mathbf{r}_{ij}}^T = \mathbf{0} \\ \mathbf{s}^T \nabla \mathbf{g}_{ij} &= \mathbf{s}_{\mathbf{x}_{ij}}^T \nabla_{\mathbf{x}_{ij}} \mathbf{g}_{ij} + \mathbf{s}_{\mathbf{r}_{(i+1)k}}^T \nabla_{\mathbf{r}_{(i+1)k}} \mathbf{g}_{ij} < \mathbf{0} \\ & \quad \forall k \in \mathcal{C}_{ij}, \quad \forall j \in \mathcal{E}_i, i = 1, ..., N. \end{aligned} \tag{3.49}$$

In Eq.(3.1), response copies of $\mathbf{r}_{ij}$ and consistency constraints $\mathbf{c}_{ij}$ are introduced.

Let $\bar{\mathbf{x}} = \{\mathbf{x}_{11}, ..., \mathbf{x}_{NM}, \mathbf{r}_{22}, ..., \mathbf{r}_{NM}, \mathbf{t}_{22}, ..., \mathbf{t}_{NM}\}$. Due to the consistency constraints, a feasible point $\bar{\mathbf{x}}^\circ$ satisfies $\mathbf{r}_{ij}^\circ = \mathbf{t}_{ij}^\circ, \forall j \in \mathcal{E}_i, i = 2, ..., N$.

In order to prove the lemma, first we need to prove part (i) above, namely, the gradients of all equality constraints in Eq.(3.1) are linearly independent if the vectors $\nabla \mathbf{h}_i^\circ$, are linearly independent. Since $\nabla \mathbf{h}_{ij}$ and $\nabla(\mathbf{a}_{ij} - \mathbf{r}_{ij})$ in Eq.(2.32) are linearly independent, $\nabla \mathbf{h}_{ij}$ and $\nabla(\mathbf{a}_{ij} - \mathbf{r}_{ij})$ in Eq.(3.1) are also linearly independent. In addition, since $\nabla \mathbf{c}_{ij}$ in Eq.(3.1) consists of 1 for $\mathbf{t}_{ij}$ and -1 for $\mathbf{r}_{ij}$, the rows in $\nabla \mathbf{c}_{ij}$ are linearly independent of each other. Also, because $\mathbf{c}_{ij}$ must include the $\mathbf{r}_{ij}$s that are not included in $\mathbf{h}_{ij}$, $\nabla \mathbf{c}_{ij}$ and $\nabla \mathbf{h}_{ij}$ are linearly independent of each other. Similarly, since $(\mathbf{a}_{ij} - \mathbf{r}_{ij})$ contains variables with two different level indices, namely $\mathbf{r}_{ij}$ and $\mathbf{t}_{(i+1)k}$, then $\nabla(\mathbf{a}_{ij} - \mathbf{r}_{ij})$ are linearly independent of $\nabla \mathbf{c}_{ij}(\bar{\mathbf{t}}_{ij}, \bar{\mathbf{r}}_{ij})$. Thus, the gradients of all equality constraints in Eq.(3.1) are linearly independent if $\nabla \mathbf{h}_{ij}$ and $\nabla(\mathbf{a}_{ij} - \mathbf{r}_{ij})$ in Eq.(2.32) are linearly independent. The "only if" part can be proven easily in a similar way.

Now we need to prove part (ii) above, namely, there exists a vector $\bar{\mathbf{s}}$ that satisfies $\bar{\mathbf{s}}^T \nabla \mathbf{h}^\circ = \mathbf{0}$, $\bar{\mathbf{s}}^T \nabla(\mathbf{a}^\circ - \mathbf{r}^\circ) = \mathbf{0}$, $\bar{\mathbf{s}}^T \nabla \mathbf{c}^\circ = \mathbf{0}$ and $\bar{\mathbf{s}}^T \nabla \mathbf{g}_A{}^\circ < \mathbf{0}$ where $\mathbf{g}_A$ denotes active inequality constraints at $\mathbf{x}^\circ$.

Let $\bar{\mathbf{s}} = \{\bar{\mathbf{s}}_{\mathbf{x_{11}}}, ..., \bar{\mathbf{s}}_{\mathbf{x_{NM}}}, \bar{\mathbf{s}}_{\mathbf{r_{22}}}, ..., \bar{\mathbf{s}}_{\mathbf{r_{NM}}}, \bar{\mathbf{s}}_{\mathbf{t_{22}}}, ..., \bar{\mathbf{s}}_{\mathbf{t_{NM}}}\}$

$= \{\mathbf{s}_{\mathbf{x_{11}}}, ..., \mathbf{s}_{\mathbf{x_{NM}}}, \mathbf{s}_{\mathbf{t_{22}}}, ..., \mathbf{s}_{\mathbf{t_{NM}}}, \mathbf{s}_{t_{22}}, ..., \mathbf{s}_{\mathbf{t_{NM}}}\}$. Then $\bar{\mathbf{s}}^T \nabla \mathbf{c}^\circ = \mathbf{0}$ is satisfied. Also, from Eq.(3.49)

$$\begin{aligned}
\mathbf{s}^T \nabla \mathbf{h}_{ij} &= \mathbf{s}_{\mathbf{x}_{ij}}^T \nabla_{\mathbf{x}_{ij}} \mathbf{h}_{ij} + \mathbf{s}_{\mathbf{t}_{(i+1)k}}^T \nabla_{\mathbf{t}_{(i+1)k}} \mathbf{h}_{ij} = \mathbf{0} \\
\mathbf{s}^T \nabla(\mathbf{a}_{ij} - \mathbf{r}_{ij}) &= \mathbf{s}_{\mathbf{x}_{ij}}^T \nabla_{\mathbf{x}_{ij}} \mathbf{a}_{ij} + \mathbf{s}_{\mathbf{t}_{(i+1)k}}^T \nabla_{\mathbf{t}_{(i+1)k}} \mathbf{a}_{ij} - \mathbf{s}_{\mathbf{r}_{ij}}^T = \mathbf{0} \\
\mathbf{s}^T \nabla \mathbf{g}_{ij} &= \mathbf{s}_{\mathbf{x}_{ij}}^T \nabla_{\mathbf{x}_{ij}} \mathbf{g}_{ij} + \mathbf{s}_{\mathbf{t}_{(i+1)k}}^T \nabla_{\mathbf{t}_{(i+1)k}} \mathbf{g}_{ij} < \mathbf{0} \\
&\quad \forall k \in \mathcal{C}_{ij}, \quad \forall j \in \mathcal{E}_i, i = 1, ..., N.
\end{aligned} \tag{3.50}$$

because $\nabla_{\mathbf{r}_{(i+1)k}}\mathbf{h}_{(i+1)k}$, $\nabla_{\mathbf{r}_{(i+1)k}}\mathbf{a}_{(i+1)k}$ and $\nabla_{\mathbf{r}_{(i+1)k}}\mathbf{g}_{(i+1)k}$ in Eq.(3.49) are equivalent to $\nabla_{\mathbf{t}_{(i+1)k}}\mathbf{h}_{(i+1)k}$, $\nabla_{\mathbf{r}_{(i+1)k}}\mathbf{a}_{(i+1)k}$ and $\nabla_{\mathbf{r}_{(i+1)k}}\mathbf{g}_{(i+1)k}$ in Eq.(3.50), respectively.

For the "only if" part, if MFCQ is satisfied for Eq.(3.1), $\bar{\mathbf{s}}_{\mathbf{r}} = \bar{\mathbf{s}}_{\mathbf{t}}$ from the consistency constraints. Then $\mathbf{s}^T\nabla\mathbf{h}^\circ = \mathbf{0}$, $\mathbf{s}^T\nabla(\mathbf{a}^\circ - \mathbf{r}^\circ) = \mathbf{0}$ and $\mathbf{s}^T\nabla\mathbf{g}_A{}^\circ < \mathbf{0}$ can be proven easily in a similar way. $\triangleleft$

Since MFCQ holds with the consistency constraints, we can apply the convergence proof in [60]. If the standard assumptions are satisfied and the original problem is compatible within a round-off error, the SLP filter algorithm (A) finds a KKT point or (B) has an infinite subsequence of consecutive f-type or η-type iterations [57]. Now we will show that if (B) occurs, the algorithm converges to a feasible point and, if MFCQ holds, the set of directions $\mathbf{s}$ in Eq.(3.51) is empty:

$$\{\mathbf{s}| \quad \mathbf{s}^T\nabla f_e < 0, \quad \mathbf{s}^T\nabla\mathbf{g}_A < \mathbf{0}, \quad \mathbf{s}^T\nabla\mathbf{h} = \mathbf{0}, \quad \mathbf{s}^T\nabla\bar{\mathbf{c}} = \mathbf{0}\}, \tag{3.51}$$

where $\mathbf{g}_A$ is the active inequality constraints.

The trust region radius ρ^l decreases and ultimately $\rho^l \to 0$. When the trust region is reduced, a trial point will be found that is acceptable, and either an f-type iteration or an η-type iteration will occur. For the resulting ρ^l,

$$\begin{cases} \text{if } \rho^l \le (1-\sigma^L)\epsilon^L/M^L, \text{ then } \Delta f_e^l > \sigma^L \Delta l_e^l, \\ \text{if } (\rho^l)^2 \le \beta^L\tau^l/mM^L, \text{ then } \eta(\mathbf{x}^l + \mathbf{d}^l) \le \beta^L\tau^l, \end{cases} \tag{3.52}$$

where $0 < \epsilon^L \le \min\{-(\nabla f_e^l)^T\mathbf{s}^l, -(\nabla\mathbf{g}_A^l)^T\mathbf{s}^l\}, \tau^l = \min_{i\in\mathcal{F}} \eta_i$, m is the number of all constraints, and M^L is the upper bound for $|\frac{1}{2}\mathbf{d}^T(\nabla^2 f_e)\mathbf{d}|$, $||\frac{1}{2}\mathbf{d}^T(\nabla^2\mathbf{g})\mathbf{d}||_\infty$, $||\frac{1}{2}\mathbf{d}^T(\nabla^2\mathbf{h})\mathbf{d}||_\infty$ and $||\frac{1}{2}\mathbf{d}^T(\nabla^2\mathbf{c})\mathbf{d}||_\infty$. Also, $\mathbf{s}^l$ is the unit vector of the projection of $\mathbf{d}$ to the space spanning the equality constraints.

Let the sequence of $\mathbf{x}^l$ of (B) converge to $\mathbf{x}^\infty$. From the assumption that the objective function f_e is bounded, the filter envelop test in Eq.(3.45) ensures $\sum \eta^{l+1}$ is bounded and $\eta^l \to 0$, so $\mathbf{x}^\infty$ is feasible [57]. The main sequence contains an infinite number of f-type or η-type iterations. Then we assume that MFCQ is satisfied and consider the proposition (to be contradicted) that $\mathbf{x}^\infty$ is not a KKT point. Then, it is always possible to find a solution of Eq.(3.2) with a trust region satisfying Eq.(3.53) from [57, 60].

$$\frac{\eta^l}{\epsilon^L} \leq \rho \leq \min\ \{\frac{(1-\sigma^L)\epsilon^L}{M^L}, \frac{\epsilon^L}{M^L}, \frac{\bar{c}^l}{\bar{a}^l}, \frac{\sigma^L \epsilon^L}{\gamma^L m M^L}, \sqrt{\frac{\beta^L \tau^l}{m M^L}}\} \tag{3.53}$$

where $0 \leq \bar{c}^l \leq -\max\{\mathbf{g}^l_{\tilde{A}}\}$ and $\bar{a}^l \geq \max\{(\nabla \mathbf{g}^l_{\tilde{A}})^T \mathbf{s}\}$. $\mathbf{g}_{\tilde{A}}$ denotes the vector of inactive inequality constraints. For sufficiently large l, it is not possible for any value of $\eta^l \leq \epsilon^L \rho$ to satisfy Eq.(3.47) since Δl^l_e decreases monotonically as ρ decreases. Thus, for sufficiently large l, f-type iterations are always generated. Then both left- and right-sides of Eq.(3.53) remain constant because η^l and τ^l are not updated. Therefore, for sufficiently large l, Δf_e does not converge to zero. This contradicts the fact that f_e is bounded. Thus by contradiction, for a sufficiently large l, the algorithm has an accumulation point that is feasible and is either a KKT point or fails to satisfy MFCQ.

If the original nonlinear problem of Eq.(2.32) is assumed to be well bounded and have a solution, the sequence of solutions of Eq.(3.2) should converge to the solution of Eq. (2.32) if targets and responses are bounded. That is, if the decomposed systems are coupled through variables that are well bounded, the solution of Eq.(3.2) converges to the point that satisfies the necessary conditions for solving Eq.(2.32).

3.3 Suspension Strategy for SLP-based ATC

Even though LATC and LAIO converge to a very similar solution with small relaxation errors, LATC may require more computations to obtain a converged solution than LAIO due to coordination costs. During the LATC solution, however, the objectives and constraints are not evaluated. Indeed, in this dissertation, we focus on the reduction in the number of function evaluations during the SLP-based ATC algorithm, rather than improvement in LATC performance, such as the convergence rate or deviation errors in the ATC strategy. To this end, we take advantage of decomposed design tasks.

Linking variables represent couplings between elements. Elements that are weakly coupled will likely be less sensitive to linking variables than to local variables. Therefore, changes in the target for an element that are sufficiently small will not have significant impact on the system objective. In this case, the change in the target can be neglected during a given iteration and the element in the branch can be "suspended" from redesign (or evaluation) [8, 53, 76]. For example, let us assume that the step size of $\mathbf{t}_{22}$ in Figure 3.5 is considerably smaller than that of $\mathbf{t}_{23}$ at iteration l. Then the elements in the corresponding branch, including O_{22}, O_{34} and O_{35}, can

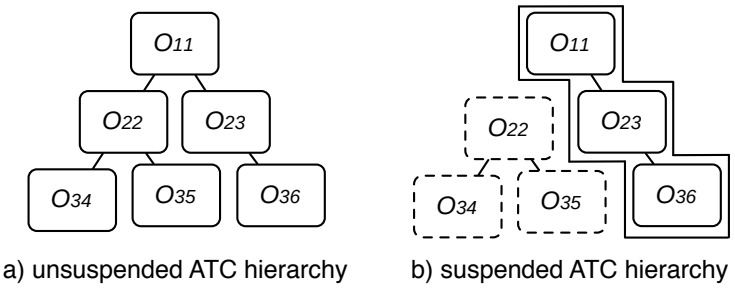

Figure 3.5: Examples of the unsuspended and suspended ATC hierarchies

be suspended from evaluation for f_{ij}^{l+1}, $\mathbf{g}_{ij}^{l+1}$ and $\mathbf{h}_{ij}^{l+1}$ and the values at iteration l are used instead while the actual functions in the unsuspended element (e.g. O_{11}, O_{23} and O_{36} in Figure 3.5) are evaluated to obtain Δf_e and η.

The SLP-based ATC with suspension strategy, shown in Figure 3.6, requires several minor steps in Step 2 of SLP-based ATC without suspension strategy. The steps in the suspension strategy (solid boxes) are described in more detail below.

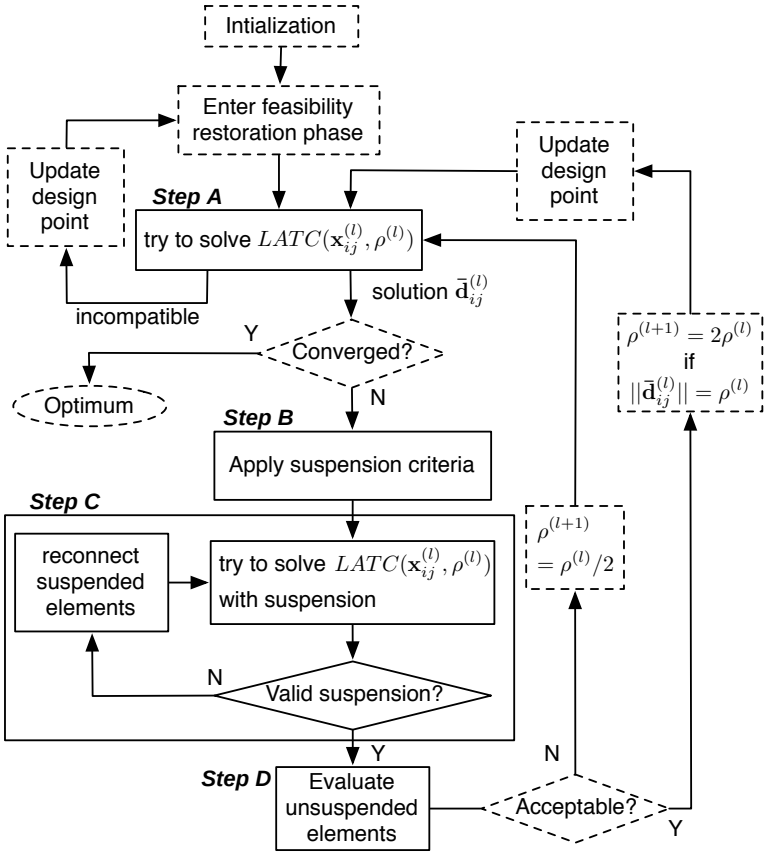

Figure 3.6: Flowcharts of SLP-based ATC with suspension strategy

Step A: Attempt to solve $LATC(\bar{\mathbf{x}}_{ij}^{l}, \rho^{l})$

Eq.(3.6) is solved using a "standard" ATC strategy to obtain $\bar{\mathbf{d}}_{ij}^{l}$. If any elements in the system are incompatible, a feasibility restoration phase is evoked in order

to find a point that is both acceptable and compatible. Once the LATC strategy converges to a solution that is compatible, the step sizes are compared in order to determine active and suspended elements in the next step.

Step B: Apply suspension criteria

This step selects the set of elements that can be suspended based on the step size of the solution's targets from the previous step. With the solution of element j at level i, the step sizes for targets $\mathbf{d}^l_{\mathbf{t}_{(i+1)k}}$ are compared. If a target to a child m satisfies

$$||\mathbf{d}^l_{\mathbf{t}_{(i+1)m}}|| < \zeta_t \sum_{k \in \mathcal{C}_{ij}} \frac{||\mathbf{d}^l_{\mathbf{t}_{(i+1)k}}||}{NC_{ij}}, \tag{3.54}$$

then the elements in the corresponding branch are selected for suspension. The parameter $\zeta_t << 1$ is chosen based on the designer's experience and NC_{ij} is the number of children of element j at level i. The suspension idea is similar to that in [8], and so the Modified Global Sensitivity Equations (MGSEs) may provide an estimation for the impact of the target changes that is accurate enough to reduce iteration between steps B and C. In this dissertation, however, simple comparison on step sizes is used because MGSEs may require additional function evaluations. The predicted reduction without suspension Δl_e needs to be obtained from the solution for validation at Step C.

Step C: Suspension validation

In this step, LATC is solved again after suspending the elements selected in the previous step to estimate the effect of suspended elements. The suspension can be readily implemented by setting the responses of the suspended elements to zero

($\mathbf{d}^l_{\mathbf{t}_{(i+1)m}} = 0$). Once the solution is obtained, the predicted reduction in f_e with suspended elements Δl_e^{sus} is calculated. If $\Delta l_e^{\text{sus}} \geq \zeta_f \Delta l_e$, the suspension is assumed to be valid. The parameter $\zeta_f < 1$ is also chosen based on the designers experience. Otherwise, the suspension is declared to be inadequate and some of the suspended elements must be reactivated if more than two elements are selected for suspension. After reactivation, LATC is solved again until suspension is valid or all elements are active. Because the validation criteria are satisfied once all elements are reactivated, the loop in this step terminates finitely.

Step D: Evaluation

Only active elements are evaluated because the step sizes of suspended elements are all set to zero in the previous step. For the suspended elements, the values from iteration k can be used.

The suspension criteria presented here, including the validation step, can be made conservative by setting $\zeta_t \to 0$, $\zeta_f \to 1$. The numerical examples presented in Section 3.4 show that the number of function evaluations saved by the suspension strategy depends highly on the values of ζ_t and ζ_f. Also the convergence of the coordination strategy is not guaranteed with the implementation of the suspension strategy because the suspension strategy is heuristic. However, the method remains attractive in design problems because even if convergence is not attained, the intermediate solutions are feasible and usually represent an improvement in the objective function. Defining parameters ranges that guarantee both convergence and reduction in function evaluations is a subject for further research.

3.4 Numerical Results

This section provides two test examples to illustrate the proposed algorithm. Both examples have three elements: one at the top level and two at the bottom level. One child element is more weakly coupled to the top level element than the other since the proposed suspension strategy is expected to be more effective on problems whose elements have significantly different coupling strengths.

In the examples, ATC problems are formulated from AIO problems and solved with the SLP-filter algorithm. Results from calculations with and without the suspension strategy are compared to each other, and also to results from the original AIO problems solved by SLP-filter and SQP algorithms.

3.4.1 Example 1: Modified Hock and Schittkowski Problem 34

Problem 34 in the classical test collection by Hock and Schittkowski [72] is modified so that the problem can be decomposed into three elements. The original AIO problem is

$$\begin{aligned} \min_{x_1,\ldots,x_6} \quad & f = -x_1 x_4 \\ \text{subject to} \quad & g_1 \equiv \exp(x_1) - x_2 x_5 \leq 0, \\ & g_2 \equiv \exp(x_2) - x_3 \leq 0, \\ & g_3 \equiv \log(5x_4^2) - x_5 \leq 0, \\ & g_4 \equiv x_5^2 - 10x_6 \leq 0, \end{aligned} \tag{3.55}$$

where the lower and upper bounds of $\mathbf{x}$ are $\{0, 0, 0, 0.01, 0, 0\}$ and $\{100, 100, 10, 100, 100, 5\}$. The unique optimal solution is $\mathbf{x}^* = \{2.79, 2.30, 10.00, 15.35, 7.07, 5.00\}$ with all constraints active.

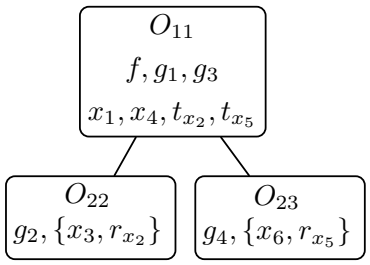

Figure 3.7: Modified Hock and Schittkowski Problem 34

Eq.(4.13) is decomposed into one top-level element (O_{11}) with two children (O_{22} and O_{23}), as illustrated in Figure 3.7. The linking variables that couple O_{11} with O_{22} and O_{23} are x_2 and x_5, respectively. Then O_{11} minimizes the sum of system objective f and deviation errors ϵ_{22} and ϵ_{23} with respect to $\bar{\mathbf{x}}_{11} = \{x_1, x_4, t_{x_2}, t_{x_5}, \epsilon_{22}, \epsilon_{23}\}$, subject to g_1 and g_3. O_{22} minimizes ϵ_{22} with respect to $\bar{\mathbf{x}}_{22} = \{x_3, r_{x_2}, \epsilon_{22}\}$, subject to g_2, while O_{23} minimizes ϵ_{23} with respect to $\bar{\mathbf{x}}_{23} = \{x_6, r_{x_5}, \epsilon_{23}\}$, subject to g_4. Parameters for the suspension strategy are set to $\zeta_t = 0.2$ and $\zeta_f = 0.8$, and the initial trust region is set to 20.

Table 4.1 summarizes the final solutions and the number of function evaluations for each element obtained from the five algorithms: *LATC* denotes the results obtained from the SLP-based ATC strategy without suspension strategy, *LATC-SS* denotes the SLP-based ATC strategy with suspension strategy, *ATC* denotes the "standard" ATC strategy with a quadratic penalty function, *AIO-SLP* denotes the SLP-filter algorithm solving the AIO problem and *AIO-SQP* denotes the SQP algorithm solving the AIO problem. All algorithms converge to the same solution. The L_∞ norms of consistency errors for *LATC*, *LATC-SS* and *ATC* are 3.55×10^{-15}, 1.78×10^{-15} and 4.57×10^{-10}, respectively.

Note that element O_{11} requires three functions to be calculated (f, g_1, g_3), while

Table 3.1: Optimal solutions and number of redesigns for Example 1

	$\mathbf{x}^*$	f^*	number of redesigns			
			O_{11}	O_{22}	O_{23}	total
LATC	$\{2.79, 2.30, 10.00, 15.35, 7.07, 5.00\}$	-42.83	$56^\dagger$	$36^\dagger$	$36^\dagger$	$128^\dagger$
LATC-SS	$\{2.79, 2.30, 10.00, 15.35, 7.07, 5.00\}$	-42.83	$56^\dagger$	$36^\dagger$	$17^\dagger$	$109^\dagger$
ATC	$\{2.79, 2.30, 10.00, 15.35, 7.07, 5.00\}$	-42.83	$777^\dagger$	$164^\dagger$	$154^\dagger$	$1095^\dagger$
AIO-SLP	$\{2.79, 2.30, 10.00, 15.35, 7.07, 5.00\}$	-42.83				$98^\ddagger$
AIO-SQP	$\{2.79, 2.30, 10.00, 15.35, 7.07, 5.00\}$	-42.83				$112^\ddagger$

† Element O_{11} contains one objective and two constraints while element O_{22} and O_{23} include one constraint function.

‡ AIO problem contains one objective and four constraints.

O_{22} and O_{23} require one function (g_2 and g_4). If we define the computation cost of LATC to be $(3 \times 56 + 36 + 36)$ and use it as a baseline, then the normalized computational costs of *LATC-SS*, *ATC*, *AIO-SLP* and *AIO-SQP* are 0.92, 11.0, 2.04 and 2.33, respectively. Here we assume that the computational cost of function evaluation is larger than that of the coordination overhead. Also, the weights on L_∞ norms and quadratic penalty functions are initialized to 1 at every SLP iteration and doubled at every ATC iteration. Thus, if the weighting update method is used, the accuracy and local convergence of *LATC*, *LATC-SS* and *ATC* could be improved [105]. The method should be more effective on *ATC* because no function evaluations are made during the inner coordination of *LATC* and *LATC-SS*.

The problem is monotonic for all design variables, and so SLP algorithms have fast convergence. In addition to the effect of monotonicity, decomposition reduces significantly the number of computations by eliminating unnecessary gradient calculations. The suspension strategy also reduces computations by reducing the number of redesigns for O_{23}. Figure 3.8 shows the history of target values for O_{22} and O_{23}. The step sizes of x_5 are sufficiently smaller than those of x_2 at iterations 2, 3, 5, 7 and 9, and so O_{23} is suspended at these iterations and the previous values of g_4 and

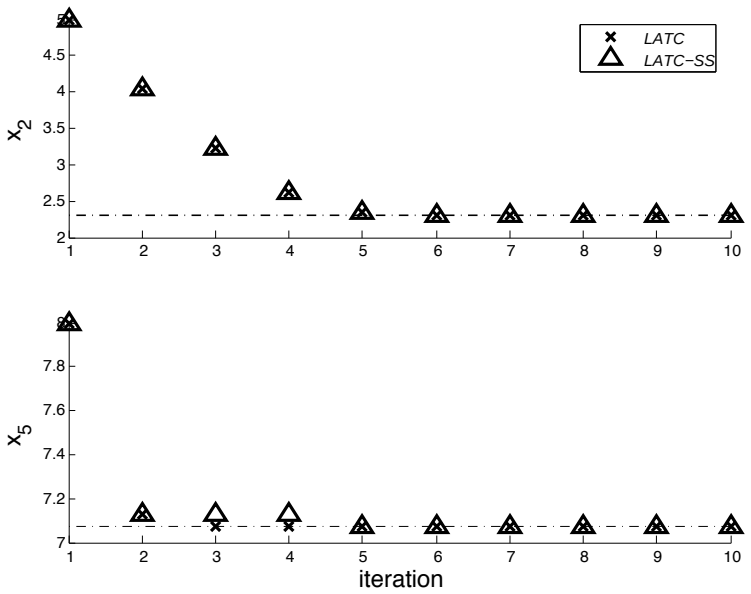

Figure 3.8: History of targets to element O_{22} and element O_{23}

∇g_4 are used instead.

3.4.2 Example 2: Allison's Structural Optimization Problem

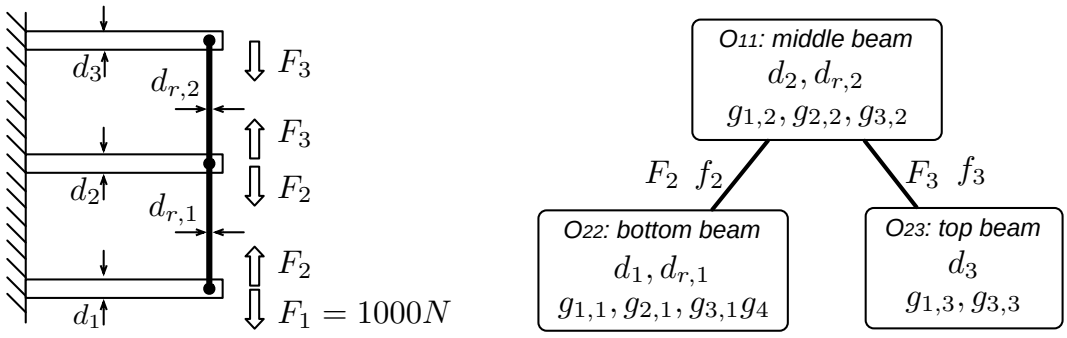

(a) Physical structure of Example 3

(b) Hierarchical problem structure of Example 3

Figure 3.9: Three-bar two-rod structural design problem (modified from [126])

The second example, illustrated in Figure 3.9 is a structural optimization problem based on the analytical mass allocation problem of Allison et al. [7] and Tosserams et al. [126] with some modifications. In the hierarchy, the element at the second level

(the middle bar) is relocated to the top level and the other two are located at the bottom level. The coupling strength between the second and third rod is strengthed. The original AIO problem is

$$\begin{aligned}
\min_{d_1,d_2,d_3,d_{r1},d_{r2}} \quad & \sum_{i=1}^{3} m_i + \sum_{j=1}^{2} m_{r,j} \\
\text{subject to} \quad & g_{1,i} \equiv \sigma_{b,i} - \bar{\sigma} \leq 0 \quad i = 1,2,3 \\
& g_{2,j} \equiv \sigma_{a,j} - \bar{\sigma} \leq 0 \quad j = 1,2 \\
& g_{3,i} \equiv (F_i - F_{i+1}) - \bar{F}_{t,i} \leq 0 \quad i = 1,2,3 \\
& g_4 = f_1 - \bar{f}_1 \leq 0 \\
& h_{1,j} \equiv f_j - f_{j+1} - f_{r,j} = 0 \quad j = 1,2 \\
\text{where} \quad & m_i = \tfrac{\pi}{4} d_i^2 L\rho, \quad \sigma_{b,i} = \tfrac{32L(F_i - F_{i+1})}{\pi d_i^3}, \\
& f_i = \tfrac{64L^3(F_i - F_{i+1})}{3\pi E_i d_i^4}, \quad i = 1,2,3; \\
& m_{r,j} = \tfrac{\pi}{4} d_{r,j}^2 L\rho, \quad \sigma_{a,j} = \tfrac{4F_{j+1}}{\pi d_{r,j}^2}, \\
& f_{r,j} = \tfrac{4F_{j+1}L}{\pi E_{r,j} d_{r,j}^2} \quad j = 1,2
\end{aligned} \tag{3.56}$$

where m_i is the mass of beam i, $m_{r,j}$ is the mass of rod j, $\sigma_{b,i}$ is the bending stress in beam i, $\sigma_{a,j}$ is the axial stress in rod j, f_i is the vertical deflection of beam i and $f_{r,j}$ is the elongation of rod j. Constraint limits for stress ($\bar{\sigma}$), transmitted force ($\bar{F}_t$) and vertical deflection of beam 1 (f_1) are set to $127 \cdot 10^6 \text{N/m}^2$, 400N and 27mm, respectively. The equality constraints can be solved explicitly to obtain F_2 and F_3. The length of beams and rods L and the density of the material ρ are fixed to be 1m and 2700kg/m^3, respectively. Similar to [126], 1000N is vertically applied at the end of beam 1 ($F_1 = 1000\text{N}$). In order to apply different coupling strengths, the Young's moduli of the beams and rods are set differently, such as $E_1 = E_2 = E_{r,1} = 70\text{GPa}$, $E_3 = 700\text{GPa}$, $E_{r,2} = 7\text{GPa}$. Therefore, the coupling strength between beams 2 and 3 becomes significantly stronger than that between beam 1 and

Table 3.2: Optimal solutions and the number of redesigns for Example 2

	$\mathbf{x}^*$	f^*	number of redesigns			
			O_{11}	O_{22}	O_{23}	total
LATC	$\{34.62, 34.84, 25.22, 40.11, 37.52\}$	12.78	$445^\dagger$	$329^\dagger$	$271^\dagger$	$1045^\dagger$
LATC-SS	$\{34.62, 34.84, 25.22, 40.11, 37.52\}$	12.78	$486^\dagger$	$127^\dagger$	$288^\dagger$	$901^\dagger$
ATC	$\{34.62, 34.84, 25.22, 40.11, 37.52\}$	12.78	$895^\dagger$	$336^\dagger$	$506^\dagger$	$1737^\dagger$
AIO-SLP	$\{34.62, 34.84, 25.22, 40.11, 37.52\}$	12.78				$547^\ddagger$
AIO-SQP	$\{34.62, 34.84, 25.22, 40.11, 37.52\}$	12.78				$418^\ddagger$

† Elements O_{11}, O_{22} and O_{23} contain five, six and three functions, respectively.
‡ AIO problem contains one objective and eleven constraints.

2. The lower and upper bounds of $\mathbf{x}$ are set to $\{0.001, 0.001, 0.001, 0.0001, 0.0001\}$ and $\{0.06, 0.06, 0.06, 0.006, 0.006\}$.

The local variables at the top-level element O_{11} are the dimensions of beam 2 and rod 2 ($\mathbf{x}_{11} = \{d_2, d_{r,2}\}$) while those at the two bottom-level elements, O_{22} and O_{23}, are the dimensions of beam 1 and rod 1, and beam 3, respectively ($\mathbf{x}_{22} = \{d_1, d_{r,1}\}$ and $\mathbf{x}_{23} = \{d_3\}$). Element O_{11} is coupled with O_{22} and O_{23} through corresponding axial forces and deflections that are $\{F_2, f_2\}$ and $\{F_3, f_3\}$, respectively. Then O_{11} minimizes the sum of $f_{11} = m_2 + m_{r,2}$ and deviation errors ϵ_{22} and ϵ_{23}, subject to $g_{1,2}$, $g_{2,2}$, $g_{3,2}$ and $h_{1,2}$. O_{22} minimizes the sum of $f_{22} = m_1 + m_{r,1}$ and ϵ_{22}, subject to $g_{1,1}$, $g_{2,1}$, $g_{3,1}$, g_4 and $h_{1,1}$, while O_{23} minimizes the sum of $f_{23} = m_3$ and ϵ_{23}, subject to $g_{1,3}$ and $g_{3,3}$. Since SLP-based algorithms are more effective when problems are well-scaled, the diameters of beams and rods are multiplied by 1000 and 10000, respectively. The scaled initial point is $\mathbf{x}_s^0 = \{30, 30, 25, 30, 30\}$. Parameters for the suspension strategy are set to $\zeta_t = 0.2$ and $\zeta_f = 0.8$, and the initial trust region is set to 0.4.

Table 4.3 summarizes the final solutions and the number of function evaluations for each element obtained from the five algorithms. The results show that the pro-

posed algorithms converge to the same solution obtained from the other algorithms solving the AIO problem. The L_∞ norms of consistency errors of *LATC*, *LATC-SS* and *ATC* are 6.21×10^{-4}, 1.65×10^{-4} and 2.98×10^{-3}, respectively. Unlike the previous example, the initial point and initial size of trust regions affect significantly the convergence of the SLP-based algorithms. The three elements include different numbers of functions to be evaluated, and the normalized computational cost of *LATC-SS*, *ATC*, *AIO-SLP* and *AIO-SQP* are 0.81, 1.60, 1.31 and 1.00, respectively.

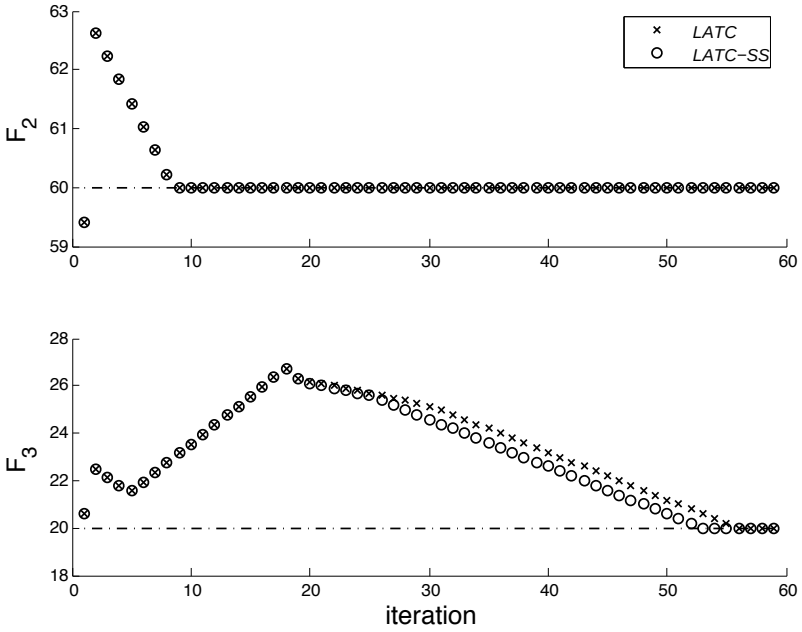

Figure 3.10: History of targets to element O_{22} and element O_{23}

Without linearity and monotonicity, SLP-based algorithms show no advantages over a sequential quadratic programming algorithm. On the other hand, applying the suspension strategy halves the number of redesigns in O_{22} even though the number of redesigns in the other elements increases slightly. Figure 3.10 shows the history of target values for O_{22} and O_{23}. Since O_{22} reaches the optimum within 10 iterations, this element is evaluated only a few times during the remaining iterations until O_{23}

converges to the optimum.

Tradeoffs between computational cost reductions in O_{22} and increases in O_{11} and O_{23} are observed by varying ζ_t and ζ_f. Since the selection of ζ_t and ζ_f is based on user experience, a more rigorous measure that is less sensitive to problem types needs to be developed.

3.5 Concluding Remarks

SLP-filter algorithms were introduced into an ATC formulation to reduce computational costs for some problem classes. In the proposed algorithm, the linearized subproblems have significantly lower levels of complexity and can be solved easily. Solving the linearized ATC requires no system analysis function evaluation during the inner loop coordination, and so the associated cost is relatively small, especially for problems with expensive analyses. Also, the analyses in the decomposed elements can be executed concurrently. Also, the L_∞ norm is employed to maintain linearity of the consistency constraints. Since some of $\mathbf{c}_{ij}$ cannot be active unless strict consistency is satisfied, deviation errors ϵ_{ij} remain in the objective functions. Even if $\mathbf{c}_{ij}$ may cause computational inefficiency due to degeneracy when $\mathbf{w}_{ij}$ and $\mathbf{t}_{ij} - \mathbf{r}_{ij}$ are small, numerical results show that the effect is not substantial during the inner loop coordination with sufficiently large $\mathbf{w}_{ij}$.

Some notation used in previous SLP-filter algorithm formulations was modified here so that definitions are equivalent to those in [57]. For convergence of the proposed SLP-based ATC, both convergence proofs of SLP-filter algorithms (Eq.(2.32) and Eq.(3.2)) and ATC (Eq.(3.2) and Eq.(3.6)) need to hold. For the first part of the proof, the convergence proof of SLP-filter algorithm in [57] was extended to

problems with equality constraints and holds for the decomposed problems. Also, the second step of the proof (ATC convergence with L_∞ norms) was proven based on HOC strategy. The examples in Section 3.4 show that the proposed SLP-based ATC converges to the solution accurately.

Decomposition enables suspension strategy to be used in order to reduce the number of function evaluation taking advantage of the properties of weakly-couple elements. Even though the suspension criteria do not guarantee either reduced computational cost or global convergence, numerical experiments presented in Section 3.4 show 10 to 20% reduction in computational cost with the proper selection of parameters based on normalized computational costs depending on the balance of coupling strengths. Results must be compared further with other ATC relaxation methods that have shown better numerical efficiency and convergence, such as AL-AD [126] or TDQA [94].

The suspension strategy can be applied to other decomposition methods, such as collaborative optimization. Suspended elements are recognized as objects that do not need significant design changes in a hierarchical decomposition. Suspended elements in a non-hierarchical decomposition could be aspects or disciplines insensitive to system design changes. Promising results from the examples give a limited demonstration of the SLP-filter algorithms advantages. They warrant further investigation of the method applied to more complex design problems, including probabilistic optimization problems, the original inspiration for development of this method.

CHAPTER IV

SLP Coordination for Probabilistic ATC

4.1 Introduction

In this chapter, we employ SLP as an alternative coordination strategy to solve PATC problems. In the proposed algorithm, probabilistic constraints are approximated by equivalent deterministic linear constraints so that the uncertainty propagation in the linearized subproblem is obtained easily. The linking variables are represented only with means and standard deviations, and the consistency of random variables does not require significant computation in estimating and matching distributions. Further a subsystem suspension strategy, developed specially for an SLP-based ATC, is also applied to reduce computational cost by suspending the analyses of subsystems that do not need considerable redesign, based on the size of trust regions and the step size of target values. The effectiveness of the proposed SLP coordination strategy for PATC, or SLP-based PATC for short, is demonstrated by comparing results for several examples to those obtained from previously proposed solution strategies.

Summary of Assumptions

The convergence proof of SLP coordination strategy for deterministic ATC in

Chapter 3 requires the assumptions used for the SLP or ATC convergence proofs in [57, 106]. In addition to the assumptions for the deterministic formulation, the following assumptions are made for the PATC algorithm convergence.

- Exact or approximate normality of random variables: In this dissertation, uncertainty is represented by random variables whose distributions are normal or can be approximated to be normal.
- Independence of random variables from each other: Random design variables and random linking variables are assumed to be independent.
- Time independent (stationary) random variables: The probabilistic characteristics of random variables do not vary in time.
- Irreducibility: Randomness of design variables is inherent so that it cannot be eliminated by improving observation methods.

The chapter is organized as follows. In Section 4.2, a Probabilistic Linearized ATC (PLATC) subproblem is formulated and the method of updating standard deviations of linking variables is discussed. Section 4.3 explains briefly the suspension strategy for SLP-based PATC. Illustrative test examples are presented in Section 4.4, followed by conclusions in Section 4.5.

4.2 SLP-based Probabilistic Analytical Target Cascading

In SLP-based PATC, a PLATC subproblem is created from a nonlinear PATC problem and is solved using the "standard" ATC strategy. By solving PLATC successively, the algorithm converges to a solution of the original nonlinear PATC problem.

Similar to [28], probabilistic constraints are approximated with equivalent deterministic constraints by either FORM or SORM. In FORM/SORM [22, 73] standard deviations must be known. Therefore, the means of linking variables in this chapter are treated as optimization variables, while their standard deviations are estimated at every iteration. A PLATC formulation is derived in Section 4.2.1 while Section 4.2.2 includes a review on how the standard deviations were handled in the previous PATC literature and a discussion on the updating method for linking variables.

4.2.1 PLATC Subproblem Formulation

In Chan et al. [28], an LP subproblem is constructed from PAIO using either FORM or SORM. In the dissertation, FORM and SORM are judiciously applied to constraints based on the following criteria:

for a constraint $g'_m \equiv \Pr[g_m(\mathbf{X}) > 0] - p_{f,m} \leq 0$,

$$\text{if } g'_m < -\delta \quad \text{or} \quad E_m = \Phi(-\beta_m)\left|\left|\prod_p (1+\beta_m\kappa_p)^{-1/2} - 1\right|\right| \leq E^a, \qquad (4.1)$$

then FORM is applied,

$$\text{if } g'_m \geq -\delta \quad \text{and} \quad E_m = \Phi(-\beta_m)\left|\left|\prod_p (1+\beta_m\kappa_p)^{-1/2} - 1\right|\right| > E^a, \qquad (4.2)$$

then SORM is applied,

where δ is a small positive number that allows a buffer to g_m and Φ is the standard normal cumulative distribution function. In these criteria, E_m indicates an error between probability of failure estimated by FORM and SORM, and E^a is the tolerance of the error. Also, β_m and κ_p denote the reliability index and the pth principal curvature of g_m at MPP. The principal curvatures $\boldsymbol{\kappa}$ of g_m are calculated as the

eigenvalues of the matrix $\mathbf{A}$, expressed as:

$$\mathbf{A} = \frac{\mathbf{B}^{\mathrm{T}}\mathbf{D}\mathbf{B}}{||\nabla g_m(\mathbf{x}_{\mathrm{M}})||} \tag{4.3}$$

where $\mathbf{x}_{\mathrm{M}}$ is the MPP of g_m, $\mathbf{D}$ is the Hessian of the g_m at $\mathbf{x}_{\mathrm{M}}$, and $\mathbf{B}$ is a matrix orthogonal to $\mathbf{B_0}$, expressed as:

$$\mathbf{B_0} = \begin{bmatrix} I_{(n-1)\times(n-1)} & 0 \\ \frac{\partial g_m}{\partial x_1} \; \frac{\partial g_m}{\partial x_2} \; \cdots & \frac{\partial g_m}{\partial x_n} \end{bmatrix}. \tag{4.4}$$

In Eq.(4.2), the first criterion indicates the activity of the constraint, so called δ-activity, while the second criterion takes into account the curvature of g_m. Since δ-activity is easy to check, the curvature criterion is applied only if the constraint is δ-active.

In Chapter 3, an SLP coordination algorithm applied to ATC problems was discussed. Similar to the deterministic LATC, weighted L_∞ norms are used as the measure of inconsistency in order to maintain the linearity of subproblem formulations instead of quadratic penalty function terms. Therefore, the maximum deviations of consistency constraints, ϵ_{ij}, are combined with the objective function, expressed as:

$$\begin{aligned} \min \quad & ||\mathbf{w}_{ij} \circ (\boldsymbol{\mu}_{\mathbf{T}ij} - \boldsymbol{\mu}_{\mathbf{R}ij})||_2^2 \\ \Rightarrow & \begin{cases} \min \quad \epsilon_{ij} \\ \text{subject to} \quad -\boldsymbol{\epsilon}_{ij} \le \mathbf{w}_{ij} \circ (\boldsymbol{\mu}_{\mathrm{T}_{ij}} - \boldsymbol{\mu}_{\mathrm{R}_{ij}}) \le \boldsymbol{\epsilon}_{ij}, \end{cases} \end{aligned} \tag{4.5}$$

where $\boldsymbol{\epsilon}_{ij}$ is a column vector whose components are equal to ϵ_{ij}. Applying constraints approximated by FORM/SORM and infinity norms, the equivalent PLATC

subproblem at iteration l with trust region radius $\rho^l > 0$ can be expressed as:

$$
\begin{aligned}
\min \quad & \nabla f_{ij}^l(\boldsymbol{\mu}_{\bar{\mathbf{x}}_{ij}}^l)^T \bar{\mathbf{d}}_{ij}^l + \epsilon_{ij} + \sum_{k \in \mathcal{C}_{ij}} \epsilon_{(i+1)k} \\
\text{with respect to} \quad & \bar{\mathbf{d}}_{ij}^l, \epsilon_{ij}, \epsilon_{(i+1)1}, ..., \epsilon_{(i+1)n_{ij}} \\
\text{subject to} \quad & \nabla g_{ij,m}^l(\bar{\mathbf{x}}_{\mathrm{M}_{ij,m}}^l)^T \bar{\mathbf{d}}_{ij}^l + g_{ij,m}^l(\bar{\mathbf{x}}_{\mathrm{M}_{ij,m}}^l) \leq \mathbf{0} \quad \text{if } g_{ij,m} \text{ satisfies Eq.(4.1)}, \\
& \nabla g_{ij,m}^l(\bar{\mathbf{x}}_{\mathrm{S}_{ij,m}}^l)^T \bar{\mathbf{d}}_{ij}^l + g_{ij,m}^l(\bar{\mathbf{x}}_{\mathrm{S}_{ij,m}}^l) \leq \mathbf{0} \quad \text{if } g_{ij,m} \text{ satisfies Eq.(4.2)}, \\
& -\boldsymbol{\epsilon}_{ij} \leq \mathbf{w}_{ij} \circ (\boldsymbol{\mu}_{\mathbf{T}_{ij}} + \mathbf{d}_{\boldsymbol{\mu}_{\mathbf{T}_{\mathrm{ij}}}} - \boldsymbol{\mu}_{\mathbf{R}_{ij}} - \mathbf{d}_{\boldsymbol{\mu}_{\mathbf{R}_{\mathrm{ij}}}}) \leq \boldsymbol{\epsilon}_{ij}, \\
& -\boldsymbol{\epsilon}_{(i+1)k} \leq \{\mathbf{w} \circ (\boldsymbol{\mu}_{\mathbf{T}} + \boldsymbol{\mu}_{\mathbf{d_T}} - \boldsymbol{\mu}_{\mathbf{R}} - \boldsymbol{\mu}_{\mathbf{d_R}})\}_{(i+1)k} \leq \boldsymbol{\epsilon}_{(i+1)k}, \\
& ||\bar{\mathbf{d}}_{ij}^l||_\infty \leq \rho^l, \\
\text{where} \quad & \bar{\mathbf{x}}_{\mathrm{M}_{ij,m}}^l = \boldsymbol{\mu}_{\bar{\mathbf{x}}_{ij}}^l + \boldsymbol{\sigma}_{\bar{\mathbf{x}}_{ij}}^l \beta_{t,m} \frac{\nabla g_{ij,m}^l}{||\nabla g_{ij,m}^l||}, \\
& \bar{\mathbf{x}}_{\mathrm{S}_{ij,m}}^l = \boldsymbol{\mu}_{\bar{\mathbf{x}}_{ij}}^l + \boldsymbol{\sigma}_{\bar{\mathbf{x}}_{ij}}^l \beta_{\mathrm{S},m}^l \frac{\nabla g_{ij,m}^l}{||\nabla g_{ij,m}^l||} \\
& \boldsymbol{\mu}_{\mathbf{R}_{ij}}^l = \mathbf{a}_{ij}^l(\boldsymbol{\mu}_{\bar{\mathbf{x}}_{ij}}^l) + \nabla \mathbf{a}_{ij}^l(\boldsymbol{\mu}_{\bar{\mathbf{x}}_{ij}}^l)^T \bar{\mathbf{d}}_{ij}^l \\
& \bar{\mathbf{d}}_{ij}^l = [\mathbf{d}_{\boldsymbol{\mu}_{\mathbf{X}_{ij}}}^l, \mathbf{d}_{\boldsymbol{\mu}_{\mathbf{T}_{(i+1)k}}}^l], \quad \forall k \in \mathcal{C}_{ij}, \quad \forall j \in \mathcal{E}_i, \quad i = 1, ..., N,
\end{aligned}
\tag{4.6}
$$

where $\beta_{t,m}$ is the target reliability index for $g_{ij,m}$ while $\beta_{\mathrm{S},m}^l$ is obtained by solving

$$
\Phi(-\beta_{\mathrm{S},m}^l) \prod_p (1 + \beta_{\mathrm{S},m}^l \kappa_p^l)^{-1/2} - (1 - \alpha_m) = 0. \tag{4.7}
$$

Chan et al. [28] showed that the convergence proof of the SLP-filter algorithm can be extended for problems with probabilistic constraints. Similarly, we can replicate the convergence arguments for LATC presented in the previous chapter, which shows that the convergence proof of the SLP-filter algorithm can be extended to ATC formulations with consistency constraints under MFCQ [102].

4.2.2 Standard Deviation of Linking Variables

The linking variables can include shared design variables, coupling variables or both: coupling variables are analysis outputs from one element that are inputs to

its parent while shared design variables are design variables that are inputs to multiple elements. For shared variables, their standard deviations are also constant parameters in PATC because they are given in the original PAIO problem. The distributions of the coupling variables, however, are dependent on the design variables of elements and likely to be non-normal. As pointed out in the previous PATC publications, matching the whole distribution is impractical because the computational cost of coordination increases substantially with the dimension of linking variables. In order to address the issue, Kokkolaras et al. [84] matched the mean values of responses for consistency while their PDFs were estimated from its children elements using an technique base on Advanced Mean Value (AMV) method [136]. On the other hand, Liu et al. [100] had the first two moments matched. Based on their generalized formulations, higher moments can be included for higher accuracy even though matching higher order moments increases the dimension of linking variables. In order to solve PATC with respect to the standard deviations of random variables, Monte Carlo Simulation (MCS) with 100,000 samples was applied, which made the algorithm computationally expensive.

In this dissertation, a scheme similar to [84] is used for standard deviations. Since PLATC consists of linear functions, the resulting distributions of linking variables are normal, if the distributions of design variables are assumed to be normal. Thus, terms of order higher than means and standard deviations are not needed to define the distributions. Moreover, as mentioned earlier, standard deviations are estimated and updated at every SLP iteration because FORM/SORM are used.

The algorithm flow is shown in Figure 4.1. In Step 1, PLATC is created from the original PATC in Eq.(4.6). In Step 2, the generated PLATC is solved by a

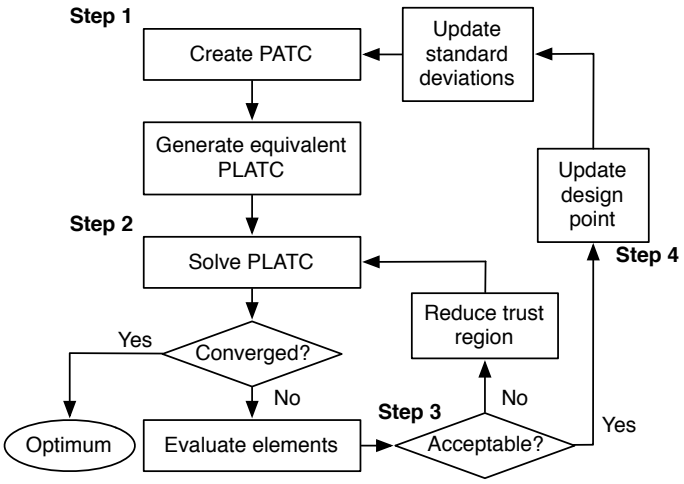

Figure 4.1: SLP-based PATC algorithm flow

"standard" ATC strategy. Note that during the inner coordination, no function evaluation is needed. Once a solution is obtained, the convergence condition is checked. If the solution is not optimal, the elements are evaluated to obtain the objectives and constraints. Since the system is decomposed, the evaluation can be executed separately and concurrently. In Step 3, the algorithm determines if the solution is acceptable for the next design point based on the evaluated objectives and constraints. Here, the same criteria used in the previous chapter are applied,

expressed as:

$$\text{if } \eta^l \le \beta^L \eta_i \quad \text{or} \quad f_e^l \le (f_e)_i - \gamma^L \eta_i, \quad \forall i \in \mathcal{F} \tag{4.8}$$

$$\text{if } \Delta f_e^l \ge \sigma^L \Delta l_e^l \text{ and } \Delta l_e^l \ge \delta^L (\eta^l)^2, \text{ then f-type iteration;} \tag{4.9}$$

$$\text{else, if } \Delta l_e^l < \delta^L (\eta^l)^2, \text{ then } \eta\text{-type iteration;} \tag{4.10}$$

else unacceptable;

else unacceptable;

$$\begin{aligned} \text{where} \quad & \eta^l(\boldsymbol{\mu}^l_{\bar{\mathbf{X}}_{11}}, ..., \boldsymbol{\mu}^l_{\bar{\mathbf{X}}_{NM}}) = ||\mathbf{g}'^l(\boldsymbol{\mu}^l_{\bar{\mathbf{X}}})^+||_1 + ||\boldsymbol{\mu}^l_{\mathbf{T}} + \mathbf{d}^l_{\boldsymbol{\mu}_{\mathbf{T}}} - \boldsymbol{\mu}^l_{\mathbf{R}} - \mathbf{d}^l_{\boldsymbol{\mu}_{\mathbf{R}}}||_1, \\ & \Delta l_e^l = \sum_{i=1}^{N} \sum_{j \in \mathcal{E}_i} \nabla f_{ij}^{l\,T} \bar{\mathbf{d}}_{ij}^l, \\ & \Delta f_e^l = \sum_{i=1}^{N} \sum_{j \in \mathcal{E}_i} f_{ij}^l(\boldsymbol{\mu}^l_{\bar{\mathbf{X}}_{ij}}) - \sum_{i=1}^{N} \sum_{j \in \mathcal{E}_i} f_{ij}^l(\boldsymbol{\mu}^l_{\bar{\mathbf{X}}_{ij}} + \bar{\mathbf{d}}_{ij}^l), \end{aligned} \tag{4.11}$$

and $1 \sim \beta^L > \sigma^L > \gamma^L \sim 0$, $\delta^L \sim 0$ are positive parameters, defined in SLP-filter algorithms [57], and $\mathcal{F}$ denotes the current filter. The definition and details of a filter algorithm are well reviewed in [58]. Eq.(4.8) determines if the current solution is an acceptable one to the filter (meaning the solution is an improved design over current filter entries). If the solution is acceptable to the filter and satisfies Eq.(4.9), it is called an f-type iteration (improving f_e with a possible increase in η). If the solution is acceptable to the filter and satisfies Eq.(4.10), it is called an η-type iteration (reducing η with a possible increase in f_e). Otherwise, the solution is rejected, the trust region radius is reduced by half and PLATC is solved again. If the solution is accepted as either an f-type or an η-type iteration, the solution is used as the incumbent point at the next iteration (Step 4). If the solution is an η-type iteration, the solution is added to the filter and the entries that are dominated by the solution are eliminated from the filter. Then the standard deviations of responses are updated. To estimate the standard deviations, any method can be used, including a linear approximation,

an AMV-based technique and MCS. Linear approximation is closest to the spirit of this chapter and less expensive, while the other methods provide more accurate estimation. For more details and convergence proofs, see [28, 57].

4.3 Suspension Strategy for SLP-based PATC

In Chapter 3, a suspension strategy for SLP-based ATC was introduced in order to reduce the number of function evaluations by suspending elements from redesign (or evaluation), if changes in the targets for an element are sufficiently small [8, 53, 76]. For the suspension strategy, Step 2 in Figure 4.1 needs to be modified with several inner steps, shown in Figure 4.2. Once PLATC is generated, Eq.(4.6) is solved using a standard ATC strategy to obtain $\bar{\mathbf{d}}_{ij}^{l}$ in Step 2.A. If the solution is not optimal, Step 2.B selects the set of elements that can be suspended based on suspension criteria defined by users. In this chapter, we simply compare the step sizes of targets $\mathbf{d}_{\boldsymbol{\mu}_\mathbf{T}}^{l}$. If a target to a child m satisfies

$$||\mathbf{d}_{\boldsymbol{\mu}_{\mathbf{T}_{(\mathrm{i+1})\mathrm{m}}}}^{l}|| < \zeta_t \sum_{k \in \mathcal{C}_{ij}} \frac{||\mathbf{d}_{\boldsymbol{\mu}_{\mathbf{T}_{(i+1)k}}}^{l}||}{NC_{ij}}, \tag{4.12}$$

then the elements in the corresponding branch are selected for suspension. The parameter $\zeta_t << 1$ is chosen based on the designers experience and NC_{ij} is the number of children of element j at level i. In Step 2.C, PLATC is solved again with only the unsuspended elements by setting the responses of the suspended elements to zero. With the solution, the predicted reduction in f_e with suspension $\Delta l_e^{\mathrm{sus}}$ is obtained. If $\Delta l_e^{\mathrm{sus}} \geq \zeta_f \Delta l_e$, the suspension is assumed to be valid. The parameter $\zeta_f < 1$ is also chosen based on the designer's experience. Otherwise, the suspension is declared to be inadequate and some of the suspended elements must be reactivated if more than two elements are selected for suspension. After reactivation, PLATC

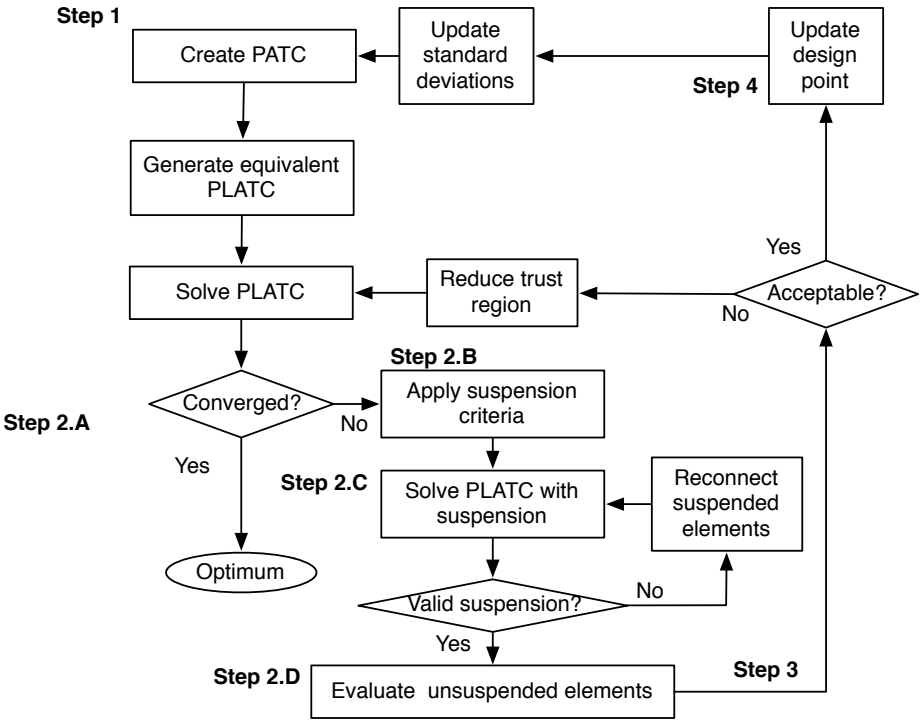

Figure 4.2: SLP-based PATC algorithm flow with suspension strategy

is solved again until suspension is valid or all elements are active. In Step 2.D, the functions in the unsuspended elements are evaluated. For suspended elements, the values at the previous iteration are used.

4.4 Numerical Results

This section provides three test examples to illustrate the proposed algorithm. All examples have three elements: one at the top level and two at the bottom level. One child element is more weakly coupled to the top level element than the other since the proposed suspension strategy is more effective on problems whose elements have significantly different coupling strengths.

The examples are solved by SLP-based PATC with and without suspension strategy, denoted as *PLATC* and *PLATC-SS*, respectively. The results are compared to those obtained from PATC with AMV-based techniques and PAIO with MCS

, denoted as *PATC-AMV* and *PAIO-MCS*. Quadratic penalty functions are used for*PATC-AMV* as relaxation functions. The weights on L_∞ norms and quadratic penalty functions are initialized to 1 at every SLP iteration and doubled at every ATC iteration. Thus, if the weighting update method is used, the accuracy and local convergence of *PLATC*, *PLATC-SS* and *PATC-AMV* could be improved from those obtained in this section[105]. The method should be more effective on *PATC-AMV* than the others because no function evaluations are made during the inner coordination of *PLATC* and *PLATC-SS*. The number of samples for MCS is 100,000, and the target probability of failure p_f^t is 0.13% for all probabilistic constraints. All random design variables are assumed to be normal with constant standard deviations.

4.4.1 Example 1: Modified Hock and Schittkowski problem 34 [72]

The first example is the modified Hock and Schittkowski problem 34, presented in the previous chapter. The PAIO problem is

$$\begin{aligned}
\min \quad & f = -x_1 x_4 \\
\text{with respect to} \quad & \mathbf{x} = \{x_1, \mu_{X_2}, \mu_{X_3}, x_4, \mu_{X_5}, \mu_{X_6}\}^T \\
\text{subject to} \quad & \Pr[g_i > 0] \le p_f^t, i = 1, ...4 \\
\text{where} \quad & g_1 \equiv \exp(x_1) - X_2 X_5 \le 0, \quad g_2 \equiv \exp(X_2) - X_3 \le 0, \\
& g_3 \equiv \log(5x_4^2) - X_5 \le 0, \quad g_4 \equiv X_5^2 - 10X_6 \le 0, \\
& \{0, 0.6, 0.6, 0.01, 0.6, 0.6\} \le \mathbf{x}^T \le \{100, 99.4, 9.4, 100, 99.4, 4.4\}
\end{aligned} \tag{4.13}$$

where $\sigma_{X_2} = \sigma_{X_3} = \sigma_{X_5} = \sigma_{X_6} = 0.2$. The structure of the decomposed system is provided in the previous chapter, as illustrated in Figure 3.7. The initial point is set to the feasible point that is closest to the deterministic optimal point, $\{2.79, 2.30, 10.00, 15.35, 7.07, 5.00\}$. Parameters for the suspension strategy are set to $\zeta_t = 0.1$ and $\zeta_f = 0.8$; the initial trust region is set to 20.

Table 4.1: Optimal solutions and number of redesigns for Example 1

	$\mathbf{x}^*$ $\{x_1, \mu_{X_2}, \mu_{X_3}, x_4, \mu_{X_5}, \mu_{X_6}\}$				f_e^*
PLATC	$\{1.80, 1.64, 9.40, 6.24, 5.87, 4.40\}$				-11.22
PLATC-SS	$\{1.80, 1.64, 9.40, 6.24, 5.87, 4.40\}$				-11.22
PATC-AMV	$\{1.80, 1.64, 9.40, 6.25, 5.87, 4.40\}$				-11.25
PAIO-MCS	$\{1.75, 1.64, 9.40, 6.24, 5.87, 4.40\}$				-10.92
	number of redesigns				consistency
	O_{11}	O_{22}	O_{23}	total	error
PLATC	561	478	368	1407	0.36×10^{-12}
PLATC-SS	561	418	204	1183	0.67×10^{-12}
PATC-AMV	8653	910	1299	10862	2.20×10^{-4}
PAIO-MCS	$4879 \times 100,000$				0

Table 4.1 summarizes the results obtained from *PLATC*, *PLATC-SS*, *PLATC-AMV*, *PAIO-MCS*. All algorithms find the solution with all constraints active because the problem is monotonic for all design variables even in the probabilistic formulation and SLP algorithms are very effective [112]. Due to the simplicity of reliability analysis in the SLP-based algorithms, the numbers of redesigns for *PLATC*, *PLATC-SS* are significantly smaller than the others. The FORM/SORM approximation is sufficient based on the reliability analysis results shown in Table 4.2. The small difference in x_1 from that of *PAIO-MCS* results from the error in g_1. As noted, strong monotonicity helps convergence of the SLP algorithms. Moreover, the suspension strategy reduces the number of function evaluations of the lower level elements.

Table 4.2: Reliability analysis results for Example 1 (1,000,000 samples for MCS)

	constraint activity (A: active)				MCS p_f (%)			
	g_1	g_2	g_3	g_4	g_1	g_2	g_3	g_4
PLATC	A	A	A	A	0.14	0.14	0.13	0.13
PLATC-SS	A	A	A	A	0.14	0.14	0.13	0.13
PATC-AMV	A	A	A	A	0.14	0.13	0.14	0.13

4.4.2 Example 2: Geometric Programming Problem

The second example is a geometric programing problem, formulated in a probabilistic form in [100]. The deterministic formulations are provided and solved in previous ATC literature [80, 126]. The PAIO problem can be expressed as:

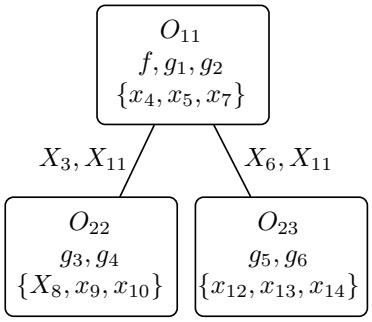

Figure 4.3: Geometric programming problem

$$
\begin{aligned}
\min \quad & \mathrm{E}[f] = \mu_{X_1}^2 + \mu_{X_2}^2 \\
\text{with respect to} \quad & \mathbf{x} = \{x_4, x_5, x_7, \mu_{X_8}, x_9, x_{10}, \mu_{X_{11}}, x_{12}, x_{13}, x_{14}\}^T \\
\text{subject to} \quad & \Pr[g_i > 0] \leq p_f^t, \quad i = 1, ..., 6 \\
\text{where} \quad & g_1 \equiv (X_3^{-2} + x_4^2)x_5^{-2} - 1, \quad g_2 \equiv (x_5^2 + X_6^{-2})x_7^{-2} - 1, \\
& g_3 \equiv (X_8^2 + x_9^2)X_{11}^{-2} - 1, \quad g_4 \equiv (X_8^{-2} + x_{10}^2)X_{11}^{-2} - 1, \\
& g_5 \equiv (X_{11}^2 + x_{12}^{-2})x_{13}^{-2} - 1, \quad g_6 \equiv (X_{11}^2 + x_{12}^2)x_{14}^{-2} - 1, \\
& X_1 = (X_3^2 + x_4^{-2} + x_5^2)^{1/2}, \quad X_2 = (x_5^2 + X_6^2 + x_7^2)^{1/2}, \\
& X_3 = (X_8^2 + x_9^{-2} + x_{10}^{-2} + {X_{11}}^2)^{1/2}, \\
& X_6 = (X_{11}^2 + x_{12}^2 + x_{13}^2 + x_{14}^2)^{1/2},
\end{aligned}
\tag{4.14}
$$

where $\sigma_{X_8} = \sigma_{X_11} = 0.1$. The structure of the decomposed problem is provided in [100], as illustrated in Figure 4.3. The initial point is set to the deterministic optimal point, $\mathbf{x}^* = \{0.76, 0.87, 0.94, 0.97, 0.87, 0.80, 1.30, 0.84, 1.76, 1.55\}$. Parameters for the suspension strategy are set to $\zeta_t = 0.1$ and $\zeta_f = 0.8$; the initial trust region is set to 0.01.

Table 4.3: Optimal solutions and number of redesigns for Example 2

	$\mathbf{x}^*$ $\left\{ x_4, x_5, x_7, \mu_{X_8}, x_9, x_{10}, \mu_{X_{11}}, x_{12}, x_{13}, x_{14} \right\}$	f_e^*	number of redesigns			
			O_{11}	O_{22}	O_{23}	total
PLATC	$\left\{ \begin{matrix} 0.74, 0.85, 0.89, 1.04, 0.80, \\ 0.86, 1.70, 0.85, 2.32, 2.17 \end{matrix} \right\}$	24.64	900	774	545	2219
PLATC-SS	$\left\{ \begin{matrix} 0.74, 0.85, 0.89, 1.04, 0.80, \\ 0.86, 1.70, 0.85, 2.32, 2.17 \end{matrix} \right\}$	24.64	900	774	501	2175
PATC-AMV	$\left\{ \begin{matrix} 0.76, 0.85, 0.89, 1.04, 0.65, \\ 0.68, 1.61, 0.84, 2.24, 2.08 \end{matrix} \right\}$	24.99	44187	57597	17760	119544
PAIO-MCS	$\left\{ \begin{matrix} 0.76, 0.85, 0.89, 1.12, 0.63, \\ 0.94, 1.67, 0.89, 2.28, 2.18 \end{matrix} \right\}$	25.22	5101×100,000			
	consistency error		$\{\sigma_{X_3}, \sigma_{X_6}\}$			
PLATC	1.85×10^{-11}		$\{0.080, 0.046\}$			
PLATC-SS	5.31×10^{-11}		$\{0.080, 0.046\}$			
PATC-AMV	1.95×10^{-3}		$\{0.066, 0.045\}$			
PAIO-MCS	0		$\{0.073, 0.046\}$			

Table 4.3 summarizes the results obtained from the four algorithms. All solutions are nearly identical with all constraints active. Sequential linearization reduces the computational cost in reliability analysis considerably without sacrificing much accuracy. Because the coupling strength of the problem is well-balanced between the parent and two children, *PLATC-SS* is not as effective as in the other examples. The differences in the solutions result mainly from the errors in estimating σ_{X_3} and reliability analysis of g_3 and g_4, as shown in Table 4.4. Note that the constraints are located in the child element, linked through X_3 and the estimated σ_{X_3} by MCS at the *PLATC-SS* solution is 0.075. Thus, accurate estimation of σ_{X_3} may provide more accurate results even though it may increase the computational cost.

4.4.3 Example 3: Allison's Structural Optimization Problem

This structural optimization problem was presented by Allison et al. [7]. Similar to the previous chapter, the element at the second level (the middle bar) is located

Table 4.4: Reliability analysis results for Example 2 (1,000,000 samples for MCS)

	constraint activity (A: active)					
	g_1	g_2	g_3	g_4	g_5	g_6
PLATC	A	A	A	A	A	A
PLATC-SS	A	A	A	A	A	A
PATC-AMV	A	A	A	A	A	A
	MCS p_f (%)					
	g_1	g_2	g_3	g_4	g_5	g_6
PLATC	0.09	0.05	0.14	0.17	0.13	0.13
PLATC-SS	0.09	0.05	0.14	0.17	0.13	0.13
PATC-AMV	0.08	0.05	0.15	0.16	0.13	0.13

to the top level and the other two are located at the bottom level, shown in Figure 3.9. The coupling strength between the second and third rod is strengthed. The original PAIO problem is

$$
\begin{aligned}
\min \quad & \sum_{i=1}^{3} \tfrac{\pi}{4}\mu_{D_i}^2 l\rho + \sum_{j=1}^{2} \tfrac{\pi}{4}\mu_{D_{r,j}}^2 l\rho \\
\text{with respect to} \quad & \mathbf{x} = \{\mu_{D_1}, \mu_{D_2}, \mu_{D_3}, \mu_{D_{r1}}, \mu_{D_{r2}}\}^T \\
\text{subject to} \quad & \Pr[g_{1,i} \equiv \sigma_{b,i} - \bar{\sigma} > 0] \le p_f^t \quad i = 1,2,3 \\
& \Pr[g_{2,j} \equiv \sigma_{a,j} - \bar{\sigma} > 0] \le p_f^t \quad j = 1,2 \\
& \Pr[g_{3,i} \equiv (F_i - F_{i+1}) - \bar{F}_{t,i} > 0] \le p_f^t \quad i = 1,2,3 \\
& \Pr[g_4 = f_1 - \bar{f}_1 > 0] \le p_f^t \\
& h_{1,j} \equiv f_j - f_{j+1} - f_{r,j} = 0 \quad j = 1,2 \\
\text{where} \quad & \sigma_{b,i} = \tfrac{32l(F_i - F_{i+1})}{\pi d_i^3}, \quad f_i = \tfrac{64l^3(F_i - F_{i+1})}{3\pi E_i d_i^4}, \quad i = 1,2,3; \\
& \sigma_{a,j} = \tfrac{4F_{j+1}}{\pi d_{r,j}^2}, \quad f_{r,j} = \tfrac{4F_{j+1}l}{\pi E_{r,j} d_{r,j}^2} \quad j = 1,2,
\end{aligned}
\tag{4.15}
$$

where constraint limits for stress ($\bar{\sigma}$), transmitted force ($\bar{F}_t$) and vertical deflection of beam 1 (f_1) are set to $127(10^6)$N/m^2, 400N and 27mm, respectively. The length of beams and rods l and the density of the material ρ are fixed to be 1m and 2700kg/m^3, respectively; 1000N is vertically applied at the end of beam 1 ($F_1 = 1000$N). In order to apply different coupling strengths, the Young's moduli of the beams and rods are

set differently: $E_1 = E_2 = E_{r,1} = 70$GPa, $E_3 = 700$GPa, $E_{r,2} = 7$GPa. Therefore, the coupling strength between beams 2 and 3 becomes significantly stronger than that between beams 1 and 2. Since SLP-based algorithms are more effective when problems are well-scaled, the diameters of beams and rods are multiplied by 1000 and 10000, respectively. The scaled lower and upper bounds and the standard deviations for all design variables are set to 2.5, 58.5 and 0.5. The scaled initial point is the deterministic optimal point, $\{34.6, 34.9, 29.4, 46, 28\}$. Parameters for the suspension strategy are set to $\zeta_t = 0.2$ and $\zeta_f = 0.8$; the initial trust region is set to 0.01.

Table 4.5: Optimal solutions and number of redesigns for Example 3

	$\mathbf{x}^*$ (scaled)	f_e^*	number of redesigns			
			O_{11}	O_{22}	O_{23}	total
PLATC	$\{35.44, 36.69, 31.69, 27.67, 20.00\}$	7.67	2262	2156	1016	5434
PLATC-SS	$\{35.44, 36.69, 31.69, 27.67, 20.00\}$	7.67	2089	1597	929	4615
PATC-AMV	$\{35.92, 35.60, 32.48, 27.44, 20.77\}$	7.69	28126	45732	4850	78708
PAIO-MCS	$\{35.39, 35.03, 32.30, 27.95, 19.98\}$	7.50	$1493 \times 100,000$			
	consistency error		$\{\sigma_{F_2}, \sigma_{F_3}, \sigma_{f_2}, \sigma_{f_3}\}$			
PLATC	1.31×10^{-7}		$\{14.22, 12.87, 0.56, 0.22\}$			
PLATC-SS	1.54×10^{-7}		$\{14.22, 12.87, 0.56, 0.22\}$			
PATC-AMV	1.55×10^{-3}		$\{14.36, 13.13, 0.59, 0.22\}$			
PAIO-MCS	0		$\{14.63, 13.50, 0.60, 0.21\}$			

Table 4.5 summarizes the results obtained from the four algorithms while Table 4.6 provides the reliability analysis results compared by MCS with 1,000,000 samples. All algorithms converge to nearly identical solutions with similar constraint activities. Based on the results, it can be concluded that FORM/SORM can provide sufficiently accurate approximation for MDO under uncertainty and the SLP-based PATC algorithm has an advantage over PATC with AMV-based techniques and PAIO with MCS due to the simplicity of uncertainty propagation. Because the coupling strength between O_{11} and O_{22} is sufficiently weaker than the other, the suspension

strategy reduces the number of function evaluations without sacrificing accuracy.

Table 4.6: Reliability analysis results for Example 3 (1,000,000 samples for MCS)

	constraint activity (A: active, I: inactive)			
	$g_{1,i}$ $(i=1,2,3)$	$g_{2,j}$ $(j=1,2)$	$g_{3,i}$ $(i=1,2,3)$	g_4
PLATC	{I,I,A}	{A, I}	{I, I, A}	A
PLATC-SS	{I,I,A}	{A, I}	{I, I, A}	A
PATC-AMV	{I,I,A}	{A, I}	{I, I, A}	I
	MCS p_f (%)			
	$g_{1,i}$ $(i=1,2,3)$	$g_{2,j}$ $(j=1,2)$	$g_{3,i}$ $(i=1,2,3)$	g_4
PLATC	$\{0, 0, 0.06\}$	$\{0.15, 0\}$	$\{0, 0, 0.00\}$	0.00
PLATC-SS	$\{0, 0, 0.06\}$	$\{0.15, 0\}$	$\{0, 0, 0.00\}$	0.00
PATC-AMV	$\{0, 0, 0.04\}$	$\{0.10, 0\}$	$\{0.00, 0, 0.08\}$	0

4.5 Concluding Remarks

The SLP coordination strategy for ATC developed earlier for deterministic formulations was shown to be effective also for PATC. The SLP-based PATC formulation is fundamentally the same as the deterministic formulation except for the constraints. Probabilistic constraints in the original PAIO problem are translated into equivalent deterministic linear constraints using FORM/SORM. Thus, the entire treatment of the problems in SLP-based ATC can be applied to SLP-based PATC analogously.

Sequential linearization can be effective for probabilistic formulations because the uncertainty propagation of normal distributions can be obtained easily. The linearity can be more helpful for probabilistic MDO because random linking variables can be represented with only means and standard deviations. In nonlinear PATC, the computational cost of estimating and matching the distributions of linking variables is a critical issue in past PATC work because the distributions are typically non-normal. On the other hand, SLP-based PATC, containing only linear functions in

its equivalent LATC subproblems (Eq. (4.6)), requires only means and standard deviations to represent the random variables that can be efficiently estimated and matched. For estimation of standard deviations, linear approximation was used in this chapter even though other methods, including AMV-based techniques and MCS, can be applied when more accurate estimation is needed. Because FORM/SORM require standard deviations to be known, the linking variables include only means while the standard deviations for coupling variables are updated at the current design point for every iteration.

The examples in Section 4.4 show that the proposed SLP-based PATC converges to the solution with significantly fewer redesigns than *PATC-AMV* and *PAIO-MCS*. Based on the results, the solution accuracy depends more on the accuracy in the estimation of linking variables than that in FORM/SORM approximation. Thus, more accurate estimation methods, such as AMV-based techniques, might improve the accuracy. The "standard" ATC strategy used involved quadratic penalty functions. For fair comparison, SLP-based PATC must be compared to PATC with other penalty functions that have shown much better numerical efficiency and convergence, such as augmented Lagrangian functions [126]. The suspension strategy reduces the number of redesigns considerably for problems with unbalanced coupling strengths. Since the current criteria are sensitive to problem formulation, however, further investigation of robust suspension criteria is required for better convergence and computational efficiency.

CHAPTER V

Optimal Design of Hybrid Electric Fuel Cell Vehicles under Uncertainty

5.1 Introduction

Automotive use of fuel cells has received increased attention as a viable alternative energy source for automobiles due to clean and efficient power generation. In recent decades, many manufacturers and energy departments of many countries have supported research and development of fuel cells. In the automotive industry, a number of prototype fuel cell vehicles have been built since Daimler Benz launched the first prototype fuel cell vehicle, NECAR 1, in 1994. Toyota's FCHV, Nissan's X-Trail FCV, Honda's FCX, GM's HydroGen 3 car, Ford's Focus FCV-hybrid and Hyundai's Tuscon are prototype vehicles, recently developed using fuel cell technologies. Among various fuel cell technologies, Polymer Electrolyte Membrane (PEM) fuel cells are currently considered the most suitable for vehicular applications because of their mobility and high power density [87]. Nevertheless, several issues still exist that must be addressed in order to assess and improve viability of fuel cell vehicles, *e.g.*, whether to use high or low pressure fuel cells, or whether to consider hybrid propulsion configurations (*i.e.*, include additional power sources in the powertrain). Several fuel cell vehicle concepts and fuel cell system designs have been proposed and

studied in terms of safety, robust operation, fuel economy, and vehicle performance [62, 64, 65, 82].

In our previous work, a model-based vehicle design methodology was presented using a quasi-static fuel cell model, which can be used to design both a vehicle and a fuel cell system [67]. Even though the model achieved sufficient fidelity and efficiency for design studies, the lack of cost, weight and packaging consideration resulted in a relatively large fuel cell system for market acceptance. Also, the problem was solved by an AIO method where the vehicle and fuel cell systems were considered as an integrated system. As explained earlier, however, the AIO method may not be applicable if problems are complex or the cost of analysis functions at each optimization iteration are computationally expensive. In order to demonstrate the effectiveness of the proposed coordination strategies on complex problems, in this chapter we develop a comprehensive hybrid electric fuel cell vehicle (HEFCV) design model that takes into account profit, cost and market demand issues. Also, a 1-D Li-ion battery model, developed in [47, 61], is included to optimize a battery pack as well. Figure 5.1 illustrates the hierarchical decomposition of the HEFCV design problem. Blocks represent subsystems in the problem while the variables between them denote the linking variables. Finally, some design variables are chosen as random variables to investigate the effect of uncertainties in engineering design and customer behavior on the overall enterprise decisions.

The chapter is organized as follows. Section 5.2 explains models for the subsystems comprising the HEFCV system, namely, models for enterprise decisions, powertrain, fuel cell and battery. In Section 5.3, the results obtained from the proposed coordination strategies are provided, followed by conclusions in Section 5.4.

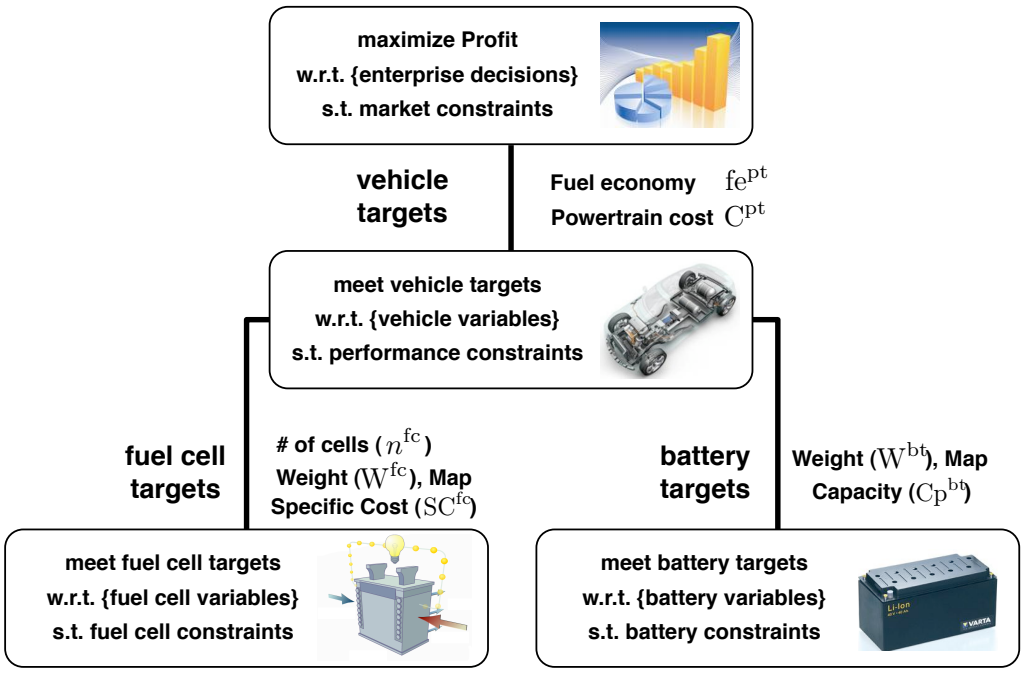

Figure 5.1: Hybrid electric fuel cell vehicles design problem with enterprise decision model

5.2 Hybrid Electric Fuel Cell Vehicle Design Model

5.2.1 Fuel Cell System Model

In order to analyze the behavior of fuel cell vehicles, models must be developed for subsystems, such as fuel cell, battery, and motor. The critical aspect of fuel cell system modeling is the Membrane-Electrode Assembly (MEA) model, which describes mathematically the entire physical environment of the electrochemical reactions; the transport phenomena of gases (hydrogen, oxygen, vapor, etc.), water, protons, and current; and the relationships among fuel cell voltage, current, temperature, material (electrode, catalyst and membrane) properties, and transport parameters. MEA modeling has been accomplished by analyzing physical effects of reactant gases [17, 119], performing experiments on actual stacks [123], or integrating the physical and experimental models [9]. Many publications on MEA models have con-

centrated on analyzing the water transport as well as the gas diffusion [12, 16, 23]. Heat transfer and thermodynamics were included to predict the temperature and humidity profiles in both transient and steady-state conditions [10, 132]. Computational fluid dynamics have been used extensively to analyze air and water transport behavior of fuel cell systems [131]. Unlike the relatively wide availability of MEA models, only a few publications are available on fuel cell system modeling. Pukrushpan et al. [116] applied reactant flow dynamics in order to estimate the net power output as a function of reactant partial pressures and the power losses in flow devices. Using MEA and fuel cell system models, optimization studies have been conducted to minimize the weighted sum of the inverse of functional performance and product cost [139] and to maximize power density by adjusting proper operating conditions [103]. The design objectives in all of the aforementioned papers do not reflect the requirements of the "supersystems" in which the designed fuel cell is used. In our previous study, a quasi-static fuel cell model was developed to take into account of the requirements of the "supersystem" [67].

5.2.1.1 Quasi-static Fuel Cell System Model

The quasi-static fuel cell system model is based on the transient fuel cell model developed by Pukrushpan et al. [116]. This model generates a static performance map that represents the maximum power for a certain range of fuel consumption with given control constraints. The power output from a fuel cell system $P_{\text{net}}^{\text{fc}}$ can be determined as the difference between the power generated from a fuel cell stack $P_{\text{st}}^{\text{fc}}$ and the power consumed by auxiliary components $P_{\text{con}}^{\text{fc}}$, expressed as follows:

$$P_{\text{net}}^{\text{fc}} = P_{\text{st}}^{\text{fc}} - P_{\text{con}}^{\text{fc}} = n^{\text{fc}} I_{\text{st}}^{\text{fc}} v_{\text{cl}}^{\text{fc}} - P_{\text{con}}^{\text{fc}}, \tag{5.1}$$

where n^{fc}, $I_{\text{st}}^{\text{fc}}$ and $v_{\text{cl}}^{\text{fc}}$ are the number of cells, the stack current and cell voltage of a fuel cell system. If the composition and structure of the cells are determined, then the cell voltage is a function of stack current density and reactant flow properties, including partial pressures, humidity, and temperature. The properties are governed by reactant suppliers consisting of four flow subsystems (shown in Figure 5.2): (i) hydrogen supply subsystem, (ii) air supply subsystem, (iii) cooling subsystem, and (iv) humidifying subsystem.This dissertation focuses on high pressure fuel cell systems with a compressor because most of the vehicular application prototypes are developed using high pressure fuel cells due to their higher power density.

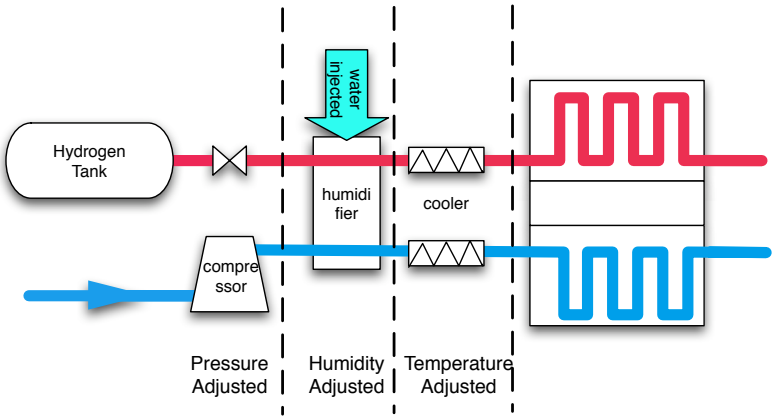

Figure 5.2: Reactant supply subsystems (modified from [116])

We assume that the properties of the inlet reactant flow, except for the partial pressures, can be controlled perfectly without transient irregularity. Additionally, the pressure at the anode is also assumed to be regulated instantly as a function of cathode pressure. Ambient air is assumed to be constant. The assumed properties are given in Table 5.1. Under these assumptions, the cell voltage can be reduced to

Table 5.1: Thermodynamical parameters used in the model

Parameter	Value
Ambient Temperature T_{amb} (Kelvin)	298
Stack Temperature T_{st} (Kelvin)	353
Ambient pressure p_{amb} (bar)	1
Ambient Relative Humidity	0.5
Relative Humidity of Cathode Inlet Flow	0.8
Anode Relative Humidity	1

a function of current density and oxygen partial pressure $p_{\text{O}_2,\text{ca}}$, expressed as follows:

$$v_{\text{cl}}^{\text{fc}} = v_{\text{cl}}^{\text{fc}}(p_{\text{O}_2,\text{ca}}, I_{\text{st}}^{\text{fc}}) = E^{\text{fc}} - v_{\text{act}} - v_{\text{ohm}} - v_{\text{conc}}, \tag{5.2}$$

where E^{fc} is the fuel cell open circuit voltage, and v_{act}, v_{ohm}, and v_{conc} are overvoltages due to the activation loss, ohmic loss, and concentration loss, respectively (details can be found in [116]). The overvoltage due to the fuel crossover and internal currents is neglected because the loss is relatively small in PEM fuel cells. Since the oxygen partial pressure is controlled by the output pressure of the compressor, the performance of the fuel cell is governed by the compressor input, which is determined as a function of the stack current by feed-forward control. Thus, the designed power output of the fuel cell can be obtained by applying a proper feed-forward control on the compressor command voltage [116]. In this dissertation, the feed-forward controller is designed to meet the target values of oxygen excess ratio $\lambda(I_{\text{st}}^{\text{fc}})$. Thus, the stack power can be simplified as a function of stack current and oxygen excess ratio.

Given ambient air properties, the air pressure and mass flow rate of the compressor outlet can be calculated from the mass conservation principle and thermodynamic and psychrometric gas properties under a quasi-static assumption. Figure 5.3 illustrates reactant flows under steady-state conditions. As the stack current $I_{\text{st}}^{\text{fc}}$ is drawn from the fuel cell, the rates of hydrogen and oxygen consumed in the reaction can

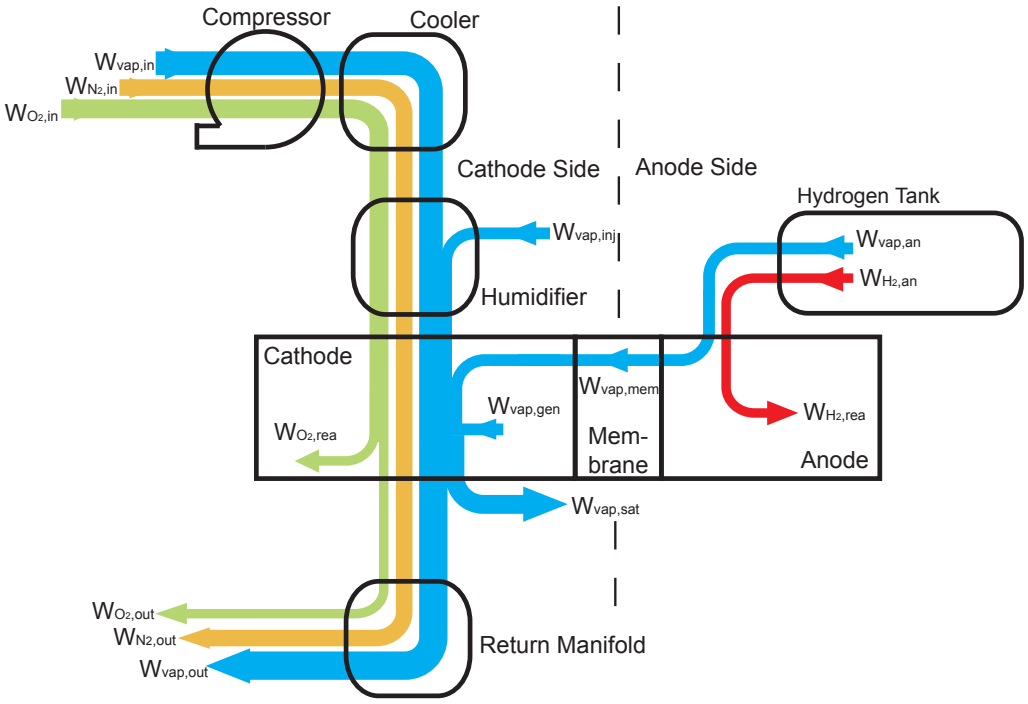

Figure 5.3: Diagram of reactant flows in a PEM fuel cell

be calculated as

$$W_{\mathrm{H_2,rea}} = M_{\mathrm{H_2}} \frac{n^{\mathrm{fc}} I_{\mathrm{st}}^{\mathrm{fc}}}{2F} \tag{5.3}$$

$$W_{\mathrm{O_2,rea}} = M_{\mathrm{O_2}} \frac{n^{\mathrm{fc}} I_{\mathrm{st}}^{\mathrm{fc}}}{4F}, \tag{5.4}$$

where $W_{\mathrm{H_2,rea}}$ and $W_{\mathrm{O_2,rea}}$, $M_{\mathrm{H_2}}$ and $M_{\mathrm{O_2}}$, and F are the rates of reacted hydrogen and oxygen, the molar masses of hydrogen and oxygen, and the Faraday constant ($= 96485$ C/mol), respectively. At steady state, since the oxygen is directly supplied from the ambient and the transient manifold filling effect is ignored, the rate of oxygen supplied to the cathode equals the rate of oxygen from the ambient. Therefore, the total mass flow rate of the inlet air W_{in} can be represented by stack current and

oxygen excess ratio, expressed as follows:

$$\begin{aligned} W_{\text{in}} &= W_{\text{O}_2,\text{in}} + W_{\text{N}_2} + W_{\text{vap,in}} \\ W_{\text{O}_2,\text{in}} &= \lambda \cdot W_{\text{O}_2,\text{rea}} \\ W_{\text{N}_2} &= \frac{(1-w_{\text{O}_2})M_{\text{N}_2}}{w_{\text{O}_2} \cdot M_{\text{O}_2}} W_{\text{O}_2,\text{in}} \\ W_{\text{vap,in}} &= \frac{M_{\text{vap}}}{M_{\text{air}}} \frac{p_{\text{vap,amb}}}{p_{\text{air,amb}}} (W_{\text{O}_2,\text{in}} + W_{\text{N}_2}), \end{aligned} \tag{5.5}$$

where $W_{\text{O}_2,\text{in}}$, W_{N_2}, and $W_{\text{vap,in}}$ are the inlet mass flow rates of oxygen, nitrogen, and vapor to the cathode side, M_{N_2}, M_{vap}, and M_{air} are the molar masses of nitrogen, vapor, and dry air, w_{O_2} is the oxygen mass fraction in dry air ($= 0.21$), and $p_{\text{vap,amb}}$ and $p_{\text{air,amb}}$ are the partial pressures of vapor and dry air at the ambient, respectively. The flow rates of the other flows can be obtained similarly.

Once the mass flow rate of each reactant gas is obtained, the pressure of each component can be calculated readily by balancing them. Taking into account the pressure drops in flow channels, the required pressure raise of the compressor p_{cp} can be determined by the inlet air flow rate as follows:

$$p_{\text{cp}} = p_{\text{cp}}(W_{\text{in}}, \alpha_{\text{ch}}) = p_{\text{cp}}(I_{\text{st}}^{\text{fc}}, \lambda, \alpha_{\text{ch}}). \tag{5.6}$$

where α_{ch} is the geometric scaling factor of reactant channels in length.

In order to control the properties of reactant gases, auxiliary components consume significant amounts of energy. Since the compressor consumes more than 80% of all auxiliary energy in high pressure PEM fuel cells, other energy losses are commonly neglected when calculating system net power loss. Assuming a constant mechanical static motor efficiency of 0.9, the compressor power consumption $P_{\text{con}}^{\text{fc}}$ is expressed as follows:

$$P_{\text{con}}^{\text{fc}} = C_p W_{\text{in}} \frac{T_{\text{amb}}}{0.9\eta_{\text{cp}}} \left[\left(\frac{p_{\text{cp}}}{p_{\text{amb}}} \right)^{\frac{\gamma-1}{\gamma}} - 1 \right], \tag{5.7}$$

where C_p and γ are specific heat capacity ($1004\mathrm{J}/(\mathrm{kg}\cdot\mathrm{K})$) and ratio of specific heats (1.4) of air, respectively, W_{in} is the mass flow rate of the system inlet flow, η_{cp} is the compressor efficiency, and p_{cp} and p_{amb} are the pressures of the compressor outlet flow and the ambient, respectively. The compressor is assumed to be static, driven by a static motor. Thus, a static compressor map is used to determine the efficiency corresponding to the required pressure ratio and the mass flow rate of air.

The performance of various compressors needs to be investigated. Because of lack of data, the compressor in this dissertation is scaled geometrically from the Allied Signal compressor given in [38]. Using the similarity principle, the map of a geometrically scaled compressor can be found readily since there is no difference between the flow characteristics of the original and the scaled compressor at a given point in the map. The efficiency η_{cp} and power $P_{\mathrm{con}}^{\mathrm{fc}}$ is predicted to vary with pump size, given by

$$\eta_{\mathrm{cp}} = \eta_{\mathrm{cp}}(\bar{W}_{\mathrm{in}}, \frac{p_{\mathrm{cp}}}{p_{\mathrm{amb}}}) = \eta_{\mathrm{cp}}(\alpha_{\mathrm{cp}}^{-2} W_{\mathrm{in}}, \frac{p_{\mathrm{cp}}}{p_{\mathrm{amb}}}) \quad \text{and} \quad P_{\mathrm{con}}^{\mathrm{fc}} = \alpha_{\mathrm{cp}}^{2} \bar{P}_{\mathrm{con}}^{\mathrm{fc}} \tag{5.8}$$

where $\bar{W}_{\mathrm{in}}$ and W_{in} are the inlet mass flow rate of the unscaled (original) and a newly scaled compressor, respectively, while $\bar{P}_{\mathrm{con}}^{\mathrm{fc}}$ and $P_{\mathrm{con}}^{\mathrm{fc}}$ are the power consumption of the unscaled (original) and a newly scaled compressor, respectively. Also, α_{cp} is the geometric scaling factor in length. The pressure ratio is invariant.

Using the above relations, the power consumed by the compressor motor and the net power output from the fuel cell system can be expressed as a function of stack current and oxygen excess ratio.

5.2.1.2 Representation of Fuel Cell Systems

As shown in Figure 5.1, the linking variables between the fuel cell and powertrain are the weight W^{fc}, specific cost SC^{fc}, number of cells n^{fc} and performance maps of the fuel cell. The number of cells is a shared variable while the others are coupling variables. The weight and specific cost are necessary in evaluating vehicle performance indices in the powertrain model and a vehicle cost in the enterprise model, respectively. According to [24], a fuel cell stack, including membranes, electrodes, gas diffusion layers, bipolar plates and seals, costs and weighs \$360/m^2 and 3.9kg/m^2, respectively. Since the fuel cells developed in 2005 are too expensive and heavy for current vehicles, in this dissertation the stack cost and weight are assumed to \$130/m^2 and 1.9kg/m^2, respectively. Also assuming that the baseline cost for the auxiliary components is \$2000 and the cost of the auxiliaries increases linearly to the compressor volume, we can define the fuel cell system cost C^{fc} as follows:

$$C^{fc} = (130 A^{fc} n^{fc}) + 2000 \alpha_{cp}^3, \tag{5.9}$$

where $A^{fc}(= 0.0769 m^2)$ is the active area of fuel cell. Similarly, the fuel cell system weight can be expressed as follows:

$$W^{fc} = (1.9 A^{fc} n^{fc}) + 15 \alpha_{cp}^3 + 20 \alpha_{ch} + 10. \tag{5.10}$$

Current costs for a fuel cell stack and a fuel cell system are \$67/kW and \$108/kW while the DOE 2005 targets are \$65/kW and \$125/kW, respectively, which means the DOE 2005 targets are met [24]. To be competitive in the automotive market, however, a fuel cell stack should cost less than \$50/kW in mass production [40]. Therefore, assuming the ratio between the costs of a fuel cell stack and a fuel cell

system remains similar, we can consider the market acceptability as follows:

$$\mathrm{SC}^{\mathrm{fc}} = \mathrm{C}^{\mathrm{fc}}/(\text{rated power}) \leq \$80/\mathrm{kW}. \tag{5.11}$$

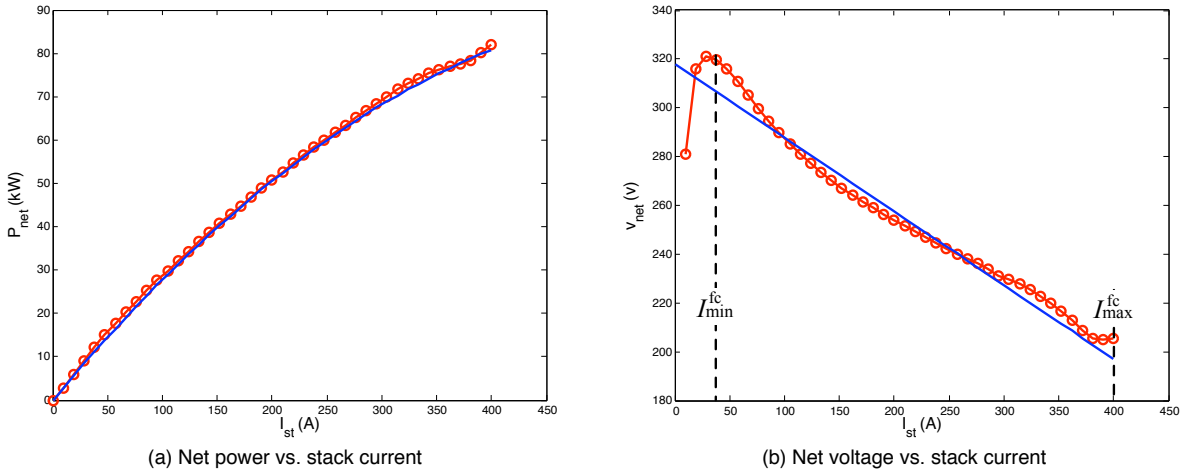

Figure 5.4: Typical fuel cell system performance maps

In order to reduce computational costs due to linking variables, a simple yet accurate representation of performance maps needs to be defined. Figure 5.4 (a) shows a typical relation between the load current and net power output for fuel cell systems. As shown in the figure, the net power output can be approximated as follows:

$$P^{\mathrm{fc}}_{\mathrm{net}} = a^{\mathrm{fc}} I^{\mathrm{fc}\,2}_{st} + b^{\mathrm{fc}} I^{\mathrm{fc}}_{st}, \tag{5.12}$$

where a^{fc} and b^{fc} are the coefficients of the quadratic approximation. Since $P^{\mathrm{fc}}_{\mathrm{net}} = v^{\mathrm{fc}}_{\mathrm{net}} I^{\mathrm{fc}}_{\mathrm{st}}$, $v^{\mathrm{fc}}_{\mathrm{net}} = a^{\mathrm{fc}} I^{\mathrm{fc}}_{st} + b^{\mathrm{fc}}$. As shown in Figure 5.4 (b), the net voltage has a peak at low current. Let the current with the peak voltage be $I^{\mathrm{fc}}_{\mathrm{min}}$. Then, the linear approximation of the net voltage is valid for the range between $I^{\mathrm{fc}}_{\mathrm{min}}$ and the maximum current $I^{\mathrm{fc}}_{\mathrm{max}}$. Thus, assuming that the designed fuel cell system is operated only for

the range between $I^{\text{fc}}_{\text{min}}$ and $I^{\text{fc}}_{\text{max}}$, or setting the lower limit of the net power to $P^{\text{fc}}_{\text{min}} = a^{\text{fc}} {I^{\text{fc}}_{\text{min}}}^2 + b^{\text{fc}} I^{\text{fc}}_{\text{min}}$, the fuel cell map can be represented as follows:

$$\begin{aligned} P^{\text{fc}}_{\text{net}} &= a^{\text{fc}} {I^{\text{fc}}_{st}}^2 + b^{\text{fc}} I^{\text{fc}}_{st}, \\ P^{\text{fc}}_{\text{min}} \leq P^{\text{fc}}_{\text{net}} &\leq P^{\text{fc}}_{\text{max}} = a^{\text{fc}} {I^{\text{fc}}_{\text{max}}}^2 + b^{\text{fc}} I^{\text{fc}}_{\text{max}}. \end{aligned} \tag{5.13}$$

Furthermore, by assuming $I^{\text{fc}}_{\text{min}} = 0.05 I^{\text{fc}}_{\text{max}}$, the performance map can be represented by three variables, namely $a^{\text{fc}}, b^{\text{fc}}$ and $I^{\text{fc}}_{\text{max}}$. Then, the fuel cell subproblem in deterministic ATC formulation can be expressed as follows:

$$\begin{aligned} \text{Given} \quad & \mathbf{t}^{\text{fc}} = \{t_{n^{\text{fc}}}, t_{\text{W}^{\text{fc}}}, t_{\text{SC}^{\text{fc}}}, t_{a^{\text{fc}}}, t_{b^{\text{fc}}}, t_{I^{\text{fc}}_{\text{max}}}\} \\ \min \quad & \boldsymbol{\pi}(\mathbf{t}^{\text{fc}} - \mathbf{r}^{\text{fc}}) \\ \text{with respect to} \quad & \mathbf{x}^{\text{fc}} = \{n^{\text{fc}}, \alpha_{\text{cp}}, \alpha_{\text{ch}}\} \\ \text{subject to} \quad & g^{\text{fc}} = \text{SC}^{\text{fc}} - \$80/\text{kW} \leq 0, \\ & \{50, 0.8, 0.6\} \leq \mathbf{x}^{\text{fc}} \leq \{1000, 1.5, 2\} \\ \text{where} \quad & \mathbf{r}^{\text{fc}} = \mathbf{a}^{\text{fc}}(\mathbf{x}^{\text{fc}}). \end{aligned} \tag{5.14}$$

The compressor and channel scaling factors are assumed to be normally distributed with $\sigma_{\alpha_{\text{cp}}} = \sigma_{\alpha_{\text{ch}}} = 0.02$. On the other hand, the number of cells is considered deterministic and large enough to be relaxed. To the best of our knowledge, it has yet to be proven how to match a map with uncertainty. Thus, we assume that the linking variables related to the map representation are deterministic and the remaining, $t_{\text{W}^{\text{fc}}}, t_{\text{SC}^{\text{fc}}}$, are random. Moreover, the local constraint is treated as a probabilistic constraint with $p_f = 0.13\%$.

5.2.2 Battery Model

In a hybrid powertrain, a secondary power source (such as a rechargeable battery) stores energy from a primary power source (such as an internal combustion engine or a fuel cell) and provides the stored energy under conditions where the primary

power source operates inefficiently. Among various secondary power sources, lithium-ion batteries have gained significant attention due to its high energy density, high open circuit voltage, no memory effect, and a slow loss of charge when not in use.

5.2.2.1 One Dimensional Li-ion Battery Cell Model

A Li-ion battery cell consists of the layers of a negative electrode, a positive electrode and a separator sandwiched by current collectors from both ends, as shown in Figure 5.5. The electrodes are made of two different insertion compounds that determine cell properties including an open circuit voltage and load resistances. In the cell, lithium ions travel between the two electrodes based on the following insertion reaction:

$$\mathrm{Li}_{1-x}\theta_n + \mathrm{Li}_x\theta_p \rightleftharpoons \mathrm{Li}\theta_n + \theta_p, \tag{5.15}$$

where θ_n and θ_p represent the negative and positive insertion materials, respectively. More detailed explanation on Li-ion battery cells and the insertion reaction can be found in [120].

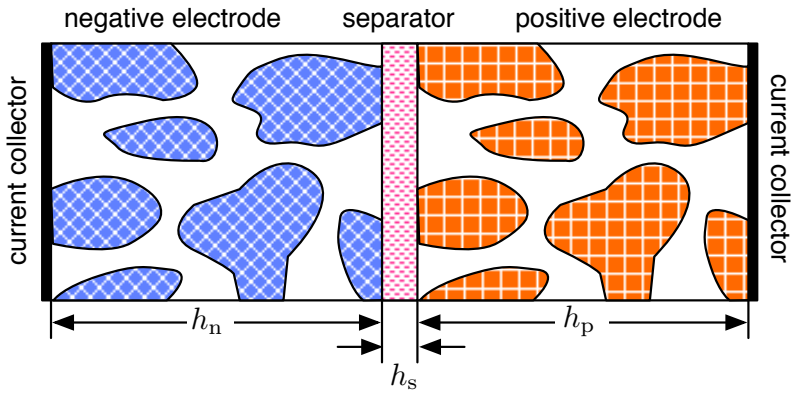

Figure 5.5: Li-ion cell sandwich consisting of composite negative and positive electrode and separator (adapted from [61])

The rate of the insertion reaction is affected by not only cell properties (such as

diffusion coefficients of lithium-ions) but also cell geometries (such as cell thicknesses or active areas). With given cell properties, a wider active area is desirable because it typically results in a lower resistance and higher energy content. Thus, a flat-wound configuration shown in Figure 5.6 is commonly used for batteries in hybrid vehicles [109]. Moreover, because a typical Li-ion cell can generate less than 4.8V, a number of cells need to be connected in series to produce sufficiently high voltage for automotive applications. In this dissertation, a battery pack consists of four battery modules containing twelve Li-ion cells per module. In other words, 48 cells are connected in series for a battery pack.

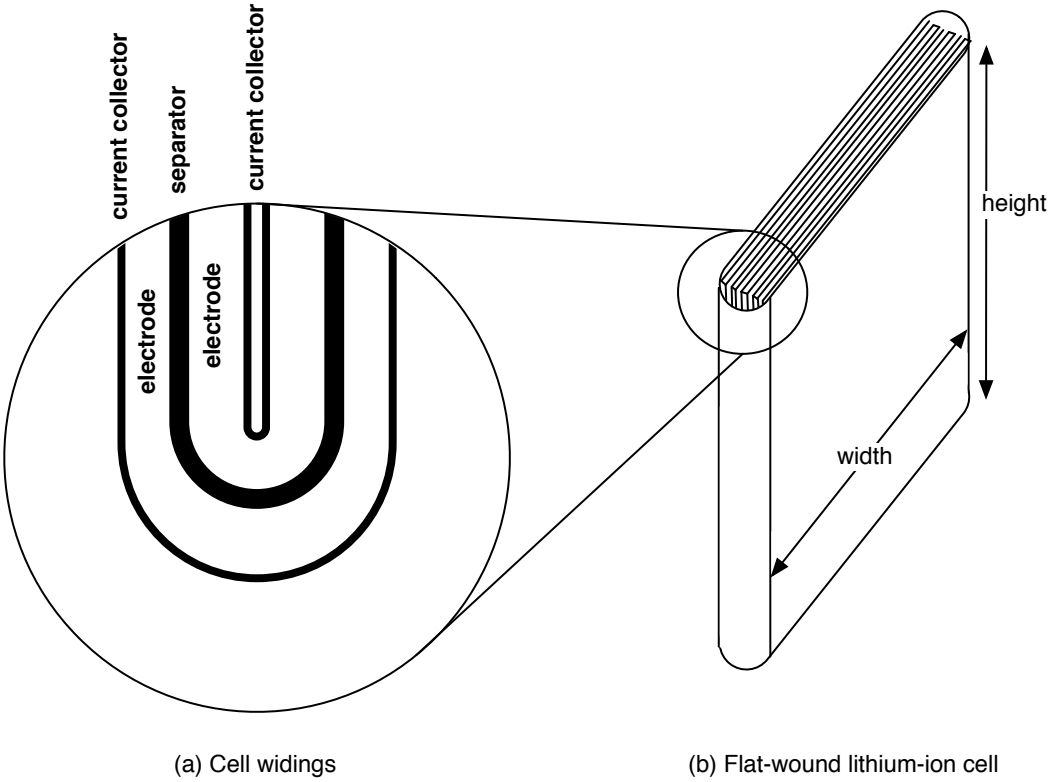

Figure 5.6: Flat-wound lithium-ion battery cell

For design purposes, a 1-D full cell model of Li and Li-ion battery has been developed in [47, 61], assuming the cell is uniform in the directions parallel to the

current collectors. The model can simulate the behavior of a given Li-ion battery cell for a prescribed load cycle. Since most output quantities are normalized by a unit area, including current density (A/m^2), the total rate of heat generation (W/m^2) and the rate of irreversible heat generation (W/m^2), the resulting output can be easily scaled by multiplying the active area. The cell temperature can vary with time if temperature-dependent material properties are provided. Due to lack of data, however, we assume that the temperature of the system is uniform and constant at 25°C. Also we take the cell thicknesses h^{bt} and cell area A^{bt} as the design variables for the battery, assuming the other properties and geometries, such as insertion materials, porosities and number of windings, are fixed. In order to reduce the problem size, the thicknesses of negative and positive electrodes are identical while the ratio of a separator thickness to an electrode thickness is fixed to 0.25, which can be expressed as follows:

$$h_{\mathrm{n}} = h_{\mathrm{p}} = 4h_{\mathrm{s}} = h^{\mathrm{bt}} \tag{5.16}$$

5.2.2.2 Lumped-parameter Battery Model

Because the model requires a relatively high computational cost for powertrain simulation, a lumped-parameter battery model needs to be developed by charactering battery cells, as described in the PNGV battery test manual [1]. In the lumped-parameter battery model, the estimated voltage $v_{\mathrm{net}}^{\mathrm{bt}}$ can be expressed as follows:

$$v_{\mathrm{net}}^{\mathrm{bt}} = E^{\mathrm{bt}} - R_0 I_{\mathrm{l}}^{\mathrm{bt}} - R_{\mathrm{p}} I_{\mathrm{p}}^{\mathrm{bt}}, \tag{5.17}$$

where E^{bt} is an open circuit voltage and R_0 and R_p are cell internal ohmic and polarization resistances, respectively. Also, $I_{\mathrm{l}}^{\mathrm{bt}}$ is a cell load current while $I_{\mathrm{p}}^{\mathrm{bt}}$ is a current through the polarization resistance, derived from the following differential

equation:

$$\frac{dI_{\mathrm{p}}^{\mathrm{bt}}}{dt} = \frac{(I_{\mathrm{l}}^{\mathrm{bt}} - I_{\mathrm{p}}^{\mathrm{bt}})}{\tau_{\mathrm{p}}}, \tag{5.18}$$

where τ_{p} is a polarization time constant. Because the open circuit voltage does not depend on cell geometries but cell materials, the open circuit voltage for the Li_x|graphite + Li_y CoO_2 cell can be easily obtained from the 1-D battery cell model, expressed as follows:

$$E^{\mathrm{bt}} = 4.03x^4 - 11.96x^3 + 11.99x^2 - 3.53x + 4.02, \tag{5.19}$$

where $x = \%\,\mathrm{SOC}/100$. On the other hand, the resistances depend on cell geometries, such as cell thicknesses. Thus, in order to measure the resistances and develop a lumped-parameter battery model, the 1-D battery cell model is simulated for a load cycle, corresponding to the hybrid pulse power characterization (HPPC) tests described in [1].

The HPPC tests are performed for the SOC range of 55-85% because the range is wide enough for batteries to run a cycle and the internal resistances can be approximated accurately by a second order polynomial function over the range. Then, the HPPC test results are used to estimate the resistances and the polarization time constant. Note that two different internal resistances need to be estimated, namely charging and discharging resistances. Since R_{p} and τ_{p} are less sensitive to SOC than the charging and discharging resistances, R_{p} and τ_{p} are set to constants. Figure 5.7 shows an example of an HPPC test result and a fitted model.

Figure 5.8 presents the estimated discharging and charging resistances and their quadratic approximations. As shown in the figure, the quadratic approximations agree with the estimated resistances sufficiently. Note that the resistances show con-

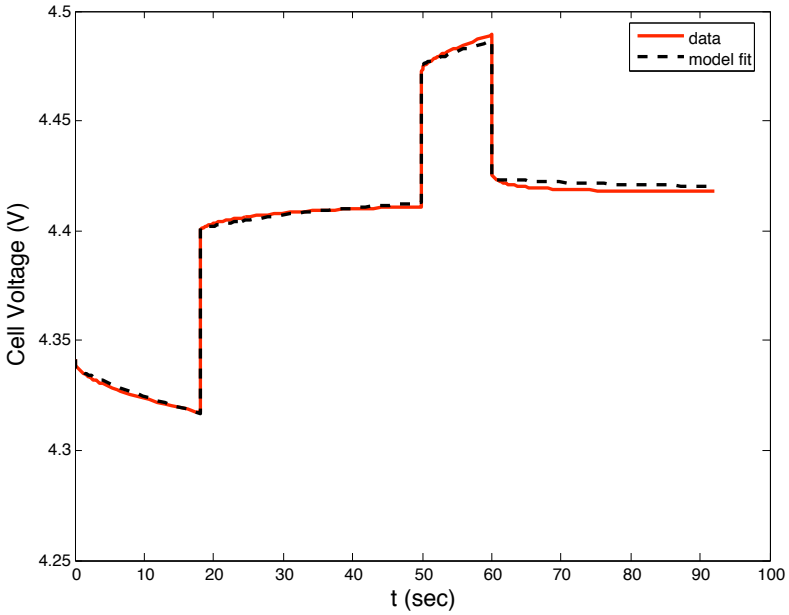

Figure 5.7: Voltage data for HPPC test showing agreement between measured voltages and lumped-parameter battery model

siderably similar slopes to each other over the SOC range. Thus, in order to reduce the number of linking variables, the resistance functions are modeled as follows:

$$\begin{aligned} \text{Discharging} \quad &: R_{\text{dis}} = (a^{\text{bt}}x^2 + b^{\text{bt}}x + c^{\text{bt}}) \cdot A^{\text{bt}}n^{\text{bt}} \\ \text{Charging} \quad &: R_{\text{chr}} = (a^{\text{bt}}x^2 + b^{\text{bt}}x + c^{\text{bt}} - d^{\text{bt}}) \cdot A^{\text{bt}}n^{\text{bt}} \end{aligned} \tag{5.20}$$

where a^{bt}, b^{bt} and c^{bt} are the average of the coefficients of the quadratic approximations and d^{bt} is the mean value of the differences of the resistances. Note that they are the functions of h^{bt}. The active area, A^{bt}, and the number of cells, (n^{bt}=48), are multiplied so that the R_{dis} and R_{chr} represent the discharging and charging resistances for a pack, respectively.

For powertrain simulation, the weight W^{bt} and the columbic capacity Cp^{bt} of batteries need to be estimated. Since the library in the 1-D model provides densities of materials, the mass of battery cells can be obtained easily. The packaging mass is also taken into account by assuming the mass is linear to the pack length with

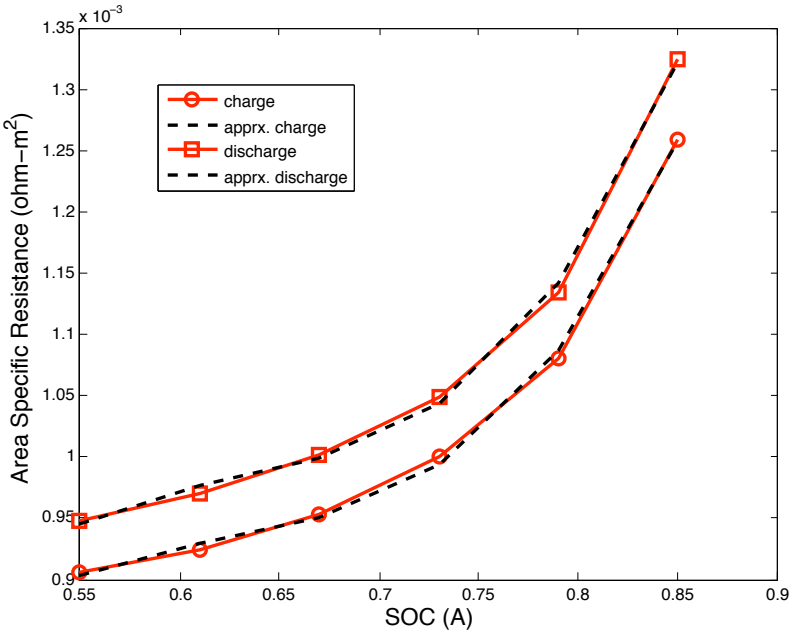

Figure 5.8: Discharging and charging resistances of a Li-ion battery showing agreement between estimated resistances and quadratic approximations

a residual mass. The columbic capacity in Ah is estimated based on how many Li-ions are included because a Li-ion corresponds to an electron in insertion reaction. Then, the battery subproblem in a deterministic ATC formulation can be expressed as follows:

$$\begin{aligned}
\text{Given} \quad & \mathbf{t}^{\text{bt}} = \{t_{\text{W}^{\text{bt}}}, t_{\text{Cp}^{\text{bt}}}, t_{a^{\text{bt}}}, t_{b^{\text{bt}}}, t_{c^{\text{bt}}}, t_{d^{\text{bt}}}\}, \\
\min \quad & \boldsymbol{\pi}(\mathbf{t}^{\text{bt}} - \mathbf{r}^{\text{bt}}) \\
\text{with respect to} \quad & \mathbf{x}^{\text{bt}} = \{h^{\text{bt}}, A^{\text{bt}}\} \\
\text{subject to} \quad & \{0.5 \times 10^{-4}, 0.5A_0^{\text{bt}}\} \leq \mathbf{x}^{\text{bt}} \leq \{2 \times 10^{-4}, 3A_0^{\text{bt}}\} \\
\text{where} \quad & \mathbf{r}^{\text{bt}} = \mathbf{a}^{\text{bt}}(\mathbf{x}^{\text{bt}}), \quad A_0^{\text{bt}} = 0.528.
\end{aligned} \tag{5.21}$$

Both local variables are assumed to have normal distribution with $\sigma_{h^{\text{bt}}} = 0.02 \times 10^{-4}$, $\sigma_{A^{\text{bt}}} = 0.02A_0^{\text{bt}}$. Also, the weight and capacity are considered random while the linking variables related with resistance maps are deterministic.

5.2.3 Powertrain Model

A hybrid powertain requires a power-management strategy to determine optimal power split. A poorly designed power-management strategy may result in worse fuel economy than that of conventional vehicles. Therefore, several strategies have been developed using a rule-based control [56, 67], dynamic programming (DP) [98, 96], stochastic dynamic programming (SDP) [97] and equivalent consumption minimization strategy (ECMS) [64, 111]. One of the major issues in strategy development is lack of causality. In other words, most strategies require *a priori* knowledge on a driving cycle and a nested optimization process for finding optimal control parameters for the cycle. The lack of causality may result in a serious robustness problem because the optimized control parameters for one driving cycle may not split the power properly for other driving cycles. Since ECMS provides robust power management compared to other strategies according to [115], we employ the strategy for our hybrid powertrain simulation.

Since design variables are fixed during nested optimization for control parameter estimation, the power required by the motors is also fixed if we assume that hybrid power sources, namely fuel cells and batteries, can provide sufficient power ideally. In other words, we can decouple the electrical part (including fuel cells, batteries and a power-management controller) from the mechanical part (including the parts between wheels to motors) as illustrated in Figure 5.9. The decoupling can be computationally effective because the nested optimization process simulates only the electrical part with the required power obtained from the mechanical part. Satisfaction of the assumption of providing sufficient power by the electrical part is assured by a design

constraint as follows:

$$g^{\text{pt}}_{\text{power}} = \max\{P^{\text{pt}}_{\text{req}}(t) - P^{\text{pt}}_{\text{avl}}(t)\} \leq 0. \tag{5.22}$$

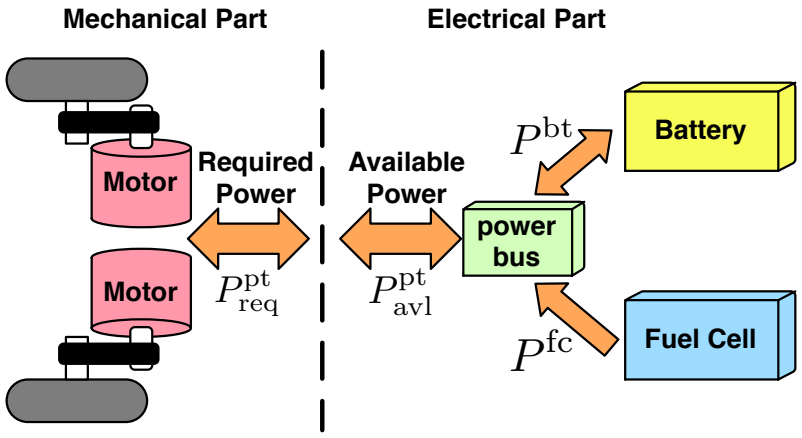

Figure 5.9: Decoupling of a hybrid powertrain into mechanical and electrical parts

Similarly, the motors need to provide sufficient torque and speed for the vehicle to follow the driving cycle, which can be expressed as:

$$\begin{aligned} g^{\text{pt}}_{\text{torque}} &= \max\{\tau_{\max}(w^{\text{mt}}(t)) - \tau^{\text{mt}}(t), \tau^{\text{mt}}(t) - \tau_{\min}(w^{\text{mt}}(t))\} \leq 0, \\ g^{\text{pt}}_{\text{speed}} &= \max\{w_{\max} - w^{\text{mt}}(t)\} \leq 0, \end{aligned} \tag{5.23}$$

where $\tau_{\max}$ and $\tau_{\min}$ are the maximum and minimum torques while $w_{\max}$ is the maximum angular velocity. For acceleration performance, the 0-60 mph time, t_{0-60}, is measured and should be less than 8 sec:

$$g^{\text{pt}}_{0-60} = t_{0-60} - 8 \leq 0. \tag{5.24}$$

5.2.3.1 Mechanical Part

This dissertation focuses on designing a light truck whose curb weight is about 2500kg. Models for the mechanical parts are developed by J.T. Allison [6], including

a detailed motor model. The vehicle includes two motors: one for each wheel on the rear axis. By the motor model, a motor map is generated as a function of motor geometries, namely a rotor radius, the number of turns per stator coil and a rotor resistance. In this dissertation, the rotor radius, rm is assumed to be the only designable geometry. Details on the motor model can be found in [6].

Since motors can cover wider speed and torque ranges more efficiently than conventional IC engines, the conventional gearbox is removed and the motors are connected to the wheels through a belt and pulley system. Thus, the final drive ratio is determined by the pulley speed ratio, pr. With a given rotor radius and pulley speed ratio, the mechanical part model estimates the required power, $P_{\text{req}}^{\text{pt}}(rm, pr)$. The weights of the fuel cell, the battery and the motors are also taken into account.

5.2.3.2 Electrical Part

The electrical part consists of three major models: a fuel cell, a battery and a powerbus. The powerbus splits the power demand from the mechanical part into the power demands to the fuel cell and the battery and combines the power supplied from the two power sources to drive the motors. In order to determine the power split during a cycle, a power management strategy needs to be defined. As mentioned already, ECMS is used in this dissertation due to its robustness and ease of implementation. In ECMS, the instantaneous energy consumption J_t is defined as the weighted sum of the fuel energy consumed in the fuel cell, $\dot{E}_{\text{H}_2}$, and the equivalent electric energy consumed in the battery, $\dot{E}_{\text{e}^-}$, expressed as follows:

$$J_t = \dot{E}_{\text{H}_2}(P^{\text{fc}}(t)) + s\dot{E}_{\text{e}^-}(P^{\text{bt}}(t)), \tag{5.25}$$

where P^{fc} and P^{bt} are the powers generated in the fuel cell and battery, respectively. The weighting factor s needs to be defined by a nested optimization because the two energy conservations are not directly comparable. In Eq.(5.25), the energy consumptions can be expressed as:

$$\begin{aligned} \dot{E}_{\text{H}_2} &= H_{\text{LHV}} \dot{m}_{\text{H}_2}(P^{\text{fc}}(t)) \\ \dot{E}_{\text{e}^-} &= \begin{cases} \alpha_{\text{dis}} P^{\text{bt}}(t)/\eta^{\text{bt}} & \text{(discharging)} \\ \alpha_{\text{chr}} \eta^{\text{bt}} P^{\text{bt}}(t) & \text{(charging)} \end{cases}, \end{aligned} \tag{5.26}$$

where H_{LHV} is the low heating value of hydrogen, $\dot{m}_{\text{H}_2}$ is the rate of hydrogen consumption and η^{bt} is the efficiency of the battery. The α_{dis} and α_{chr} can be different because the charging and discharging efficiencies are not identical. For computational efficiency, however, αs are set to 1 because fuel economy estimations with the same α are sufficiently close to those with two different αs [108]. In ECMS, therefore, the following instantaneous optimization problem is solved at each time t:

$$\begin{aligned} \min_{P^{\text{bt}}} \quad & J_t(P^{\text{bt}}, P^{\text{fc}}) \\ \text{subject to} \quad & P^{\text{pt}}_{\text{req}} = P^{\text{bt}} + P^{\text{fc}}, \\ & P^{\text{bt}}_{\text{min}}(t) \le P^{\text{bt}}(t) \le P^{\text{bt}}_{\text{max}}(t), \\ & P^{\text{fc}}_{\text{min}} \le P^{\text{fc}}(t) \le P^{\text{fc}}_{\text{max}}, \\ & \text{SOC}_{\text{min}} \le \text{SOC}(t) \le \text{SOC}_{\text{max}}, \end{aligned} \tag{5.27}$$

where $P^{\text{bt}}_{\text{min}}$ and $P^{\text{fc}}_{\text{max}}$ are the minimum and maximum powers available from the battery, respectively. In Eq.(5.27), the state of charge (SOC) is bounded by the maximum and minimum SOCs that are set to be 0.55 and 0.85, respectively, because the battery model is valid only for the range.

The performance of ECMS depends highly on the weighting factor that varies by the driving conditions and vehicle designs. Thus, for every design change, a nested

optimization needs to be executed in order to find the optimal s, minimizing the overall fuel consumption subject to the SOC sustainability constraint, expressed as:

$$\begin{aligned} \min_{s} \quad & \int_0^{t_f} \dot{m}_{\mathrm{H_2}} dt \\ \text{subject to} \quad & g^{\mathrm{pt}}_{\mathrm{SOC}} = |\mathrm{SOC}(t_f) - \mathrm{SOC}(0)| - 0.001 \leq 0. \end{aligned} \tag{5.28}$$

In order to estimate the hydrogen consumption in Eq.(5.26) and (5.28), the fuel cell module uses a simple map generated from the quasi-steady fuel cell model of Section 5.2.1. Since most of the transient phenomena in fuel cells are faster than the vehicle dynamics, the fuel cell dynamics are approximated by a first order system, whose time constant is about 2 seconds. Thus, the fuel cell module can produce the same power as demanded almost immediately. The maximum and minimum demands are limited to the maximum and minimum powers defined in Eq.(5.13).

The cost of the powertain, C^{pt}, needs to be estimated for enterprise decisions that can be expressed as follows:

$$\mathrm{C}^{\mathrm{pt}} = \mathrm{C}^{\mathrm{fc}} + \mathrm{C}^{\mathrm{bt}} + \mathrm{C}^{\mathrm{mt}} - \mathrm{C}^{\mathrm{ic}}, \tag{5.29}$$

where $\mathrm{C}^{\mathrm{fc}}, \mathrm{C}^{\mathrm{bt}}$ and C^{mt} are the cost of the fuel cell, the battery and the motor while C^{ic} is the cost of a target IC engine whose max power is 200kW. Since the specific cost of IC engines is not readily available, we employ the same assumption as in [110], *i.e.*, (ICE specific cost) = 19\$/kW. Thus, C^{ic} = \$ 3800. Also, C^{fc} is estimated as follows:

$$\mathrm{C}^{\mathrm{fc}} = \mathrm{SC}^{\mathrm{fc}} P^{\mathrm{fc}}_{\mathrm{max}} \tag{5.30}$$

For the battery and motor cost, cost models, presented in [99], are used, expressed

as follows:

$$\begin{aligned} \mathrm{C}^{\mathrm{bt}} &= \max\{MCC, MCC_{\min}\} \cdot W^{\mathrm{bt}} + BAUX, \\ \mathrm{C}^{\mathrm{mt}} &= 368.7 + (127.7\ln[P^{\mathrm{mt}}_{\max}]) + 2.95P^{\mathrm{mt}}_{\max} \\ &\text{where} \quad MCC = MCC^* - \frac{EDTB_{C/3} - EDTB^*_{C/3}}{K_{\mathrm{BM}}} \cdot \ln[EDTB_{C/3}], \end{aligned} \tag{5.31}$$

where:

MCC	=	the estimated OEM cost of manufacturing a battery module (OEM selling price) per kg ($/kg),
$MCC_{\min}$	=	the minimum allowable manufacturing cost, as a bound on the MCC function (0 $/kg),
$BAUX$	=	the cost of the battery auxiliaries: tray, straps, bus bar, terminal interconnects, electrical harness, and thermal management system (100$),
MCC^*	=	the reference OEM manufacturing cost (selling price) per kg, for batteries of the reference specific energy (50 $/kW),
$EDTB_{C/3}$	=	the specific energy of the new battery (Wh/kg),
$EDTB^*_{C/3}$	=	the reference specific energy of the new battery (200 Wh/kg),

and K_{BM} = coefficient (15). Since the battery model is developed for NiMH batteries, the reference OEM manufacturing cost and the reference specific energy are modified for Li-ion batteries while the minimum allowable manufacturing cost is set to 0$/kg due to lack of data. Then, the powertrain subproblem in a deterministic

ATC formulation can be expressed as follows:

$$\begin{aligned}
\text{Given} \quad & \mathbf{t}^{\text{pt}} = \{t_{\text{fe}^{\text{pt}}}, t_{\text{C}^{\text{pt}}}\}, \mathbf{r}^{\text{fc}}, \mathbf{r}^{\text{bt}}, \\
\min \quad & \boldsymbol{\pi}(\{\mathbf{t}^{\text{pt}} - \mathbf{r}^{\text{pt}}, \mathbf{t}^{\text{fc}} - \mathbf{r}^{\text{fc}}, \mathbf{t}^{\text{bt}} - \mathbf{r}^{\text{bt}}\}) \\
\text{with respect to} \quad & \mathbf{x}^{\text{pt}} = \{rm, pr\}, \mathbf{t}^{\text{fc}}, \mathbf{t}^{\text{bt}} \\
\text{subject to} \quad & g^{\text{pt}}_{\text{power}} \leq 0, \quad g^{\text{pt}}_{\text{torque}} \leq 0, \quad g^{\text{pt}}_{\text{speed}} \leq 0, \quad g^{\text{pt}}_{\text{SOC}} \leq 0 \\
& g^{\text{pt}}_{0-60} = t_{0-60} - 8 \leq 0, \quad \{0.1, 1\} \leq \mathbf{x}^{\text{pt}} \leq \{0.2, 3\}, \\
\text{where} \quad & \mathbf{r}^{\text{pt}} = \mathbf{a}^{\text{pt}}(\mathbf{x}^{\text{pt}}, \mathbf{t}^{\text{fc}}, \mathbf{t}^{\text{bt}}).
\end{aligned} \tag{5.32}$$

The rotor radius is deterministic while the pulley ratio is normally distributed with $\sigma_{pr} = 0.002$. In this subproblem, the local constraints are assumed deterministic. Due to the nested optimization and ECMS, $g^{\text{pt}}_{\text{SOC}}$ is not violated unless the power sources are too small for the vehicle. For fuel economy estimation, Simplified Federal Urban Driving Schedule (SFUDS) is used.

5.2.4 Enterprise Model

The objective of enterprise decision is to maximize the profit subject to marketing constraints. Here we consider a simple gross profit π^{ent}, calculated as the total revenue minus the cost of obtaining the revenue. Revenue is basically price, P^{ent}, times quantity, q^{ent}, considering the sales of the designed vehicle is the only economic activity. Also, we consider only the manufacturing cost of the vehicle, ignoring the operational expenses such as marketing and sales expenditures. This section provides a brief explanation of the profit model while detailed explanation is presented in [35].

5.2.4.1 Price and Demand

Based on standard assumptions in the microeconomic literature, a negative linear relationship between price and quantity demanded of conventional light class trucks

Table 5.2: Historical product price and demand data points and demand values adjusted for expected new product penetration

Year	Price	Quantity (thousand)	Adjusted quantity (thousand)
2001	\$23,632	9278.3	927.83
2002	$(\$24{,}585)_{98}$	8721.4	872.14

can be drawn from the two pairs of price and annual sales data in 2001 and 2002, shown in Table 5.2 [2, 99]. We assume that the enterprise has decided to allocate 10% of its existing capacity for the production of the new product. Moreover, following the argument in [35], the demand is assumed to be shifted by the fuel cost saving S^{ent}, and the resulting demand curve can be expressed as follows:

$$q^{\text{ent}} = \theta - \frac{\Delta q^{\text{ent}}}{\Delta P^{\text{ent}}} P^{\text{ent}} + \frac{\Delta q^{\text{ent}}}{\Delta S^{\text{ent}}} S^{\text{ent}}. \tag{5.33}$$

Solving with respect to price we have

$$P^{\text{ent}} = \frac{\theta}{\Delta q^{\text{ent}}/\Delta P^{\text{ent}}} - \frac{\Delta P^{\text{ent}}}{\Delta q^{\text{ent}}} q^{\text{ent}} + \frac{\lambda_{S^{\text{ent}}}}{\lambda_{P^{\text{ent}}}} S^{\text{ent}}, \tag{5.34}$$

where $\lambda_{S^{\text{ent}}} = \Delta q^{\text{ent}}/\Delta S^{\text{ent}}$ and $\lambda_{P^{\text{ent}}} = \Delta q^{\text{ent}}/\Delta P^{\text{ent}}$. $\lambda_{S^{\text{ent}}}$ can be interpreted as the fuel cost saving elasticity of demand, meaning the responsiveness of the quantity demanded of a good to a change in the expected fuel cost saving. Due to lack of knowledge on the new technology, the ratio $\lambda_{S^{\text{ent}}}$ is unknown in this dissertation. In order to determine the demand curve, it is needed to realize consumer behavior toward the new technology through consumer preference constraints.

A consumer's aversion toward the new technology can be modeled by a net utility threshold V^{ent} [3]. As in [35], for market acceptability, the difference between fuel saving from a hybrid fuel cell vehicle and change in price should be greater than the threshold, expressed as follows:

$$S^{\text{ent}} - (P^{\text{ent}} - \bar{P}^{\text{ent}}_{01|02}) \geq V^{\text{ent}}, \tag{5.35}$$

Table 5.3: Lifecycle Mileage of a light truck [54]

Age	Miles	Age	Miles	Age	Miles	Age	Miles	Age	Miles
1	28,951	7	17,035	13	10,146	19	6,111	25	3,720
2	26,479	8	15,613	14	9,317	20	5,622	26	3,427
3	24,226	9	14,314	15	8,558	21	5,173	27	3,159
4	22,173	10	13,128	16	7,864	22	4,762	28	2,913
5	20,301	11	12,043	17	7,227	23	4,384	29	2,686
6	18,593	12	11,052	18	6,645	24	4,038	30	2,477

where $\bar{P^{\text{ent}}}_{01|02}$ is the average of 2001 and 2002 market prices of the current conventional light truck design, which is set to \$ 24,108.5. Because the value of V^{ent} cannot be verified, we will treat it as a parameter in the optimization. Its value is, however, determined after the following discussion on the fuel cost saving.

In order to estimate the fuel cost saving, miles traveled, the rate of fuel consumption and fuel price need to be known. A lifecycle mileage of a light tucks is presented by Environmental Protection Agency [54] (see Table 5.3) and the rate of fuel consumption is the inverse of fuel economy obtained from the powertrain model assuming that the initial fuel economy is maintained for the period. On the other hand, the fuel price is uncertain because it fluctuates across time. In [35], the fuel price is assumed to follow the mean-reverting process, expressed as follows:

$$\begin{aligned} \Delta D_{\text{dsl}} &= \alpha^{\text{ent}}_{\text{dsl}}(D_{\text{dsl}} - \bar{D}_{\text{dsl}})\Delta t + \sigma^{\text{dsl}}\Delta z, \\ \Delta z &= \eta^{\text{ent}}\sqrt{\Delta t}, \quad \eta^{\text{ent}} \sim N(0,1), \end{aligned} \tag{5.36}$$

where α is the speed of reversion, $\bar{D}_{\text{dsl}}$ is the normal level of D_{dsl} and σ^{dsl} is the volatility of diesel fuel price, estimated from historical monthly diesel fuel prices from March 1994 to October 2007 [44]. The mean-reverting process can be used for predicting the diesel fuel price for an ICE vehicle. On the other hand, at present there is no such commodity market for hydrogen, and data for hydrogen prices are not rich enough for the mean-reverting process to be applied. The given information,

however, indicates the current hydrogen prices are ranging from \$4.40/kg to \$5.00/kg [122]. Also, the Department of Energy (DOE) has set the 2005 target for the end-user cost of hydrogen to \$2.00/kg - \$3.00/kg [45]. Therefore, this dissertation assumes that the hydrogen price is \$3/kg currently and increases at a static inflation rate, r^{ent}, that is assumed to be 3%. The model for hydrogen prices, therefore, is not suitable for a long-term prediction. Instead, we can assume that both price models are valid in a short-run, such as 2 years.

For diesel price, we can generate a random walk for the period based on Eq.(5.36). Discounting back with the static inflation rate, r^{ent}, the diesel fuel expense can be calculated in:

$$\mathrm{C}_{\text{dsl}} = \int_0^{2\text{yr}} \frac{D_{\text{dsl}} M_t e^{-r^{\text{ent}} t}}{\text{fe}_{\text{dsl}}} dt, \tag{5.37}$$

where M_t denotes miles traveled while fe_{dsl} is the fuel economy of a conventional light truck whose average value is reported to be 22.3 mpg in [128]. In order to consider multiple future scenarios, the process is repeated 100,000 times and the mean of the fuel expenses is used for the rest of model. On the other hand, because hydrogen price increases at r^{ent}, the hydrogen fuel expense can be expressed as:

$$\mathrm{C}_{\mathrm{H}_2} = \frac{3(28961 + 26479)}{\text{fe}^{\text{pt}}}. \tag{5.38}$$

From Eq.(5.37) and (5.38), fuel cost saving is expressed as follows:

$$S^{\text{ent}} = \int_0^{2\text{yr}} \frac{D_{\text{dsl}} M_t e^{-r^{\text{ent}} t}}{\text{fe}_{\text{dsl}}} dt - \frac{3(28961 + 26479)}{\text{fe}^{\text{pt}}}. \tag{5.39}$$

Back to consumer preference, the constraint in [35] cannot be applied directly here because the fuel cost saving in the paper was calculated for 20 years not 2 years. Instead, we assume similar constraints taking account of the consumer preference.

First, assume that consumers want their return of an investment after 2 years to be larger than the half of the cost of the investment. Additionally, for a long-term prediction, eight times the fuel cost saving should be larger than the price difference by V^{ent} =\$ 10,000, similar to the costumer preference constraint in [35]. Both constraints can be expressed mathematically as follows:

$$\begin{aligned} g_1^{\text{ent}} &= (P^{\text{ent}} - \bar{P}_{01|02}^{\text{ent}}) - 2S^{\text{ent}} \leq 0, \\ g_2^{\text{ent}} &= (P^{\text{ent}} - \bar{P}_{01|02}^{\text{ent}}) - 8S^{\text{ent}} - 10000 \leq 0. \end{aligned} \tag{5.40}$$

Modeling of a sophisticated costumer preference is possible but beyond the scope of this demonstration.

5.2.4.2 Manufacturing Cost

The manufacturing cost includes the production cost $\text{C}_{\text{P}}^{\text{ent}}$ and the powertrain cost C^{pt}. Since C^{pt} can be estimated from the powertrain model, the production cost needs to be defined. Due to lack of data, the regression model in [35] is scaled down by the ratio between the prices of light and medium trucks, expressed as follows:

$$\text{C}_{\text{P}}^{\text{ent}} = 3.05 \times 10^4 - 44.5q^{\text{ent}} + 0.0443 * {q^{\text{ent}}}^2 \tag{5.41}$$

Then, assuming that the enterprise has allocated the maximum monthly capacity to 1200, the enterprise subproblem in a deterministic ATC formulation can be expressed as follows:

$$\begin{aligned} \text{Given} \quad & \mathbf{r}^{\text{pt}} \\ \min \quad & \boldsymbol{\pi}(\{-\pi^{\text{ent}}, \mathbf{t}^{\text{pt}} - \mathbf{r}^{\text{pt}}\}) \\ \text{with respect to} \quad & \mathbf{x}^{\text{ent}} = \{\tfrac{\lambda_S^{\text{ent}}}{\lambda_P^{\text{ent}}}, q^{\text{ent}}\}, \mathbf{t}^{\text{pt}} \\ \text{subject to} \quad & g_1^{\text{ent}} \leq 0 \quad g_2^{\text{ent}} \leq 0 \quad g_3^{\text{ent}} = q^{\text{ent}} - 1200 \leq 0, \\ & \{0.1, 60\} \leq \mathbf{x}^{\text{ent}} \leq \{0.9, 1200\}. \end{aligned} \tag{5.42}$$

The lack of understanding of market behavior is taken into account as uncertainties in local variables with $\sigma_{\lambda_S^{\text{ent}}/\lambda_P^{\text{ent}}} = 0.02$, $\sigma_{q^{\text{ent}}} = 30$. Also, the local constraints are treated as probabilistic constraints with $p_f = 0.13\%$.

5.3 Results and Discussion

To facilitate numerical computation, the design variables are scaled to 1. For example, the number of cells is divided by 500 and the cell thickness is multiplied by 1000. The scaled initial point is the deterministic optimal point, $\{\mathbf{x}^{\text{ent}}, \mathbf{x}^{\text{pt}}, \mathbf{x}^{\text{fc}}, \mathbf{x}^{\text{bt}}\} = \{0.873, 0.980, 2.41, 1.43, 0.980, 1.23, 1.51, 1.99, 1.84\}$. Parameters for the suspension strategy are set to $\zeta_t = 0.2$ and $\zeta_f = 0.8$; the initial trust region is set to 0.01. The problem is solved by SLP-based PATC with and without the suspension strategy. During PATC with the suspension strategy, we find that the coupling between the enterprise and powertrain is significantly stronger those that between the powertrain and the other two subsystems. Therefore, the coupling between the enterprise and powertain is also assumed suspendable, as shown in Figure 5.10. Criteria for the modified suspension strategy for the powertrain model are expressed as follows:

$$\begin{aligned}
&\text{if } ||\mathbf{d}^l_{\boldsymbol{\mu}_{\mathbf{R}_{22}}}|| < \zeta_t\left(\frac{||\mathbf{d}^l_{\boldsymbol{\mu}_{\mathbf{R}_{22}}}||}{3} + \sum_{k\in\mathcal{C}_{22}} \frac{||\mathbf{d}^l_{\boldsymbol{\mu}_{\mathbf{T}_{3k}}}||}{3}\right), \quad O_{11} \text{ is suspended;} \\
&\text{if } ||\mathbf{d}^l_{\boldsymbol{\mu}_{\mathbf{T}_{33}}}|| < \zeta_t\left(\frac{||\mathbf{d}^l_{\boldsymbol{\mu}_{\mathbf{R}_{22}}}||}{3} + \sum_{k\in\mathcal{C}_{22}} \frac{||\mathbf{d}^l_{\boldsymbol{\mu}_{\mathbf{T}_{3k}}}||}{3}\right), \quad O_{33} \text{ is suspended;} \\
&\text{if } ||\mathbf{d}^l_{\boldsymbol{\mu}_{\mathbf{T}_{34}}}|| < \zeta_t\left(\frac{||\mathbf{d}^l_{\boldsymbol{\mu}_{\mathbf{R}_{22}}}||}{3} + \sum_{k\in\mathcal{C}_{22}} \frac{||\mathbf{d}^l_{\boldsymbol{\mu}_{\mathbf{T}_{3k}}}||}{3}\right), \quad O_{34} \text{ is suspended.}
\end{aligned} \tag{5.43}$$

Table 5.4 summarizes the results obtained from the three methods: the SLP-based PATC without suspension strategy (denoted as *PLATC*), the SLP-based PATC with the suspension strategy based on Eq.(4.12) (denoted as *PLATC-SS*1) and the SLP-based PATC with the modified suspension strategy based on Eq. (5.43) (denoted as

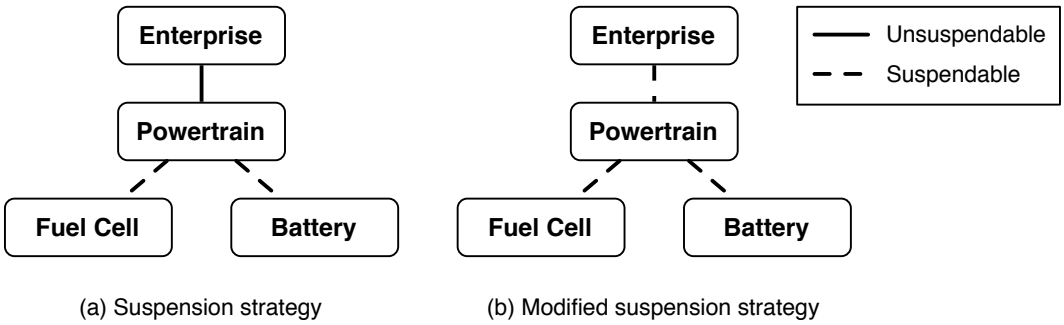

Figure 5.10: Modified suspension strategy taking into account of the coupling between enterprise and powertrain models

Table 5.4: Optimal solutions and number of redesigns for the HEFCV design problem

	$\mathbf{x}^*$ (scaled)					
PLATC	$\{0.16, 1.07, 2.15, 1.89, 0.96, 1.23, 1.37, 1.94, 1.84\}$					
*PLATC-SS*1	$\{0.16, 1.07, 2.15, 1.89, 0.96, 1.23, 1.37, 1.94, 1.84\}$					
*PLATC-SS*2	$\{0.16, 1.07, 2.15, 1.89, 0.96, 1.23, 1.37, 1.94, 1.84\}$					
	f_e^*	consistency error	number of redesigns			
			O_{11}	O_{22}	O_{33}	O_{34}
PLATC	\$68,600	2.61×10^{-4}	571	1529	350	274
*PLATC-SS*1	\$68,600	2.98×10^{-4}	571	1529	350	241
*PLATC-SS*2	\$68,600	3.03×10^{-4}	571	1529	219	163

*PLATC-SS*2). All algorithms result in an exactly identical solution at the optimum. Moreover, g_1^{ent}, g_{0-60}^{pt} and g^{fc} are active and $\lambda_S^{\text{ent}}/\lambda_P^{\text{ent}}$ and h^{bt} are bounded by the upper and lower bounds, respectively.

The AIO approach takes about 200 seconds per design point on a PC with a 3.4GHz CPU and 1GB RAM. Since Monte Carlo Simulation (MCS) with 100,000 samples would take about 230 per design point, MCS was not performed to solve the problem but to validate the accuracy of the solution. The proposed methods are, however, efficient enough to find a solution under uncertainty with FORM/SORM approximation. Note that the modified suspension strategy is more effective than the original suspension strategy. Because the fuel economy is considerably sensitive to the motor radius compared to the targets to the fuel cell and battery, the cou-

Table 5.5: Reliability analysis results (MCS with 20,000 samples)

Constraint	g_1^{ent}	g_2^{ent}	g_3^{ent}	g_{0-60}^{pt}		g^{fc}
PLATC	Active	Inactive	Inactive	Active		Active
MCS p_f (%)	0.65	0	0	0.12		0.13
Linking variables	$\mu_{\text{Fe}^{\text{pt}}}$	$\mu_{\text{C}^{\text{pt}}}$	$\mu_{\text{W}^{\text{fc}}}$	$\mu_{\text{SC}^{\text{fc}}}$	$\mu_{\text{W}^{\text{bt}}}$	$\mu_{\text{Cp}^{\text{bt}}}$
PLATC	48.6 mpg	\$8600	134kg	74.9\$/kg	95.2kg	223Ah
MCS	46.8 mpg	\$9590	135kg	75.6\$/kg	95.8kg	225Ah
Linking variables	$\sigma_{\text{Fe}^{\text{pt}}}$	$\sigma_{\text{C}^{\text{pt}}}$	$\sigma_{\text{W}^{\text{fc}}}$	$\sigma_{\text{SC}^{\text{fc}}}$	$\sigma_{\text{W}^{\text{bt}}}$	$\sigma_{\text{Cp}^{\text{bt}}}$
PLATC	1.53	59.5	2.74	1.71	0.938	3.42
MCS	1.37	66.4	2.76	1.72	0.939	3.43

pling between the enterprise and powertrain requires a large number of iterations to determine a proper fuel economy. Even thought the modification of the suspension criteria performs better for the problem, it has yet to be investigated how to apply the modified criteria to more complex hierarchies.

Table 5.5 provides the reliability analysis results compared to MCS with 20,000 samples. The relatively fewer MCS samples are used due to the expensive simulations. While constraint activities predicted by *PLATC* are accurate, MCS shows that g_1^{ent} is severely violated. The violation seems to result from inaccurate estimations in the means rather than in the standard deviations of the linking variables. Additionally, because the estimations for the linking variables between the level 2 and level 3 are relatively accurate, it can be concluded that the estimation errors are aggregated and make the estimation between the level 1 and level 2 inaccurate. Therefore, in order to improve the accuracy of the solution, more sophisticated methods, such as AMV-based methods and numerical integration methods, can be considered when the number of levels is large.

Table 5.6 provides the resulting vehicle specifications, compared with the results from [67]. The results are not directly comparable because the two vehicles are signif-

Table 5.6: Summary of results compared with the results from [67]

	This study	Results from [67]
Profit (π)	$\$6.86 \times 10^7$	N/A
Demand	6.43×10^5	N/A
Price	\$28,900	N/A
Fuel Cost Saving for the First 2 Years	\$2390	N/A
Gasoline Equivalent Fuel Economy	48.6 mpgE (SFUDS)	24.8 mpgE (UDDS)
0-60mph	8sec	20sec
Vehicle Mass	3220kg	>4270kg
Fuel Cell Max Power	113kW	$\sim$ 160kW
Battery Max Power	82.2kW	$\sim$ 50kW
Powertrain Cost	\$8,600	N/A
Fuel Cell Cost	\$8,500	N/A
Motor Cost	\$1,860	N/A
Battery Cost	\$2,050	N/A

icantly different, but a comparison is still useful because the two studies used similar underlying engineering models. The expected profit π is not significant compared to the demand. Since its approximated standard deviation at the solution is $\$3.07 \times 10^7$, there is some chance of negative profit. The low profit may result from the low fuel cost saving and hight hydrogen price. Since the hydrogen price is expected to have low volatility, the fuel cost saving would be larger and the demand and profit might be improved if a hydrogen price model for the long-run is provided.

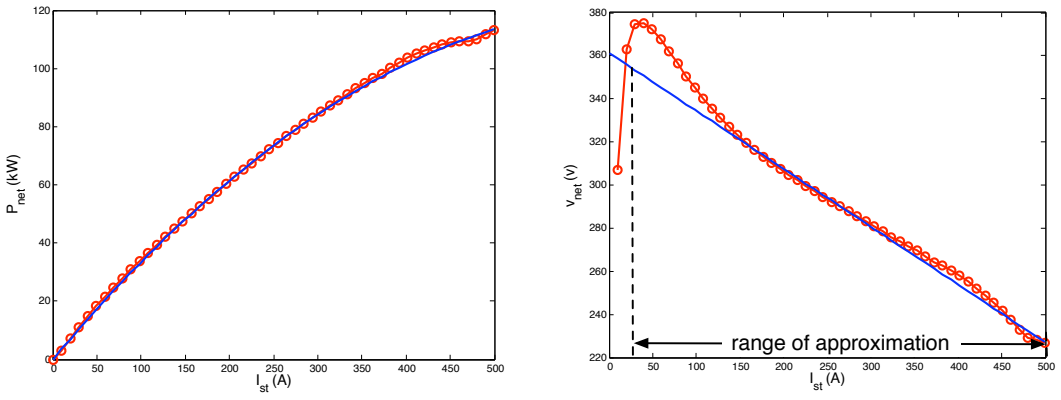

(a) Net power vs. stack current (b) Net voltage vs. stack current

Figure 5.11: Fuel cell system performance map

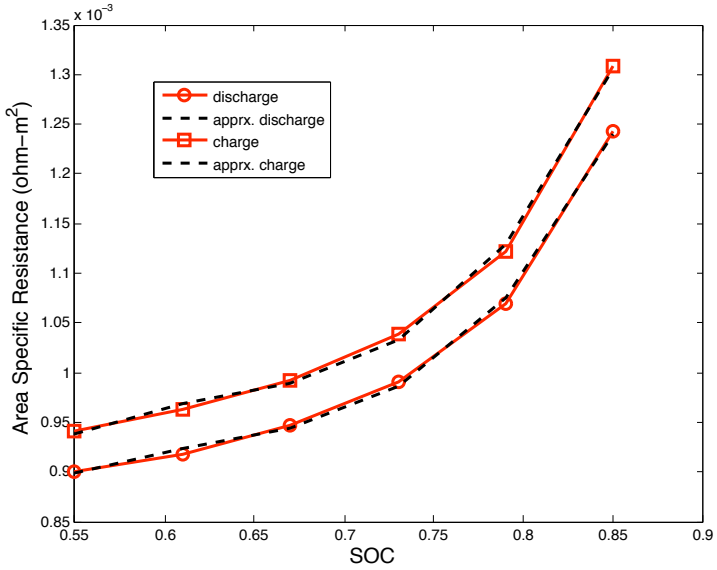

Figure 5.12: Battery resistance map

Because the vehicle in this dissertation is significantly lighter than that in [67], the difference in fuel economy and 0-60mph time is notable with the similar powertrain size. Note that the size of the fuel cell here (113kW) is comparable to that of the battery (82kW) while a considerably larger fuel cell (∼160kW) and a smaller battery (∼50kW) were obtained in [67]. The difference may result from the specific power density of the battery. Since [67] employed a NiMH battery whose specific power density ranges from 250 to 1000 W/kg, a bigger fuel cell whose specific power density is about 500 W/kg was desirable. The specific power density of Li-ion battery here, however, can be 1800W/kg or higher, which makes a bigger battery more favorable.

Figure 5.11 and 5.12 shows the performance maps of the fuel cell and the internal resistance map of the battery, respectively. Even though the approximated net voltage output from the fuel cell for 25A to 150A is not as accurate as that for the other net current, the net power approximation shows good agreement with the

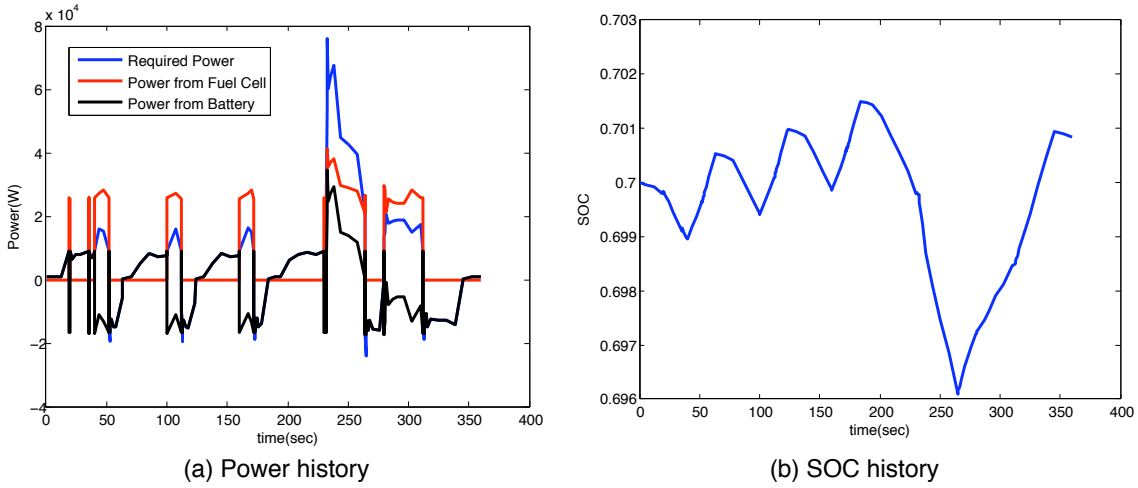

(a) Power history (b) SOC history

Figure 5.13: Simulation of a hybrid electric fuel cell vehicle

actual output because the excess in the net voltage results in below 1kW (or 5%) power loss. Because the range of discrepancy is frequently visited as shown in Figure 5.13, however, improved fuel economy could be obtained from a more accurate approximation even though the improvement would be less than 5%. Compared to the fuel cell maps, Figure 5.12 validates the agreement between the approximation and the actual performance maps for the range of approximation or operation at the solution.

Figure 5.13 (a) presents the power demand from the motor (blue), the power from the fuel cell (red) and the battery (black) during SFUDS. The power demand during the schedule is not aggressive compared to the maximum power available from the fuel cell or the battery. Moreover, Figure 5.13 (b) shows the SOC history during the cycle. As shown in both figures, ECMS splits the power demands properly so that the final SOC is maintained close to the initial SOC. As shown in both figures, ECMS splits the power demands properly so that the final SOC is maintained close to the initial SOC and satisfies the SOC constraint ($0.699 \leq \mathrm{SOC}(t_f) \leq 0.701$). Note

that the maximum deviation from the initial SOC is only 0.4%. This small deviation could results from the length of the short duty cycle and the large battery size. Since the duty cycle (SFUDS) is relatively short (< 370 seconds), the power-management strategy tends to use the fuel cell more actively.

5.4 Concluding Remarks

A comprehensive HEFCV design model was developed in this chapter, including enterprise decisions, powertrain, fuel cell and battery models. An optimization problem was formulated considering uncertainties in engineering design and marketing decisions. Especially, costumer preference and demand were assumed to be random variables because costumers behavior on HEFCV has not yet been reported. Since the linking variables between the powertrain model and its children contain performance maps, the maps were approximated in order to reduce the number of linking variables.

The problem was solved by the coordination strategies proposed in this dissertation. All proposed strategies resulted in an identical solution and the approximation of the performance maps agreed with the actual maps at the solution with less than 5% error. Since the enterprise and powertrain models are coupled more strongly than the other couplings, the suspension strategy was modified so that the targets were also compared with the responses. Even though the modified suspension strategy reduced computations significantly, more rigorous investigation is needed for the applicability of the modified suspension strategy to more complex systems. Moreover, in order to validate the accuracy and efficiency, the solution needs to be compared with results from other methods using different uncertainty propagation.

Though the proposed strategies solved the problem efficiently, the design seems less profitable because of the low fuel cost saving. Moreover, the battery cost may be considerably lower than available costs in the market. For a more comprehensive and reasonable understanding of the overall design tradeoffs, more accurate models must be provided.

CHAPTER VI

Conclusions

6.1 Dissertation Summary

The particular objective of this dissertation was to resolve computational difficulties in uncertainty propagation for MDO under uncertainty by using sequential linearization. To this end, an SLP algorithm was developed as a coordination strategy for ATC and PATC, along with convergence proofs. To illustrate the effectiveness of the proposed strategies, a number of illustrative examples were provided.

Among various uncertainty models, this dissertation focused on continuous random variables because they are most commonly used in engineering problems. In Chapter 2, several techniques to estimate propagated uncertainty were explained, including sampling techniques, local expansion methods, most probable point (MPP) methods and numerical integration methods. In terms of numerical efficiency and accuracy, MPP methods and numerical integration methods were considered more suitable for optimization than the other methods. In addition, MPP methods, such as FORM and SORM, were chosen to be applied for approximations in this dissertation. Furthermore, Chapter 2 reviewed formulation and solution approaches for design optimization and MDO under uncertainty. As the dissertation concentrated on a hierarchical decomposition strategy, the formulations of ATC and PATC and

uncertainty propagation in PATC were reviewed extensively. Previous work reviewed in Chapter 2 suggested the need for research to reduce the computational burden in estimation of propagated uncertainty for PATC.

Because sequential linearization could reduce problem complexity and be advantageous in uncertainty propagation, linearized ATC and PATC hierarchies were formulated to be used with the proposed SLP coordination strategy in Chapters 3 and 4, respectively. Unlike the other ATC formulations, the linearized ATC and PATC utilized L_∞ norms for relaxation in order to maintain linearity. Solution approaches and convergence proofs for a SLP coordination strategy for ATC and PATC were also presented. For the convergence proofs, this dissertation considered the following six formulations, illustrated in Figure 6.1: AIO, PAIO, ATC, PATC and SLP subproblems for AIO and ATC. The formulations in the upper row (PATC, ATC, SLP-ATC) are the ATC formulation of those in the lower row (PAIO, AIO, SLP-AIO) while the formulations in the second column (AIO, ATC) can be obtained by applying FORM/SORM approximation to the constraints of those in the first column (PAIO, PATC). Therefore, the solutions from AIO, ATC, PAIO and PATC

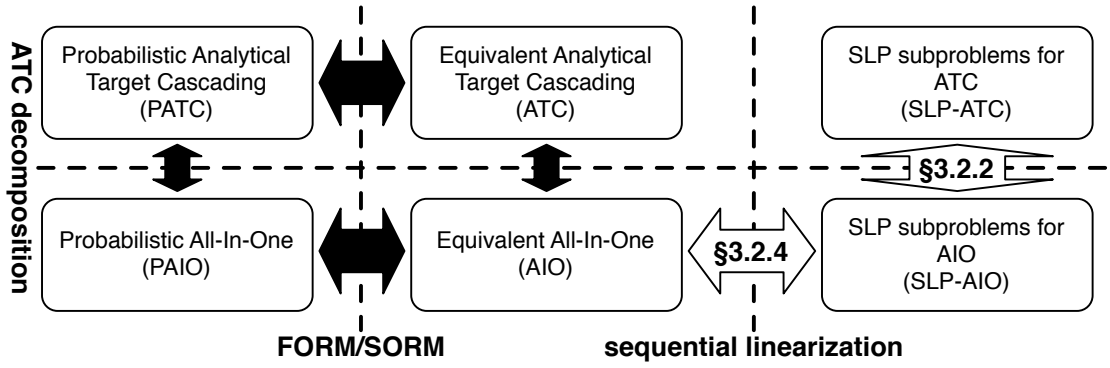

Figure 6.1: Convergence proof overview

are equivalent to each other by the ATC convergence proof [106] and optimality conditions for RBDO problems [26]. Also, SLP convergence proof was derived for the problems with only inequality constraints [57]. Thus, in order to complete the convergence proof of the proposed coordination strategy, Section 3.2.2 showed that the convergence proof of ATC still holds for linearized ATC with the L_∞ norms based on HOC strategy. Moreover, since decomposition introduces equality constraints for system consistency, the previous SLP convergence proof was extended for problems with inequality and equality constraints based on the Mangasarian-Fromowitz constraint qualication in Section 3.2.4.

In order to further reduce the computational cost, a suspension strategy was applied by suspending coordination between weakly coupled elements. The effectiveness of the proposed strategies was demonstrated in several illustrative examples. Reduction in computations by the suspension strategy was varied when using varying parameters for suspension criteria and coupling strengths between elements. However, the suspension strategy may invalidate algorithmic convergence, so it might be used with caution until this convergence behavior is investigated more thoroughly.

A comprehensive design model for a Hybrid Electric Fuel Cell Vehicle (HEFCV) that took into account uncertainties in both engineering design and marketing decisions was developed in Chapter 5. The design problem, including enterprise, powertrain, fuel cell and battery models, was solved by the proposed strategies. Since linking variables between powertrain and fuel cell/battery contained performance maps, the maps were approximated by linear or quadratic functions and the coefficients of the approximated functions were used as linking variables to represent the maps. Additionally, because the coupling between enterprise and powertrain models

was stronger than the others, the suspension strategy was modified so that the step sizes of both targets and responses could be compared in the suspension criteria. Even though the solutions from the proposed strategies agreed to each other, the accuracy and computational efficiency of the proposed strategies has yet to be proven fully through comparison with results from other methods.

6.2 Contributions

The main contributions of this dissertation are summarized as follows:

- Development of an SLP algorithm to coordinate ATC and PATC problem by applying L_∞ norms for relaxation.
- Convergence proofs of the proposed coordination strategies for the use of L_∞ norms and the inclusion of equality constraints.
- Application of a suspension strategy and development of suspension criteria for the SLP coordination strategy for ATC and PATC.
- Demonstration of the proposed strategies to a comprehensive design model for HEFCV taking into account uncertainties in both engineering design and marketing decisions.

6.3 Future Work

The following research issues require future investigation:

- **Extension of the proposed strategies to other MDO formulations under uncertainty.** The SLP coordination and suspension strategies can be applied to other decomposition methods, such as collaborative optimization

and BLISS under uncertainty. Since many design problems can be decomposed by aspects not objects, this would expand the range of the applications of the proposed strategies.

- **Improved suspension strategy.** The suspension strategy requires iterations between suspension and validation. Also, reduction in computation by the strategy is considerably sensitive to problem formulations and suspension parameters that require several tunings. Therefore, improved suspension criteria based on coupling strength may reduce computations more effectively. Additionally, promising results achieved by including the step sizes of targets shown in Chapter 5 warrant further investigation of the modified suspension strategy.

- **Usage of other uncertainty propagation methods for LP approximation.** Because the local expansion methods were used for the mean and variance estimation of coupling variables, the estimations were inaccurate if response functions were highly nonlinear functions, and this resulted in inaccurate solutions, especially for the HEFCV design problem. Therefore, using more accurate methods for highly nonlinear functions judiciously could improve the accuracy and efficiency of the proposed coordination strategies.

- **System consistency with random linking variables.** The equivalence of random variables in this dissertation was determined by the equality in mean and variance, which resulted in inaccuracy of solutions. A more appropriate approximation of random variables could provide more accurate solutions with little increase in computational cost.

BIBLIOGRAPHY

BIBLIOGRAPHY

[1] *PNGV Battery Test Manual Revision 3, DOE/ID-10597*, Feburary 2001.

[2] Ethan C. Abeles. Analysis of light-duty vehicle price trends in the U.S. Technical Report UCD-ITS-RR-04-15, Institute of Transportation Studies, University of California, Davis, 2004.

[3] Ron Adner and Daniel Levinthal. Demand heterogeneity and technology evolution: Implications for product and process innovation. *Management Science*, 47(5):611–628, 2001.

[4] Harish Agarwal, John E. Renaud, Evan L. Preston, and Dhanesh Padmanabhan. Uncertainty quantification using evidence theory in multidisciplinary design optimization. *Reliability Engineering & System Safety*, 85(1-3):281–294, 2004.

[5] Natalia M. Alexandrov and Robert Michael Lewis. Analytical and computational aspects of collaborative optimization for multidisciplinary design. *AIAA Journal*, 40(2):301 – 309, 2002.

[6] James Allison. *Optimal Partitioning and Coordination Decisions in Decomposition-based Design Optimization*. PhD thesis, University of Michigan, 2007.

[7] J.T. Allison, M. Kokkolaras, Marc Zawislak, and P.Y. Papalambros. On the use of analytical target cascading and collaborative optimization for complex system design. In *Proceedings of the 6th World Congress on Structural and Multidisciplinary Optimization*, Rio de Janeiro, Brazil, May 30 - June 3 2005.

[8] Sulaiman F. Alyaqout, Panos Y. Papalambros, and A. Galip Ulsoy. Quantification and use of system coupling in decomposed design optimization problems. *ASME Computers and Information in Engineering Division*, 10:95 – 103, 2005.

[9] J.C. Amphlett, R.M. Baumert, R.F. Mann, B.A. Peppley, and P.R. Roberge. Performance modeling of the ballard mark IV solid polymer electrolyte fuel cell. *Journal of Electrochemical Society*, 142(1):1–8, 1995.

[10] J.C. Amphlett, R.F. Mann, B.A. Peppley, P.R. Roberge, and A. Rodrigues. Model predicting transient responses of proton exchange membrane fuel cells. *Journal of Power Sources*, 61:183–188, 1996.

[11] R.J. Balling and J. Sobieszczanski-Sobieski. Optimization of coupled systems: A critical overview of approaches. *AIAA Journal*, 34(1):6 – 17, 1996.

[12] J. Baschuk and X. Li. Modelling of polymer electrolyte membrane fuel cells with variable degrees of water flooding. *Journal of Power Sources*, 86:181–196, 2000.

[13] Stephen M. Batill, John E. Renaud, and Xiaoyu Gu. Modeling and simulation uncertainty in multidisciplinary design optimization. In *8th AIAA/USAF/NASA/ISSMO Symposium on Multidisciplinary Analysis and Optimization*, number AIAA-2000-4803, Long Beach, CA, Sept. 6-8 2000.

[14] A. D. Belegundu and S. H. Zhang. Robustness of design through minimum sensitivity. *Journal of Mechanical Design*, 2(114):213–217, 1992.

[15] Y. Ben-Haim and I. Elishakoff. *Convex Models of Uncertainty in Applied Mechanics*. Elsevier, Amsterdam, 1990.

[16] P. Berg, K. Promislow, J. Pierre, and J. Stumper. Water management in PEM fuel cells. *Journal of Electrochemical Society*, 151(3):A341–A353, 2004.

[17] D. Bernardi and M. Verbrugge. Mathematical model of a gas diffusion electrode bonded to a polymer electrolyte. *AIChE Journal*, 37(8):1151–1163, 1991.

[18] Dimitri P. Bertsekas. *Nonlinear programming*. Athena Scientific, 2nd edition, 1999.

[19] Alan P. Bowling, John E. Renaud, Jeremy T. Newkirk, Neal M. Patel, and Harish Agarwal. Reliability-based design optimization of robotic system dynamic performance. *Journal of Mechanical Design*, 129(4):449–454, 2007.

[20] R. Braun, I. Kroo, and A. Moore. Use of the collaborative optimization architecture for launch vehicle design, 1996.

[21] Karl Breitung. Asymptotic approximations for multinormal integrals. *Journal of Engineering Mechanics*, 110(3):357 – 366, 1984.

[22] Karl Breitung. Asymptotic approximations for probability integrals. *Probabilistic Engineering Mechanics*, 4(4):187 – 190, 1989.

[23] H. Bussel, F. Koene, and R. Mallant. Dynamic model of solid polymer fuel cell water management. *Journal of Power Sources*, 71:218–222, 1998.

[24] Eric Carlson, Peter Kopf, Jayanti Sinha, Suresh Sriramulu, and Yong Yang. PEM fuel cell cost status - 2005. *Fuel Cell Seminar*, November 14-18, 2005.

[25] Enrique Castillo, Miguel A. Losada, Roberto Minguez, Carmen Castillo, and Asuncion Baquerizo. Optimal engineering design method that combines safety factors and failure probabilities: Application to rubble-mound breakwaters. *Journal of Waterway, Port, Coastal and Ocean Engineering*, 130(2):77 – 88, 2004.

[26] K.-Y. Chan. *Monotonicity, Activity and Sequential Linearizations in Probabilistic Design Optimization*. PhD thesis, University of Michigan, Ann Arbor, Michigan, USA., 2006.

[27] Kuei-Yuan Chan, Steven Skerlos, and Panos Y. Papalambros. Monotonicity and active set strategies in probabilistic design optimization. *Journal of Mechanical Design*, 128(4):893–900, 2006.

[28] Kuei-Yuan Chan, Steven J. Skerlos, and Panos Papalambros. An adaptive sequential linear programming algorithm for optimal design problems with probabilistic constraints. *Journal of Mechanical Design*, 129(2):140–149, 2007.

[29] Shih-Pin Chen. Robust design with dynamic characteristics using stochastic sequential quadratic programming. *Engineering Optimization*, 35(1):79 – 89, 2003.

[30] Wei Chen and Kemper Lewis. Robust design approach for achieving flexibility in multidisciplinary design. *AIAA Journal*, 37(8):982 – 989, 1999.

[31] Xiaoguang Chen, Timothy K. Hasselman, and Douglas J. Neill. Reliability based structural design optimization for practical applications. *Collection of Technical Papers - AIAA/ASME/ASCE/AHS/ASC Structures, Structural Dynamics & Materials Conference*, 4:2724 – 2732, 1997.

[32] K. Choi and B. Youn. On probabilistic approaches for reliability-based design optimization (RBDO). In *9th AIAA/ISSMO Symposium on Multidisciplinary Analysis and Optimization*, number AIAA-2002-5472, Atlanta, Georgia, Sep. 4-6 2002.

[33] Kyung K. Choi, Yoojeong Noh, and Liu Du. Reliability based design optimization with correlated input variables using copulas. In *ASME Internaltional Design Engineering Technical Conference & Computers and Information in Engineering Conference*, number DETC2007-35104, Las Vegas, NV, United States, Sep. 4-7 2007.

[34] Kyung K. Choi, Byeng D. Youn, and Jun Tang. Structural durability design optimization and its reliability assessment. *Proceedings of the ASME Design Engineering Technical Conference*, 2 A:73 – 83, 2003.

[35] Adam B. Cooper, Panayotis Georgiopoulos, Harrison M. Kim, and Panos Y. Papalambros. Analytical target setting: An enterprise context in optimal product design. *Journal of Mechanical Design*, 128(1):4–13, 2006.

[36] C.A. Cornell. Bounds on reliability of structural systems. *American Society of Civil Engineers Proceedings, Journal of the Structural Division*, 93(ST1):171 – 200, 1967.

[37] Evin J. Cramer, Jr. J. E. Dennis, Paul D. Frank, Robert Michael Lewis, and Gregory R. Shubin. Problem formulation for multidisciplinary optimization. *SIAM Journal on Optimization*, 4(4):754–776, 1994.

[38] J. Cunningham, M. Hoffman, R. Moore, and D. Friedman. Requirements for a flexible and realistic air supply model for incorporation into a fuel cell vehicle (FCV) system simulation. *Future Transportation Technology Conference and Exposition*, Costa Mesa, California, August 17-19 1999.

[39] Indraneel Das. Robustness optimization for constrained nonlinear programming problems. *Engineering Optimization*, 32(5):585 – 618, 2000.

[40] D.P. Davies and P.L. Adcock. Lightweight, high power density fuel cell stack. *ETSU F02/00216/REP DTI/Pub URN 02/643*, 2002.

[41] Ove Ditlevsen. Generalized second moment reliability index. *Journal of Structural Mechanics*, 7(4):435 – 451, 1979.

[42] U.M. Diwekar and J.R. Kalagnanam. Robust design using an efficient sampling technique. *Comput. Chem. Eng. (UK)*, 20:389 – 94, 1996.

[43] Urmila M. Diwekar and Jayant R. Kalagnanam. Efficient sampling technique for optimization under uncertainty. *AIChE Journal*, 43(2):440 – 447, 1997.

[44] DOE. Energy prices. http://www.eia.doe.gov/price.html, october, 2007.

[45] DOE and DOT. Hydrogen posture plan hydrogen posture plan: An integrated research, development and demonstration plan. Technical report, United States Department of Energy and United States Department of Transportation, 2006.

[46] Joseph L. Doob. The development of rigor in mathematical probability (1900-1950). *The American Mathematical Monthly*, 103(7):586–595, aug 1996.

[47] Marc Doyle, Thomas F. Fuller, and John Newman. Modeling of galvanostatic charge and discharge of the lithium/polymer/insertion cell. *Journal of The Electrochemical Society*, 140(6):1526–1533, 1993.

[48] Xiaoping Du and Wei Chen. Methodology for managing the effect of uncertainty in simulation-based design. *AIAA Journal*, 38(8):1471 – 1478, 2000.

[49] Xiaoping Du and Wei Chen. Efficient uncertainty analysis methods for multidisciplinary robust design. *AIAA Journal*, 40(3):545 – 552, 2002.

[50] Xiaoping Du and Wei Chen. Sequential optimization and reliability assessment method for efficient probabilistic design. *Journal of Mechanical Design*, 126(2):225–233, 2004.

[51] Xiaoping Du and Wei Chen. Collaborative reliability analysis under the framework of multidisciplinary systems design. *Optimization and Engineering*, 6(1):63 – 84, 2005.

[52] G. Emch and A. Parkinson. Robust optimal design for worst-case tolerances. *Journal of Mechanical Design, Transactions of the ASME*, 116(4):1019 – 1025, 1994.

[53] K. English, C.L. Bloebaum, and E. Miller. Development of multiple cycle coupling suspension in the optimization of complex systems. *Structural and Multidisciplinary Optimization*, 22(4):268 – 283, 2001.

[54] EPA. Nonconformance penalties for 2004 highway heavy duty diesel engines. Final Technical Support Document EPA420-R-02-021, United States Environmental Protection Agency, 2002.

[55] Bernd Fiessler, Hans-Joachim Neumann, and Rudiger Rackwitz. Quadratic limit states in structural reliability. *Journal of the Engineering Mechanics Division*, 105(4):661 – 676, 1979.

[56] Z. Filipi, L. Louca, B. Daran, C.C. Lin, U. Yildir, B.Wu, M. Kokkolaras, D. Assanis, H. Peng, P. Papalambros, and J. Stein. Combined optimization of design and power management of the hydraulic hybrid propulsion system for the 6x6 medium truck. *International Journal of Heavy Vehicle Systems*, 11(3-4):371–401, 2004.

[57] R. Fletcher, S. Leyer, and P.L. Toint. On the global convergence of an SLP–filter algorithm. *Numerical Analysis Report NA/183, University of Dundee, UK*, 98(13):1–11, 1998.

[58] R. Fletcher, S. Leyffer, and Ph. L. Toint. A brief history of filter methods. Technical Report ANL/MCS-P1372-0906, Argonne National Laboratory, Mathematics and Computer Science Division, September 2006.

[59] Roger Fletcher and Sven Leyffer. Nonlinear programming without a penalty function. *Mathematical Programming*, V91(2):239–269, 2002.

[60] Roger Fletcher, Sven Leyffer, and Philippe L. Toint. On the global convergence of a filter–SQP algorithm. *SIAM Journal on Optimization*, 13(1):44–59, 2002.

[61] Thomas F. Fuller, Marc Doyle, and John Newman. Simulation and optimization of the dual lithium ion insertion cell. *Journal of The Electrochemical Society*, 141(1):1–10, 1994.

[62] M. Grujicic, K.M. Chittajallu, and J.T. Pukrushpan. Control of the transient behaviour of polymer electrolyte membrane fuel cell systems. *Proceedings of the Institution of Mechanical Engineers, Part D: Journal of Automobile Engineering*, 218(11):1239 – 1250, 2004.

[63] X. Gu, J.E. Renaud, S.M. Batill, R.M. Brach, and A.S. Budhiraja. Worst case propagated uncertainty of multidisciplinary systems in robust design optimization. *Structural and Multidisciplinary Optimization*, 20(3):190 – 213, 2000.

[64] Yann Guezennec, Ta-Young Choi, Gino Paganelli, and Giorgio Rizzoni. Supervisory control of fuel cell vehicles and its link to overall system efficiency and low-level control requirements. *Proceedings of the American Control Conference*, 3:2055 – 2061, 2003.

[65] L. Guzzella. Control oriented modelling of fuel-cell based vehicles. *Presentation in NSF Workshop on the Integration of Modeling and Control for Automotive systems*, 1999.

[66] A. Haldar and S. Mahadevan. *Probability, Reliability and Statistical Methods in Engineering Design*. John Wiley & Sons Inc., New York, NY, USA, 2000.

[67] Jeongwoo Han, Michael Kokkolaras, and Panos Papalambros. Optimal design of hybrid fuel cell vehicles. In *the 4th International Conference on Fuel Cell Science, Engineering and Technology*, number FUELCELL2006-97161. ASME, 2006.

[68] Alf Harbitz. Efficient sampling method for probability of failure calculation. *Structural Safety*, 3(2):109 – 115, 1986.

[69] F.E. Haskin, B.D. Staple, and C. Ding. Efficient uncertainty analyses using fast probability integration. *Nucl. Eng. Des. (Netherlands)*, 166(2):225 – 48, 1996.

[70] Abraham M. Hasofer and N. C. Lind. Exact and invariant second-moment code format. *Journal of the Engineering Mechanics Division-ASCE*, 100(NEM1):111–121, 1974.

[71] Glenn Hess. Push on hill for fuel independence, December 5, 2005.

[72] Willi Hock and K. Schittkowski. *Test Examples for Nonlinear Programming Codes*. Springer-Verlag New York, Inc., Secaucus, NJ, USA, 1981.

[73] M. Hohenbichler and R. Rackwitz. First-order concepts in system reliability. *Structural Safety*, 1(3):177–188, 1983.

[74] Monu Kalsi, Kurt Hacker, and Kemper Lewis. A comprehensive robust design approach for decision trade-offs in complex systems design. *Journal of Mechanical Design*, 123(1):1–10, 2001.

[75] Ashish Karamchandani and C. Allin Cornell. Adaptive hybrid conditional expectation approaches for reliability estimation. *Structural Safety*, 11(1):59 – 74, 1991.

[76] Nachiket T. Kasarekar and Kenneth W. English. Development of a hybrid MDF/IDF multidisciplinary optimization solution method with coupling suspension. *Collection of Technical Papers - 10th AIAA/ISSMO Multidisciplinary Analysis and Optimization Conference*, 3:1865 – 1874, 2004.

[77] Harrison M. Kim, Wei Chen, and Margaret M. Wiecek. Lagrangian coordination for enhancing the convergence of analytical target cascading. *AIAA Journal*, 44(10):2197 – 2207, 2006.

[78] Harrison M. Kim, Deepak K.D. Kumar, Wei Chen, and Panos Y. Papalambros. Target exploration for disconnected feasible regions in enterprise-driven multilevel product design. *AIAA Journal*, 44(1):67–77, 2006.

[79] Hyung Min Kim, Michael Kokkolaras, Loucas S. Louca, George J. Delagrammatikas, Nestor F. Michelena, Zoran S. Filipi, Panos Y. Papalambros, Jeffrey L. Stein, and Dennis N. Assanis. Target cascading in vehicle redesign: A class VI truck study. *International Journal of Vehicle Design*, 29(3):199 – 225, 2002.

[80] Hyung Min Kim, N.F. Michelena, P.Y. Papalambros, and Tao Jiang. Target cascading in optimal system design. *Trans. ASME, J. Mech. Des. (USA)*, 125(3):474 – 80, Sept. 2003.

[81] Hyung Min Kim, D. Geoff Rideout, Panos Y. Papalambros, and Jeffrey L. Stein. Analytical target cascading in automotive vehicle design. *Journal of Mechanical Design*, 125(3):481–489, 2003.

[82] S.K. Kim and S.H. Choi. Development of fuel cell hybrid vehicle by using ultracapacitors as a secondary power source. *2005 SAE World Congress*, (2005-01-0015), Detroit, Michigan, April 11-14 2005.

[83] M. Kokkolaras, R. Fellini, H.M. Kim, N.F. Michelena, and P.Y. Papalambros. Extension of the target cascading formulation to the design of product families. *Structural and Multidisciplinary Optimization*, 24(4):293 – 301, 2002.

[84] Michael Kokkolaras, Zissimos P. Mourelatos, and Panos Y. Papalambros. Design optimization of hierarchically decomposed multilevel systems under uncertainty. *Journal of Mechanical Design, Transactions of the ASME*, 128(2):503 – 508, 2006.

[85] Ilan Kroo. Multidisciplinary optimization applications in preliminary design - status and directions. In *AIAA/ASME/ASCE/AHS/ASC Structures, Structural Dynamics, and Materials Conference and Exhibit, 38th, and AIAA/ASME/AHS Adaptive Structures Forum, Kissimmee, FL, Apr. 7-10*, number AIAA-1997-1408, 1997.

[86] Ilan Kroo, Steve Altus, Robert Braun, Peter Gage, and Ian Sobieski. Multidisciplinary optimization methods for aircraft preliminary design. *AIAA/USAF/NASA/ISSMO Symposium on Multidisciplinary Analysis and Optimization*, (AIAA 94-4325):697–707, 1994.

[87] J. Larminie and A. Dicks. *Fuel Cell System Explained*. John Wiley & Sons Ltd., New York, 2nd edition, 2002.

[88] Julie B. Lassiter, Margaret M. Wiecek, and Kara R. Andrighetti. Lagrangian coordination and analytical target cascading: Solving ATC-decomposed problems with lagrangian duality. *Optimization and Engineering*, 6(3):361–381, 2005.

[89] Ikjin Lee, Kyung K. Choi, Liu Du, and David Gorsich. A new inverse reliability analysis method using MPP-based dimension reduction method (DRM). In *ASME Internaltional Design Engineering Technical Conference & Computers and Information in Engineering Conference*, number DETC2007-35098, Las Vegas, NV, United States, Sep. 4-7 2007.

[90] Jinkoo Lee, D.J. Li, Xiaoping Liu, Nathan Soderborg, Agus Sudjianto, Mahesh Vora, and Steve C. Wang. An approach to robust design employing computer experiments. *Proceedings of the ASME Design Engineering Technical Conference*, 2:793 – 799, 2001.

[91] Sang Hoon Lee and Wei Chen. A comparative study of uncertainty propagation methods for black-box type functions. In *ASME Internaltional Design Engineering Technical Conference & Computers and Information in Engineering Conference*, number DETC2007-35533, Las Vegas, NV, United States, Sep. 4-7 2007.

[92] Sang Hoon Lee and Byung Man Kwak. Response surface augmented moment method for efficient reliability analysis. *Structural Safety*, 28(3):261–272, 2006.

[93] Tae Won Lee and Byung Man Kwak. A reliability-based optimal design using advanced first order second moment method. *Mechanics Based Design of Structures and Machines*, 15(4):523 – 542, 1987.

[94] Yanjing Li, Zhaosong Lu, and Jeremy J. Michalek. Diagonal quadratic approximation for parallelization of analytical target cascading. In *ASME Internaltional Design Engineering Technical Conference & Computers and Information in Engineering Conference*, number DETC2007-35566, Las Vegas, NV, United States, Sep. 4-7 2007.

[95] Jinghong Liang, Zissimos P. Mourelatos, and Jian Tu. A single-loop method for reliability-based design optimization. *Proceedings of the ASME Design Engineering Technical Conference*, 1:419 – 430, 2004.

[96] C.C. Lin, Z. Filipi, L. Louca, H H. Peng, D. Assanis, and J. Stein. Modelling and control of a medium-duty hybrid electric truck. *International Journal of Heavy Vehicle Systems*, 11(3-4):349–371, 2004.

[97] Chan-Chiao Lin, Huei Peng, and J. W. Grizzle. A stochastic control strategy for hybrid electric vehicles. *American Control Conference, 2004. Proceedings of the 2004*, 5:4710–4715 vol.5, 2004.

[98] Chan-Chiao Lin, Huei Peng, Jessy W. Grizzle, and Jun-Mo Kang. Power management strategy for a parallel hybrid electric truck. *IEEE Transactions on Control Systems Technology*, 11(6):839 – 849, 2003.

[99] Timothy E. Lipman and Mark A. Delucchi. Hybrid electric vehicle design: Retail and lifecycle cost analysis. Technical Report UCD-ITS-RR-03-01, Institute of Transportation Studies, University of California, Davis, 2003.

[100] Huibin Liu, Wei Chen, M. Kokkolaras, P.Y. Papalambros, and H.M. Kim. Probabilistic analytical target cascading: a moment matching formulation for multilevel optimization under uncertainty. *Trans. ASME, J. Mech. Des. (USA)*, 128(4):991 – 1000, 2006.

[101] L. S. Louca, M. Kokkolaras, G. J. Delagrammatikas, N. F. Michelena, Z. S. Filipi, P. Y. Papalambros, , and D. N. Assanis. Analytical target cascading for the design of an advanced technology heavy truck. In Y. Bayazitoglu, editor, *ASME International Mechanical Engineering Congress and Exposition*, volume 115, New Orleans, LA, November 17-22 2002.

[102] Olvi L. Mangasarian. *Nonlinear Programming*. McGraw-Hill, New York, 1969.

[103] A. Mawardi, F. Yang, and R. Pitchumani. Optimization of the operating parameters of a proton exchange membrane fuel cell for maximum power density. *Journal of Fuel Cell Science and Technology*, 2(2):121–135, 2005.

[104] Jeremy J. Michalek, Fred M. Feinberg, and Panos Y. Papalambros. Linking marketing and engineering product design decisions via analytical target cascading. *Journal of Product Innovation Management*, 22(1):42–62, 2005.

[105] J.J. Michalek and P.Y. Papalambros. An efficient weighting update method to achieve acceptable consistency deviation in analytical target cascading. *Trans. ASME, J. Mech. Des. (USA)*, 127(2):206 – 14, 2005.

[106] Nestor Michelena, Hyungju Park, and Panos Y. Papalambros. Convergence properties of analytical target cascading. *AIAA Journal*, 41(5):897 – 905, 2003.

[107] R.E. Moore. *Interval Analysis*. Prentice-Hall, Englewood Cliffs, NJ, 1996.

[108] C. Musardo, G. Rizzoni, and B. Staccia. A-ECMS: An adaptive algorithm for hybrid electric vehicle energy management. *Decision and Control, 2005 and 2005 European Control Conference. CDC-ECC '05. 44th IEEE Conference on*, pages 1816–1823, 2005.

[109] P. Nelson, I. Bloom, K. Amine, and G. Henriksen. Design modeling of lithium-ion battery performance. *Journal of Power Sources*, 110:437–444(8), 2002.

[110] Joan M. Ogden, Robert H. Williams, and Eric D. Larson. Societal lifecycle costs of cars with alternative fuels/engines. *Energy Policy*, 32(1):7–27, 2004.

[111] G. Paganelli, M. Tateno, A. Brahma, G. Rizzoni, and Y. Guezennec. Control development for a hybrid-electric sport-utility vehicle: strategy, implementation and field test results. volume 6, pages 5064–5069 vol.6, 2001.

[112] P.Y. Papalambros and D.J. Wilde. *Principles of Optimal Design: Modeling and Computation*. Cambridge University Press, Cambridge, 2nd edition, 2000.

[113] Athanasios Papoulis and S. Unnikrishna Pillai. *Probability, Random Variables, and Stochastic Processes*. McGraw-Hill, 4th edition, 2002.

[114] K. Pearson. *Tables for Statisticians and Biometricians*, volume 1. Cambridge University Press, Cambridge, 1914.

[115] P. Pisu and G. Rizzoni. A comparative study of supervisory control strategies for hybrid electric vehicles. *Control Systems Technology, IEEE Transactions on*, 15(3):506–518, 2007.

[116] Jay T. Pukrushpan, Anna G. Stefanopoulou, and Huei Peng. *Control of Fuel Cell Power Systems: Principles, Modeling, Analysis and Feedback Design*. Springer, 2004.

[117] S. Rahman and H. Xu. A univariate dimension-reduction method for multi-dimensional integration in stochastic mechanics. *Probabilistic Engineering Mechanics*, 19(4):393–408, 2004.

[118] Murray Rosenblatt. Remarks on a multivariate transformation. *The Annals of Mathematical Statistics*, 23(3):470–472, 1952.

[119] A. Rowe and X. Li. Mathematical modeling of proton exchange membrane fuel cells. *Journal of Power Sources*, 102(1-2):82–96, 2001.

[120] Bruno Scrosati. Lithium rocking chair batteries: An old concept? *Journal of The Electrochemical Society*, 139(10):2776–2781, 1992.

[121] M.L. Shooman. *Probabilistic Reliability : An Engineering Approach*. McGraw-Hill, New York, NY, USA, 1968.

[122] D. Simbeck and E. Chang. Hydrogen supply: Cost estimate for hydrogen pathways - scoping analysis. Technical Report NREL/SR-540-32525, National Renewable Energy Laboratory, 2002.

[123] T.E. Springer, M.S. Wilson, and S. Gottesfeld. Modeling and experimental diagnostics in polymer electrolyte fuel cells. *Journal of Electrochemical Society*, 140(12):3513–3526, 1993.

[124] Robert H. Sues, David R. Oakley, and Graham S. Rhodes. Multidisciplinary stochastic optimization. *Proceedings of Engineering Mechanics*, 2:934 – 937, 1995.

[125] R.V. Tappeta and J.E. Renaud. Multiobjective collaborative optimization. *Journal of Mechanical Design, Transactions of the ASME*, 119(3):403 – 411, 1997.

[126] S. Tosserams, L.F.P. Etman, P.T. Papalambros, and J.E. Rooda. An augmented lagrangian relaxation for analytical target cascading using the alternating direction method of multipliers. *Struct. Multidiscip. Optim. (Germany)*, 31(3):176 – 89, 2006.

[127] J. Tu, K.K. Choi, and Y.H. Park. Design potential method for robust system parameter design. *AIAA Journal*, 39(4):667 – 677, 2001.

[128] U.S. Department of Transportation, NHTSA. Summary of fuel economy performance, March 2004.

[129] Daniele Veneziano. New index of reliability. 105(2):277 – 296, 1979.

[130] Xiaoqun Wang. Quasi-monte carlo integration of characteristic functions and the rejection sampling method. *Computer Physics Communications*, 123(1-3):16 – 26, 1999.

[131] Z.H. Wang, C.Y. Wang, and K.S. Chen. Two-phase flow and transport in the air cathode of proton exchange membrane fuel cells. *Journal of Power Sources*, 94:40–50, 2001.

[132] M. Wohr, K. Bolwin, W. Schnurnberger, M. Fischer, W. Neubrand, and G. Eigenberger. Dynamic modelling and simulation of a polymer membrane fuel cell including mass traksport limitation. *International Journal of Hydroyen Energy*, 23(3):213–218, 1998.

[133] Y.-T. Wu. Adaptive importance sampling method for structural system reliability analysis. *American Society of Mechanical Engineers, Aerospace Division (Publication) AD*, 28:217 – 231, 1992.

[134] Y.-T. Wu. Computational methods for efficient structural reliability and reliability sensitivity analysis. *AIAA Journal*, 32(8):1717 – 1723, 1994.

[135] Y.T. Wu and O. H. Burnside. Efficient probabilistic structural analysis using an advanced mean value method. In *Probabilistic Methods in Civil Engineering*, pages 492–495, 1988.

[136] Y.T. Wu, H.R. Millwater, and T.A. Cruse. Advanced probabilistic structural analysis method for implicit performance functions. *AIAA Journal*, 28(9):1663 – 1669, 1990.

[137] Y.T. Wu and W. Wang. Efficient probabilistic design by converting reliability constraints to approximately equivalent deterministic constraints. *Journal of Integrated Design and Process Sciences*, 2(4):13–21, 1998.

[138] H. Xu and S. Rahman. A generalized dimension-reduction method for multidimensional integration in stochastic mechanics. *International Journal for Numerical Methods in Engineering*, 61(12):1992–2019, 2004.

[139] D. Xue and Z. Dong. Optimal fuel cell system design considering functional performance and production costs. *Journal of Power Sources*, 76(1):69–80, 1998.

[140] Byeng D. Youn and Kyung K. Choi. A new response surface methodology for reliability-based design optimization. *Computers and Structures*, 82(2-3):241 – 256, 2004.

[141] Byeng D. Youn, Kyung K. Choi, and Liu Du. Enriched performance measure approach for reliability-based design optimization. *AIAA Journal*, 43(4):874 – 884, 2005.

[142] Byeng D. Youn, Kyung K. Choi, and Young H. Park. Hybrid analysis method for reliability-based design optimization. *Journal of Mechanical Design*, 125(2):221–232, 2003.

[143] Byeng D. Youn, Zhimin Xi, Lee J. Wells, and Pingfeng Wang. Enhanced dimension-reduction (eDR) method for sensitivity-free uncertainty quantification. In *11th AIAA/ISSMO Multidisciplinary Analysis and Optimization Conference*, number AIAA 2006-6977, Portsmouth, Virginia, September 6-8 2006.

[144] L. A. Zadeh. Fuzzy sets. *Information and Control*, 8(3):338–353, 1965.

[145] Jinhuan Zhang, Margaret M. Wiecek, and Wei Chen. Local approximation of the efficient frontier in robust design. *Journal of Mechanical Design, Transactions of the ASME*, 122(2):232 – 236, 2000.

[146] Yan-Gang Zhao and Tetsuro Ono. General procedure for first/second-order reliability method (FORM/SORM). *Structural Safety*, 21(2):95 – 112, 1999.

[147] Yan-Gang Zhao and Tetsuro Ono. New approximations for SORM: Part 1. *Journal of Engineering Mechanics*, 125(1):79 – 85, 1999.

[148] Yan-Gang Zhao and Tetsuro Ono. New approximations for SORM: Part 2. *Journal of Engineering Mechanics*, 125(1):86 – 93, 1999.